

Development of a High-Bandwidth Current Sensor for High-Frequency Power Applications

Master's Thesis of

Sven Hauer

at the Department of Electrical Engineering and Information Technology
Institute for Data Processing and Electronics (IPE)
KIT ASIC and Detector Laboratory (KIT-ADL)

Supervisor: Prof. Dr. Ivan Perić
Advisor: M.Sc. Roberto Blanco

09. April 2018 – 27. September 2018

I declare that I have developed and written the enclosed thesis completely by myself, and have not used sources or means without declaration in the text.

Karlsruhe, 27. September 2018

.....
(Sven Hauer)

© 2018 Sven Hauer



This work and all its parts is published under the terms of the Creative Commons Attribution 4.0 International License. To view a copy of this license, visit <http://creativecommons.org/licenses/by/4.0/>.

The software used to accomplish the thesis can be shared upon request.
If you reuse any part of this work, I'm happy to hear about it. Email me at thesis@uniku.de.

DOI: 10.5445/IR/1000090453

Abstract

The aim of this master thesis is to develop a high-bandwidth current sensor for a nominal design current of 100 A and a nominal design bandwidth of 100 MHz.

After an analysis which properties are important to develop a current sensor, a requirement list was stated. Several current sensing methods were described and their qualification for the stated requirements were evaluated. With the resulting sensing concept, consisting out of Rogowski coils and magneto resistors, a system design was elaborated. One requirement was to develop a current sensor which needs less effort in series production than a regular Rogowski coil. Therefore, a planar Rogowski coil was proposed for this sensor development. Furthermore, a magnetic field simulation was designed. Based on the results, a optimal placement simulation for both sensors was carried out. In the final design phase, the galvanic insulation requirements of 4.8 kV based on the corresponding standards were investigated and implemented. The test equipment used in this thesis was designed and build in-house at IPE (KIT-ADL). Commercial solutions did not offer the suggested requirements for generating a double pulse with the necessary rise time to characterize the current sensor's bandwidth. The test equipment was able to apply pulses with a maximum current of 200 A and a rise time of 1 ns to the device under test. The prototype is able to sense a current up to ± 100 A with a bandwidth of 20 MHz.

Acknowledgement

I would like to thank all people, I've spoken to about technical details of my work to complete my thesis. I would specially thank my supervisor Prof. Dr. Ivan Perić that he enabled me to write the thesis at his institute and funded my work financially. My advisor Roberto Blanco helped me when I was stuck at some point, although he wrote his doctoral thesis. I would also like to thank all office co-workers. With some of them I had a brief technical exchange. I would specially thank Helge Wurst for spending many hours of deep physics related discussions with me. I would also like to thank Prof. Dr. Babak Parkhideh from the *University of North Carolina at Charlotte* for the preliminary internship during the summer of 2017 at which I were introduced into the topic of high-bandwidth current sensing and for his support during this thesis.

Contents

Abstract	i
Acknowledgement	ii
1 Introduction	1
1.1 Motivation	1
1.2 Requirements/Primary Aims	1
2 Sensor Selection	3
2.1 Steady field capable sensors	3
2.2 High-frequency sensors	4
2.3 Investigation Results	4
3 Introduction to Magnetoresistors and Rogowski coils	5
3.1 Magnetoresistors	5
3.1.1 Properties of different magnetoresistors	5
3.1.2 Hysteresis	6
3.1.3 Measurement methods	7
3.2 Rogowski coil	11
3.2.1 Planar Rogowski Coil	13
3.2.2 Integration of the coil signal	13
4 System Design	15
4.1 The ideal sensor	15
4.2 The real sensor design	15
4.2.1 Magnetoresistor placement	15
4.2.2 Current Trace	16
4.2.3 Rogowski coil	17
4.3 Sensor fusion of the Magnetoresistor and Rogowski coil	23
4.4 Sensor Interface	26
5 Magnetic Field Simulation	27
5.1 Introduction	27
5.2 Tools	27
5.3 Simulation details	27
5.4 Effort reduction	29
5.4.1 Assumptions for calculations	29
5.4.2 Proof	29
5.4.3 Conclusion	32

5.5	Introduction to Magnetoresistor placement	32
5.6	Postprocessing	33
5.6.1	Principle	33
5.6.2	Workflow	33
5.6.3	Objective function	34
5.6.4	Explanation	36
5.6.5	Trajectory extraction	38
5.6.6	Conclusion	40
5.7	Result	40
6	Sensor Structure	42
6.1	Introduction	42
6.2	Rogowski coil equivalent circuit	42
6.3	Design Considerations	44
6.3.1	Attaching the trace to the sensor board	44
6.3.2	Galvanic Insulation	44
6.3.3	Targeted dimensioning	46
7	Experimental Setup	49
7.1	Evaluation of Current Pulse Generators	49
7.1.1	Avalanche Pulse Generator	49
7.1.2	Short-Circuit Switch	49
7.1.3	Full-bridge bidirectional pulse generator	50
7.2	Prototype (V1)	51
7.2.1	DC-Link Capacitor	51
7.2.2	Shunt	52
7.2.3	Half-Bridge	53
7.2.4	Sensor Adapter	54
7.2.5	Device Under Test	54
7.3	Measurement setup	57
7.3.1	Power Supply	57
7.3.2	Oscilloscope	58
7.3.3	Pulse Generator	58
7.3.4	Readout equipment	58
7.4	Experiments	58
7.4.1	Frequency response	58
7.4.2	Hysteresis measurement	59
7.4.3	Degaussing	60
7.5	Conclusion (V1)	62
7.6	Prototype (V2)	62
7.6.1	Circuit Simulation	62
7.6.2	Hardware	63
7.7	Measurement Results (V2)	66
7.7.1	Double Pulse	66
7.7.2	Bandwidth Characterization	67

7.7.3 Explanations	67
8 Outlook	74
9 Summary and Conclusion	75
List of Figures	76
List of Tables	78
List of Algorithms	79
Bibliography	80
A Appendix: Circuit Diagram for hardware version 2	83
B Appendix: Vishay pulse energy calculator	85

1 Introduction

1.1 Motivation

In today's world of power converters, one research goal is to reduce the weight, the size and the cooling effort e.g. for mobile applications. Another goal is to increase the efficiency of buck converters under light load conditions. One way to achieve this is to use fast switching semiconductors. The newest generation of gallium nitride semiconductors support switching frequencies higher than 100 MHz¹.

At the market, there are not yet any cost-effective high bandwidth current sensors available, which can be integrated easily in a standard converter design. An other use case for high bandwidth current sensors is detecting short circuits before the semiconductor will fail. This does not necessarily need to be a DC-capable sensor, but it would be one supplemental use case.

This work is based on previous work and ideas of Dr. Parkhideh's team at PIL (PV Integration Laboratory)² at EPIC (Energy Production and Infrastructure Center)³ at UNCC (University of North Carolina at Charlotte)⁴ where i worked as a research assistant during my six months internship from April to September 2017.

The main focus for this thesis is to understand the physical principle of the current sensor used at PIL/EPIC/UNCC and showing ways and implementations to improve its performance.

1.2 Requirements/Primary Aims

To get started, a few design requirements have to be listed to reduce the degrees of freedom for this work:

- Nominal design current: $I_{nominal} = \pm 100$ A
- Nominal design bandwidth: $B_{nominal} = 100$ MHz
- Measuring direct and alternating currents
- Bipolar current measurement
- Galvanic insulation

¹GaN Systems: GS66516T

²<https://coefs.uncc.edu/bparkhid/pv-integration-laboratory/>

³<https://epic.uncc.edu/>

⁴<https://www.uncc.edu/>

- High linearity
- Small footprint
- Easy production
- Low cost
- Overload ability
- Low-power consumption
- High noise immunity
- Easy usage

2 Sensor Selection

To fulfill the requirements from [section 1.2](#), a few types of sensors will be described shortly in this chapter. Later on, the sensors which will be used in this thesis will be set and explained in the following chapters.

2.1 Steady field capable sensors

For measuring direct currents, a sensor is needed that can measure steady magnetic fields generated by a conductor with a direct current applied. There are a few sensors that fulfill the most requirements but do not fulfill the full bandwidth requirement. With the required galvanic insulation, sensors like shunt resistors are not possible. The remaining common types of sensors are^[1]:

- Magneto resistors (AMR, TMR, GMR) (open- and closed-loop)
- Hall-effect sensors (open- and closed loop)
- Fluxgate sensors
- Fiber-optic current sensors (FOCS)

FOCS are very bulky and expensive sensors for high and highest voltages measuring currents in the range of kA-MA.

Fluxgate Sensors require relatively complex control electronics which is in general handled by using an ASIC chip.

Hall effect sensors do have a very little output voltage compared to other sensor types. The bandwidth of hall effect sensors is in the range of a few kHz.

The magneto resistive effect is based on a resistance change in a specific material when a magnetic field gets applied into the sensitive axis. Within magneto resistors, there are different sensing concepts at the market. The most popular are AMR¹, GMR² and TMR³. These magneto resistive structures and can be integrated in a very small area.

¹Anisotropic magneto resistance

²Giant magneto resistance

³Tunnel magneto resistance

2.2 High-frequency sensors

In general high-frequency sensors use the Faraday law of induction. These sensors can only measure direct current after integrating the sensors output which is very hard at high accuracy because of offset errors.

In the following bullet list, a few common AC sensors are listed:

- Current transformer
- Rogowski coils
- Fiber-optic current sensors (FOCS)

Current Transformers are using a pretty bulky core for high currents and a DC offset saturates the core.

Rogowski coils are basically an air coil around the current-carrying trace. The air core is not subject to any saturation effects which results in a very good overload behavior.

Fiber-optic current sensors were introduced in the last section.

2.3 Investigation Results

With commercial current sensors it is not possible to measure fields with a frequency range from $f_0 = 0$ Hz to more than $f_1 = 10$ MHz at low cost. These requirements call for the use of two sensors merged together using an intelligent sensor fusion algorithm. Because the sensor has to be split into a high-frequency and a low-frequency part, both sensor concepts can be developed independent from each other.

For this thesis, magneto resistors should be used as low-frequency sensors and rogowski coils as high-frequency sensors.

These two sensors can later be merged. Basically the low-frequency sensor will be cut off at a certain frequency and the high-frequency sensor will start at the same frequency. This is described in detail in [section 4.3](#). The proposed frequency will be in the range of 0.5 MHz to 2 MHz.

3 Introduction to Magnetoresistors and Rogowski coils

As shown in [chapter 2](#), the current sensor should be built using magnetoresistors and Rogowski coils. In this chapter, a brief introduction to these sensing devices will be given.

3.1 Magnetoresistors

Magnetoresistor (MR) elements react to the magnitude of an external magnetic field in their intrinsic sensing direction by a change of resistance. This electric resistance can be measured for example using a voltage divider or a Wheatstone bridge. Several physical effects give rise to the phenomenon of magnetoresistance. In this thesis only those of commonly available sensors for current measurement will be considered. The development of magnetoresistive technologies or in more general terms “magnetic field sensors” has in recent years been driven by the field of high density data storage, yielding great advances in manufacturing and miniaturization but unintentionally making linearity and absolute measurement a secondary objective. Especially in GMR and TMR sensors a certain amount of hysteresis is observed which can be linked to the behavior of ferromagnetic domains and domain walls at the nanometer scale. For current sensing, only three common types of sensors are available at the market.

- Anisotropic magnetoresistance (AMR, discovered ≈ 1856 [2])
- Giant magnetoresistance (GMR, discovered ≈ 1988 [3])
- Tunnel magnetoresistance (TMR, originally discovered ≈ 1975 [4], usable since ≈ 2000)

3.1.1 Properties of different magnetoresistors

To give an overview [Table 3.1](#) lists selected properties of the most common magnetoresistive effects. Other aspects include saturation behavior and linearity which are easily illustrated by the response of the output voltage ([Figure 3.1](#)) to the magnetic field H . An ideal sensor should have a bijective¹ transfer function to allow unambiguous reconstruction of the sensed current from the sensor voltage. The AMR effect does shift to side valleys when the sensor is driven in saturation which makes it mandatory to implement a reset circuit². The GMR sensor transfer function has rectification characteristics which makes it nearly unusable for

¹A bijective function has a one-by-one representation where the function converting from one parameter vector to another parameter vector is unambiguous.

²An AMR reset circuit is shown in the datasheet of the Honeywell HMC1021 sensor [5].

	AMR	GMR	TMR
effect	Anisotropic magnetoresistive	Giant magnetoresistive	Tunnel magnetoresistive
sensitivity $\left[\frac{R(H)-R(0)}{R(0)} \right]$	20 %	80 % [6]	230 % [7]
comments	needs set/reset circuitry because of overcurrent	self rectifying	low hysteresis

Table 3.1: A comparison of general properties for different magnetoresistive effects

manufacturer	Crocus Technology Inc.	Sensitec GmbH	MultiDimension Technology Co., Ltd.
magnetoresistor	CT219 [8]	TF952 [9]	TMR2103P [10]
sensitivity $\left[\frac{mV}{\sqrt{mT}} \right]$	15 ⁱ	7	0.6
Linear Range [mT]	depends on applied counter field current	± 20	± 3
Hysteresis Error	1% FS ⁱⁱ	0.05 mT ⁱⁱⁱ	0.03 mT ^{iv}
sensing concept	half bridge with feedback resistors	Wheatstone bridge	Wheatstone bridge
comments	in production / samples	in development / samples	small quantities only available via amazon marketplace

ⁱ According to the datasheet[8] in a closed loop configuration. ⁱⁱ Full Scale

ⁱⁱⁱ Measured: 5 mT \rightarrow -5 mT \rightarrow 5 mT ^{iv} @ ± 3 mT

Table 3.2: A comparison of properties from selected TMR sensors. The sensitivity cannot be compared directly because they feature different measurement concepts.

bidirectional current sensing. The TMR effect shows a similar behavior as the AMR effect, but does not decrease its output voltage on high magnetic field values as much as AMR sensors do. The effect that best matches current sensing applications is the tunnel magnetoresistive effect due to its low hysteresis and the easily interpretable transfer function. Table 3.2 shows three selected TMR sensors. The sensors from *Sensitec GmbH* and *Crocus Technology Inc.* were procured for experiments over the course of this thesis.

3.1.2 Hysteresis

All magnetic sensors have some degree of hysteresis due to the sensor material becoming magnetized. Figure 3.2 shows a general hysteresis curve with the corresponding characteristic points.

The *saturation magnetization* B_S describes the point where an increase in magnetic field does not lead to an increase of magnetic flux density.

The *magnetic coercivity* H_c can be measured when driving an demagnetized sensor with an external magnetic field into saturation and then reversing the field slowly, until the magnetic

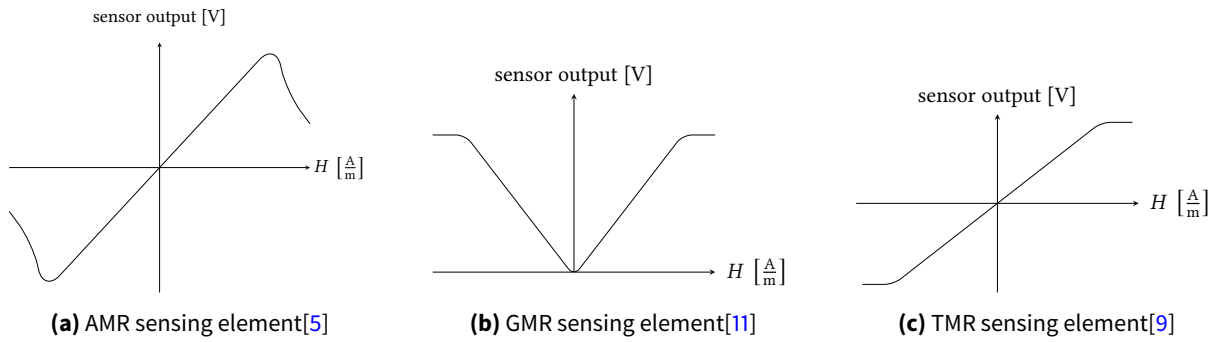


Figure 3.1: Simplified transfer functions for AMR, GMR and TMR. Saturation causes AMR sensors to latch into a side valley from which it needs to be reset by using a reset circuit. GMR sensors do not have saturation problems but do rectify the input. TMR sensors driven into saturation only show a very small decrease in output voltage during saturation.

flux density is restored to its initial value.

The *remanent magnetization* \mathbf{B}_R describes the residual magnetic flux density and remanence, respectively, when removing external field sources after the sensor was driven into saturation. Hysteresis describes a memory effect, because the offset results from a saturation event and persists beyond that. While an intended behavior in hard disk drives, for current sensors this effect ought to be minimized. As a precaution not to reach saturation the sensors should only be operated in its linear range. The flatness in all graphs of Figure 3.1 at the end of the measurement range describes the *saturation magnetization* \mathbf{B}_S and does not reflect the limit of the voltage supply.

When exceeding the linear range of a magnetoresistor, an offset of the output of the sensor is introduced in the form of hysteresis. While it will not damage the sensor, it causes a permanent offset even after a powercycle. To revert persistent changes, it is possible to degauss the sensor. A common principle for degaussing is described by *NVE Corporation*[12, External Magnetic Fields and Hysteresis Effects][GMR] and *Honeywell*[5, 'Set/reset drive circuits' and Figure 6][AMR]. They mainly drive the sensor into saturation towards both extremes of the hysteresis loop $+\mathbf{H}_{\text{demagnetize,pk}} \rightarrow -\mathbf{H}_{\text{demagnetize,pk}}$ and then reduce the amplitude within two or four pulses while the state of the sensor spirals inwards to zero remanence. The need for degaussing is a big challenge when using AMR sensors, but extends to GMR and TMR applications as well.

3.1.3 Measurement methods

TMR and AMR sensor output resistance can be modelled using a linear coupling between the resistance $R_{MR}(H)$ and the magnetic field \mathbf{H} (Equation 3.1). This simplification can of course only be used over a limited range where the sensor is not in saturation and hysteresis is insignificant with respect to overall accuracy limits. $C_{\text{sensitivity}}$ will be a scalar with the unit $\frac{\text{V m}}{\text{A}^2}$.

$$R_{MR}(\mathbf{H}) = R_{MR_{\text{base}}} + C_{\text{sensitivity}}\mathbf{H} \quad (3.1)$$

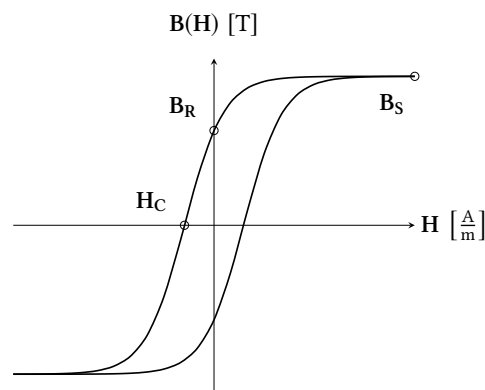


Figure 3.2: An exemplary hysteresis curve with three key parameters *saturation magnetization* B_S , *magnetic coercivity* H_C and *remanent magnetization* B_R .

The sensors can be measured using a regular voltage divider, in a half bridge, or a full bridge (Wheatstone bridge) configuration. Open-loop and closed-loop configurations have to be considered, too.

3.1.3.1 Voltage divider and half/full bridges

- A regular voltage divider shown in [Figure 3.3a](#) will only have one sensing element in either the lower or upper branch. This circuit has issues with temperature and offset stability.
- The push-pull half bridge in [Figure 3.3b](#) consists of two sensing elements where one is positioned to measure the inverse effect of the first one. This will double the output voltage range, makes the sensors more linear while also reducing common-mode noise. One problem is the current drawn by a sensing circuit which can be described by using the formula for a loaded voltage divider. The load current will give rise to offset errors.
- As far as the last method, a full-bridge setup (Wheatstone bridge) will reduce output loading problems by providing a fully symmetric structure ([Figure 3.3c](#)). For linearity reasons, all four resistors have to be positioned close to each other and preferably on the same die³. The resistors should ideally be subjected to the same environmental changes, e.g. temperature and magnetic field. If the half bridges are separated, their temperatures will differ dynamically which leads to non-compensable measurement errors.

There are two versions of Wheatstone bridges: one with four and one with two sensing elements. For the two-element full-bridge, the insensitive resistors usually only shielded sensing elements which share the temperature and resistance characteristics of the adjacent sensing elements. This leads to good temperature compensation and reduces offset errors. When using four elements, the output range doubles.

³An integrated circuit cut from a wafer.

The Wheatstone bridge is the preferred measurement arrangement due to good temperature stability and the inherently differential output. Most sensors are available in the Wheatstone bridge configuration (Figure 3.3c) or half-bridge configuration (Figure 3.3a, Figure 3.3b).

3.1.3.2 Open vs closed loop measurement

So far the direct measurement of a magnetoresistive effect where the sensing element is subjected to the full swing of the external magnetic field were discussed. A different sensing topology introduces closed-loop control to force zero change in magnetoresistivity. This requires a means to generate a superimposed magnetic field counteracting the external field locally - at the microscopic location of the sensing element.

Closed-loop control as shown in Figure 3.3d allows extending the measurement range while keeping the sensor bounded to a region of its magnetization curve where its response is linear. Closing the loop unfortunately introduces new problems: If the net flux density is out-of-range at any point in time the sensor element is driven into saturation and the sensor signal will thereby acquire a DC offset. As far as external flux density is concerned, open loop sensors do not have this kind of problem as they need to be rated for the maximum flux density that can occur at any point in time. The bounds of linear operation can also be exceeded in other ways: real feedback circuits are limited in both output voltage swing as well as bandwidth, adding clipping, saturation recovery and finite bandwidth to the list of causes.

If the characteristics of a sensor can change by applying a high field like it's the case with AMR sensors (change in sensitivity), closed loop has to be considered with special care. Ultimately closed-loop sensors are inherently slower than open-loop sensors while offering in principle larger sensing range and better linearity.

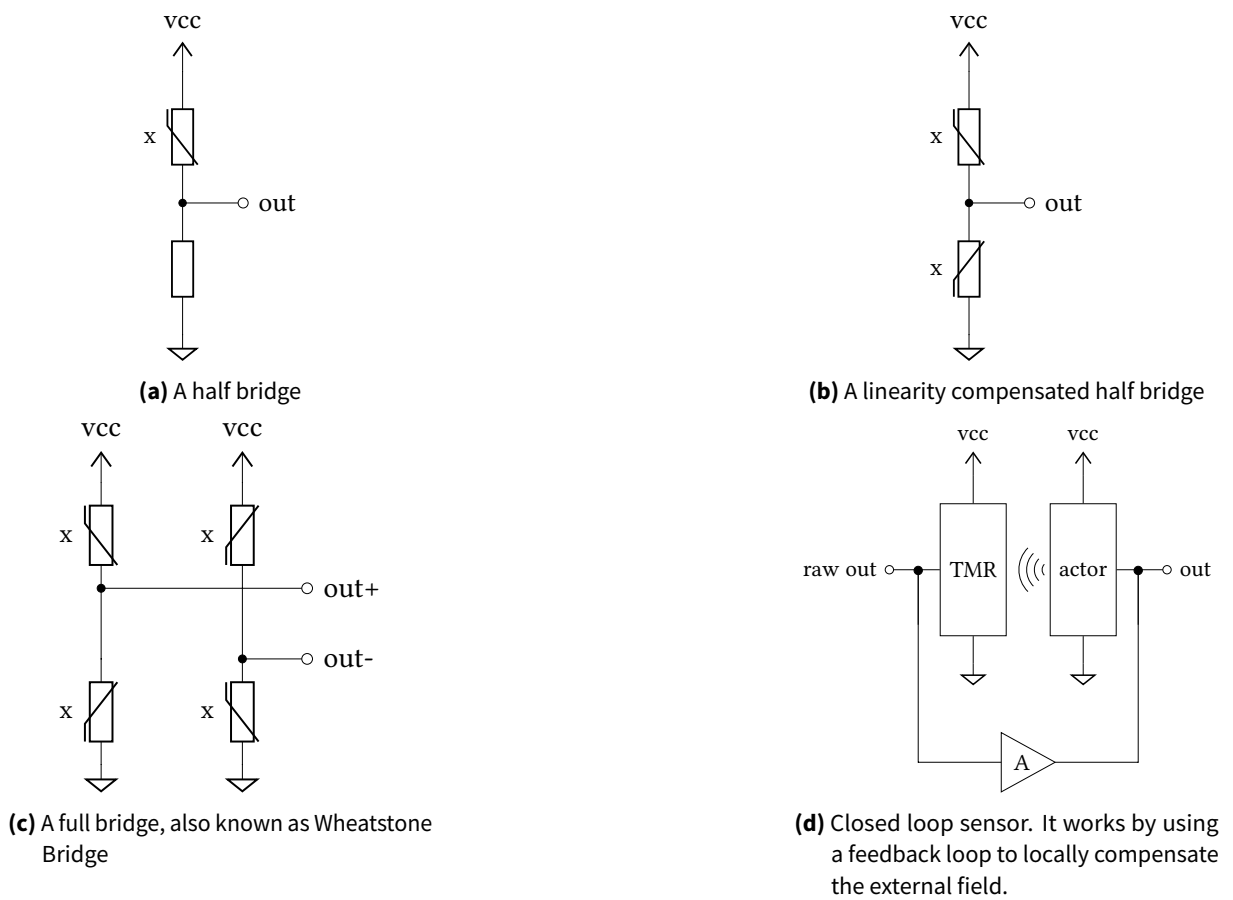


Figure 3.3: Different measurement methods for magnetoresistor sensors.

3.2 Rogowski coil

The Rogowski coil was invented in 1912 by Walter Rogowski [13] at the German metrology institute *Physikalisch-Technische Reichsanstalt* (PTR). It is an air core toroidal coil as shown in Figure 3.4 and sketched in Figure 3.5. This coil is used to measure the change in the encircled poloidal magnetic flux caused by current in a central power conductor. It is essentially a weakly coupled transformer that samples an AC current $\frac{di(t)}{dt}$ via its induced voltage $u_i(t)$. In the following paragraph, a mathematical derivation based on [14, chapter 4.2] will attempt to explain the formal working principle of the Rogowski coil.

The Rogowski coil working principle is that of a weakly coupled sensing transformer. Where the coupling is described in *Ampère's circuital law* (Equation 3.2) and the induction voltage is described in *Faraday's law of induction*. It connects a closed line integral of the magnetic flux density proportional to the enclosed current. The line integral shows, that only the enclosed fields will be added to the result with no respect to the chosen integration path. The coil (Figure 3.5) has a perimeter of l with n loops with a distance Δs between each turn which are wound in normal direction around a current-carrying wire and encloses the area A . In the simplified *Faraday's law of induction* in Equation 3.3 the induction voltage results from the integral of the time-varying perpendicular field components of the area of the coil loops. The closed line integral in Equation 3.2 can be written as a sum for small Δs as Equation 3.4 using $\Delta s n = l$. This leads with Equation 3.3 to Equation 3.5. The coupling between wire and coil is M . The coupling between the current-carrying wire and the Rogowski coil is weak and with ideally no current flowing through the Rogowski coil, there is almost no reverse coupling to the wire. This concept is the main difference to a current transformer.

The major geometrical problem real Rogowski coils have is that the individual turns of the coil can hardly be fully aligned with the normal axis of the current-carrying wire. An optimal model of an Rogowski coil would consist of a set of flat coils arranged along a ring, each being oriented perpendicular to the flux passing through. This differs from the usual toroidal winding shape, the turns of which continually accumulate angular pitch as they wrap around the toroidal surface, leading to turn segments that are tilted out-of-plane, thus sensing non-poloidal field components. To circumvent this geometric problem a cross-wrapping can be performed which was proposed in [14, figure 187, page 169]. A Cross-wrapped winding consist of two Rogowski coils with opposite handedness and a connection at the far end instead of one Rogowski coil and a return wire. This winding geometry cancels non-poloidal contributions of the \mathbf{B} -field as at each point there are partial turns tilted in opposite directions by the same amount which cause error voltages of opposite signs, cancelling out-of-plane contributions as the turns voltages add up from terminal to terminal.

$$\oint_C \mathbf{B} \, ds = \mu I \quad (3.2)$$

$$u_i(t) = A \sum_{v=1}^n \frac{dB_v}{dt} \quad (3.3)$$

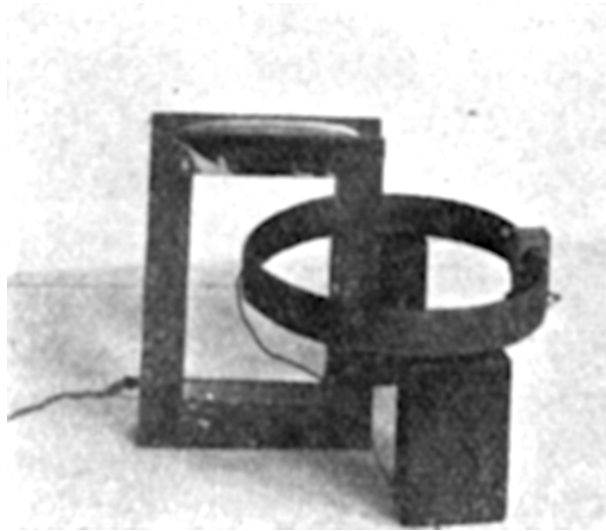


Figure 3.4: One of the experiments for measuring the magnetic induction voltage carried out by Walter Rogowski[13, Fig. 4] in 1912 at the German metrology institute *Physikalisch-Technische Reichsanstalt*(PTR).

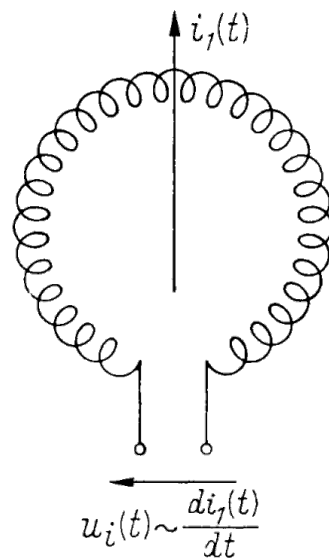


Figure 3.5: Schematic of a Rogowski coil [14, Figure 186]

$$\sum_{v=1}^n B_v \Delta s = \mu i(t) = \mathbf{B}_v l \quad (3.4)$$

$$u_i(t) = \frac{An\mu}{l} \frac{di(t)}{dt} = M \frac{di(t)}{dt} \quad (3.5)$$

3.2.1 Planar Rogowski Coil

In pursuit of the goals set forth for this thesis, an inexpensive and easy-to-build Rogowski coil should be used. Two coil windings can be realized in PCB technology as a planar coil. They can be thought as a quadrupole H-field probe or as an approximation to a Rogowski coil where Δs is very small, or even 0 (the coil is considered planar) and only a small angle of the regular coil will be covered. This type of coil has been described in “High-Impulse Current and Voltage Measurement”[15] as the *Magnetic Probe Method*.

This coil type is obviously not a conventional Rogowski coil anymore and Equation 3.5 no longer applies. The concept of equidistant loops along the perimeter of the current trace hardly applies. When using a pair of such planar coils, they can measure the opposite field (e.g. both side of a current-carrying wire) and can then be subtracted. This results in cancellation of external homogeneous field components (common-mode rejection) while doubling the signal amplitude due to symmetry (differential mode). But there are some other possibilities to consider. They will be covered in the next chapter.

3.2.2 Integration of the coil signal

To obtain a sensor voltage $u_m(t)$ proportional to the main current $i(t)$, the Rogowski coil signal needs to be integrated over time. This can be done using different methods.

A *LR-lowpass* can use the (precisely measured) self inductance of the coil and only needs a low inductance resistor for the integration.

A *RC-lowpass* is a more commonly used approach, because knowledge and control of the exact value of the self inductance is not important. Note that enlarging the coil at the far leaves the coupled mutual flux essentially unchanged but proportionally enlarges self-inductance. The filter design described in the following is shown in Figure 3.6 and can also be found in [14, chapter 4.2]. The lower cutoff frequency is defined by the first order RC low pass (Equation 3.6) and the higher cutoff frequency by the load connected to the coil (Equation 3.7). When the above conditions are met, the resulting measured voltage will be directly proportional to the current in the frequency range (Equation 3.8) of f_{low} and f_{high} .

$$f_{low} \gg \frac{1}{2\pi RC} \quad (3.6)$$

$$f_{high} \ll \frac{Z}{2\pi L} \quad (3.7)$$

$$u_m(t) = \frac{1}{RC} \int u_i(t) dt = \frac{M}{RC} i(t) \quad (3.8)$$

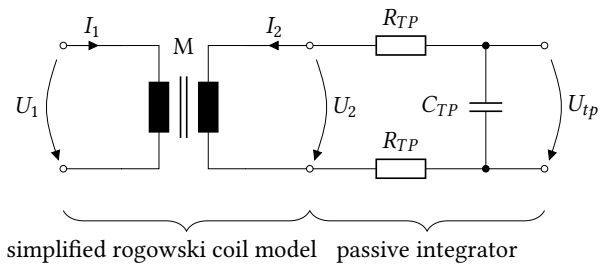


Figure 3.6: Schematic for a low-pass filter after an simplified Rogowski coil equivalent circuit. The equivalent circuit is derived in [section 6.2](#) in detail. The low-pass filter integrates the coils signal starting with the cutoff frequency of the low-pass.

4 System Design

In the last chapter, different sensing concepts for building a current sensor were presented. In this chapter, the focus will be the design and the construction of a real current sensor. The components of it were selected in the last chapter namely a tunnel magnetoresistor (TMR) and a Rogowski coil. Now the current trace and the secondary electronics will be examined.

4.1 The ideal sensor

The ideal current sensor would have the following properties in addition to the previously collected requirements in [section 1.2](#):

- Low inserted inductance into the primary current trace
- Close to ideal frequency characteristics with a very high bandwidth
- Low reverse coupling into the current trace when measuring the current using the sensing elements
- High noise rejection

The inserted inductance can be minimized by using a coaxial current trace as described in “Wide Bandwidth Current Sensor Combining a Coreless Current Transformer and TMR Sensors”[16]. This leads in general to a very bulky construction.

The ideal frequency characteristic is not possible, because every sensor has only a limited bandwidth (see the Shannon-Hartley theorem¹). For coils, the resonance frequency has to be considered.

The influence of the current trace and the sensor can be minimized, but leads to a lower coupling and the signal-to-noise ratio (SNR) will decrease.

4.2 The real sensor design

4.2.1 Magnetoresistor placement

To get an idea of how to position the magnetic field sensor, the way the field circulates around the trace and in which axis the sensor is sensitive has to be studied. The magnetic flux density \vec{B}

¹Shannon-Hartley theorem: A channel can only have a limited bandwidth with respect to the surrounding noise. The Channel is the magnetic field connecting the current and the pickup coil.

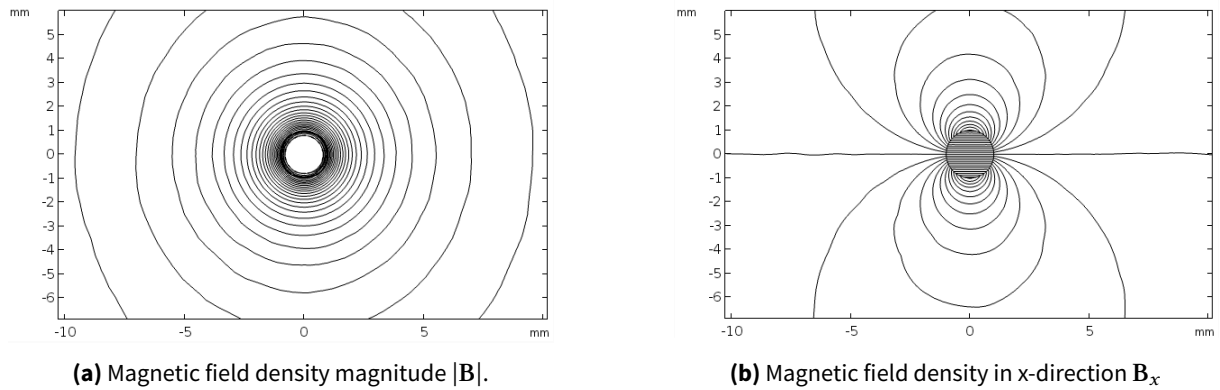


Figure 4.1: The magnetic field generated by a circular current-carrying wire. Crosssectional view with trace at $I = 100$ A. The horizontal axis is the x-axis, the vertical axis the y-axis and the axis into the paper is the z-axis. The left plot describes the magnitude of the magnetic flux density. The right plot describes only the x-axis component which is able to be measured using a single axis magnetoresistor. Both plots are valid from 10 Hz to more than 100 MHz. The magnitude changes over frequency according to [Equation 4.2](#).

of a straight current-carrying wire can be described in cylindrical coordinates as of [Equation 4.1](#). The magnitude of this vector ([Equation 4.2](#)) is depicted as a plot in [Figure 4.1a](#).

$$\vec{B}(r, \varphi) = \frac{\mu_0 I}{2\pi} \frac{\vec{e}_\varphi}{r} \quad (4.1)$$

$$B(r) = |\vec{B}(r, \varphi)| = \frac{\mu_0 I}{2\pi} \frac{1}{r} \quad (4.2)$$

$$\vec{B}(x, y) = \frac{\mu_0 I}{2\pi} \frac{x\vec{e}_y - y\vec{e}_x}{x^2 + y^2} \quad (4.3)$$

$$B_x(x, y) = \frac{\mu_0 I}{2\pi} \frac{-y}{x^2 + y^2} \quad (4.4)$$

All common sensors measure the magnetic flux density in at least the x-direction but do not measure the absolute value in all three dimensions. The sensors available for this thesis support x- and/or y-axis measurements. The field in y-dimension should be 0 mT under the assumption of an infinite long, straight current-carrying wire. The remaining axis is now the x-axis. The resulting field of a wire can now be calculated by transforming [Equation 4.1](#) from cylindrical coordinates to Cartesian coordinates ([Equation 4.3](#)) and then only plot the x-direction part of \vec{B} ([Equation 4.4](#)). For verification a plot of the B_x is depicted in [Figure 4.1b](#).

For a circular wire, the magnetoresistors should be placed on top in extension of the center of the trace. The exact placement will be dependent on the trace shape and other parameters. This will be optimized in [chapter 5](#).

4.2.2 Current Trace

The goal for a real sensor is to achieve the lowest possible inserted impedance but easy to produce current trace. The first approach would be a single rectangular copper trace shown in



Figure 4.2: A U-shaped current trace with a trace width of 5 mm, a trace thickness of 2 mm and a trace gap of 2 mm.

[Figure 4.3a](#) and [Figure 4.3b](#). A sensor PCB mounted flat onto the converters PCB would use a lot of space on a circuit board. An upright position would reduce the footprint but involves that the trace needs a return wire. One solution would be a rectangular shaped trace that runs from the backside of the trace to the top of the board on the front side and runs back where the trace started. The paper “Hybrid Magnetoresistor-Planar Rogowski Current Sensing Scheme With Folded Trace Magnetic Field Concentration Technique”[\[17\]](#) describes this approach. It leads to a uniform magnetic flux density between the traces, but requires a more complex copper shape and a mechanically fixed sensor would not be easy to realize for mass production.

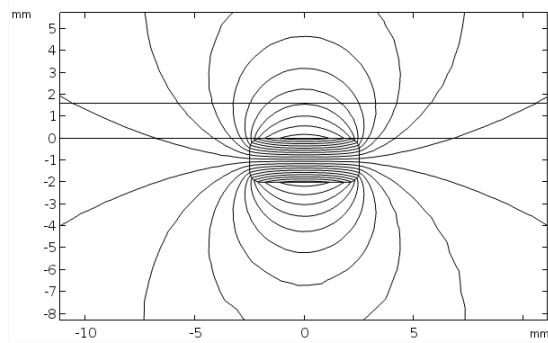
Another approach could be a U-shaped flat trace. A milled U-shaped trace is shown in [Figure 4.2](#). It combines the return wire with an easy punch press production. One side effect is the possibility to measure the magnetic fields for magnetoresistors fully differential. The inductance can be minimized, because the high-frequency current will only run at the inner surfaces of the U-shaped trace. The corresponding fields will concentrate within the gap. This can be explained by viewing at an crosssectional drawing [Figure 4.3c](#) and [Figure 4.3d](#) with a sentence from Jim Williams from Linear Technology: "A wire's inductance is defined as the energy stored in the field [surrounding it.]"[\[18, p.23\]](#).

4.2.3 Rogowski coil

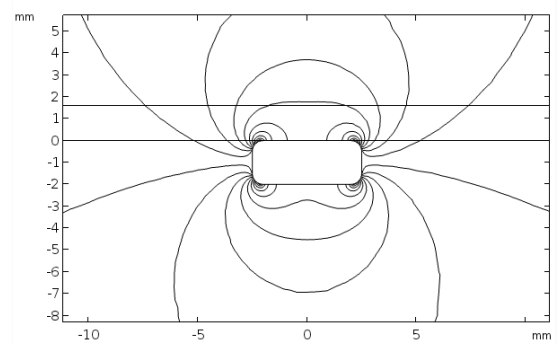
The planar Rogowski coil was introduced in [subsection 3.2.1](#). In this section, the preliminary placing should be constructed.

Using a Rogowski coil in the commonly known manner as a toroidal coil around a trace leads to a high space consumption and a more or less expensive coil construction. The result has a fixed dependency of the current to measure ([Equation 3.5](#)). Another way to use the Rogowski coil effect is to build planar Rogowski coils (see [subsection 3.2.1](#)). This can be imagined by folding the toroidal coil flat onto a piece of paper and reduce the number of turns.

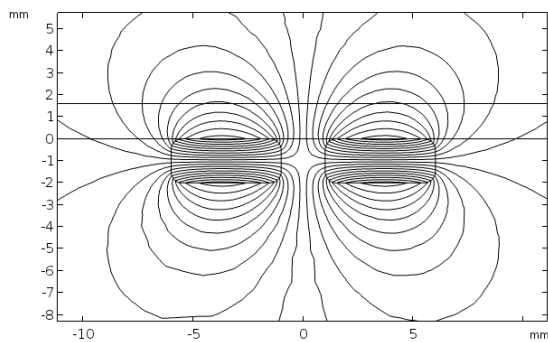
Due to the skin effect, the magnetic field radiated by a rectangular shaped current trace concentrates around the corners. These fields can be collected by a planar coil. Another problem with the planar coil comes with the partial perimeter of the current trace covered by the coil loops: The coil will not only collect a part of field emitted by the current trace, it also collects unwanted external fields. This leads to two problems: There is noise from external fields and there is no straight forward formula between current and collected field as for the traditional Rogowski coil.



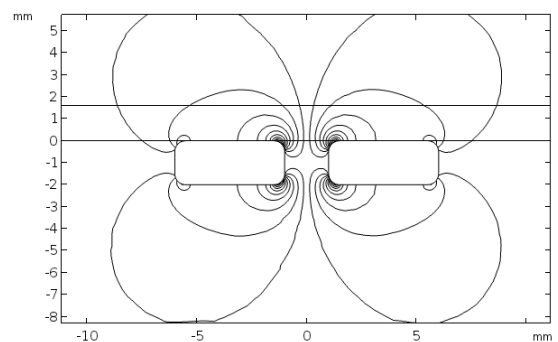
(a) B_x for single rectangular trace, $f = 10$ Hz



(b) B_x for single rectangular trace, $f = 100$ MHz



(c) B_x for two rectangular traces, $f = 10$ Hz



(d) B_x for two rectangular traces, $f = 100$ MHz

Figure 4.3: The magnetic field generated by one or two current-carrying traces. Crosssectional view with trace below PCB, $I = 100$ A, $f = 10$ Hz \rightarrow 100 MHz. The coil placement is described by the horizontal lines inside the PCB.

The second problem can be solved by calibrating the output by driving the current carrying trace with a precise measured current. For example, a shunt can be used, due to the fact it is able to measure at high frequencies. It is not necessary that the test equipment measures galvanic insulated.

To solve the first problem, three major possible coil and current trace arrangements will be introduced:

As an explanation in advance: The output of two coils can be added by connecting them in a way that their rotation direction matches. For subtracting, their rotation directions have to be reverse to each other. The shape of the coil does not matter for the first contemplation and will be explained in more detail in [chapter 5](#).

The first possibility shown in [Figure 4.4](#) are two planar coils on top of a single current trace with no return path. This configuration was used in [19]. This configuration will reduce common mode fields by subtracting the homogeneous field from each other. Because the current is sensed on both sides of the conductor, the output amplitude will be doubled. A drawback is the need of a return wire which will increase the inserted inductance. Another clear drawback is that magnetoresistors could not be placed in a differential configuration onto the same height because of the single current trace configuration.

The second possibility shown in [Figure 4.5](#) are two planar coils located on top of a current trace and its return trace which are located close together. This configuration tries to compensate the drawbacks of the first possibility but fails on the common mode rejection. In the end the inserted inductance can be minimized and the magnetoresistors can sense the fields in a differential manner. The coils response is also doubled by adding both coil outputs, which does unfortunately also double common mode fields.

The third possibility would be a single coil centered between the trace and its return trace as shown in [Figure 4.6](#). It features a very high output amplitude. The main challenge would be the minimization of the gap between the traces for low inductance and the area of the coil needs to be maximized for a high response. To minimize the effects from external fields, this setup could probably be shielded. To build this type of coil a manufacturing process featuring very thin wires is necessary to keep the gap as small as possible. Buried vias are most likely also required.

For this thesis, the first possibility was used in the beginning and later on switched to the second approach because the differential magnetoresistor placement was also a very mandatory and the low inserted inductance was considered to be more important.

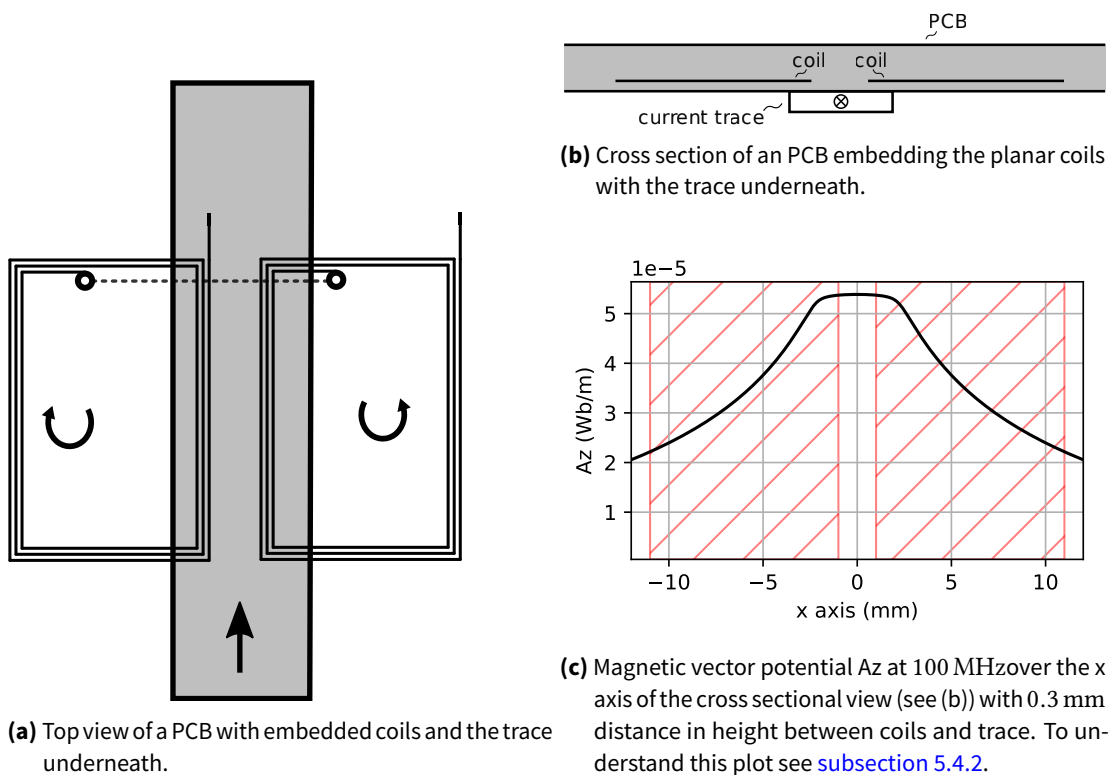


Figure 4.4: The first possibility to place coils on top of an single conductor. The main advantage is the common mode rejection.

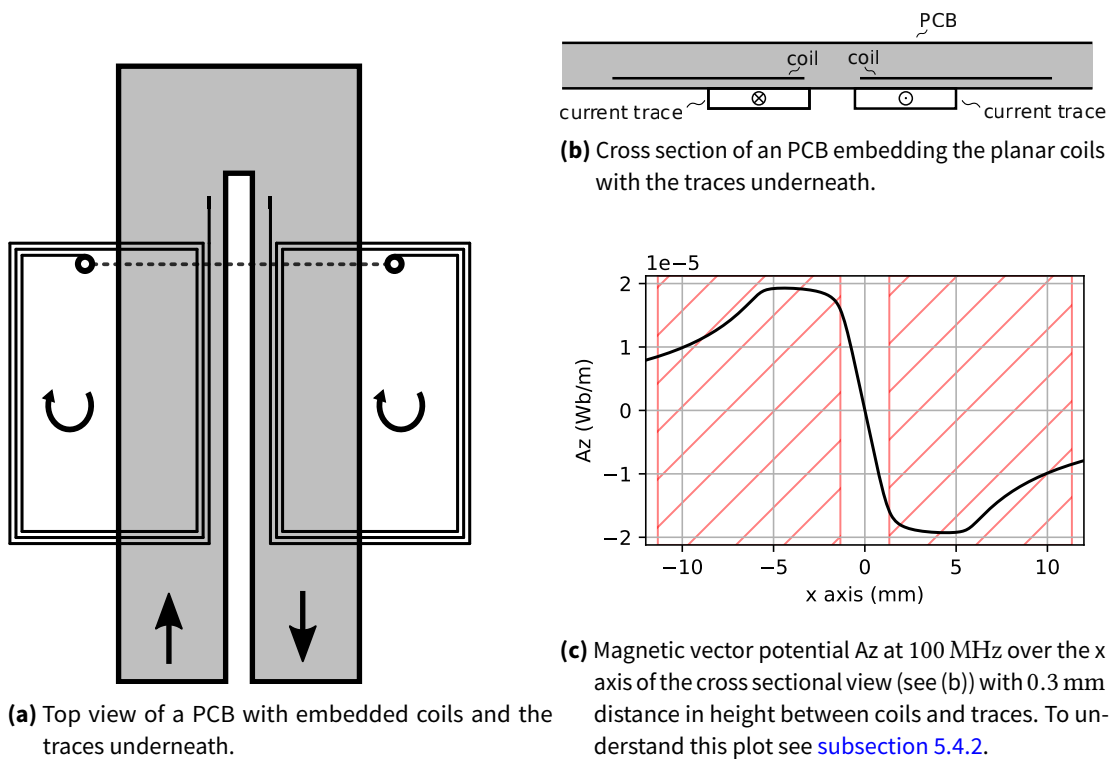


Figure 4.5: The second possibility to place coils on top of an U shaped conductor. The main advantage is the reduced inserted inductance and the possibility to place the magnetoresistor in a differential manner.

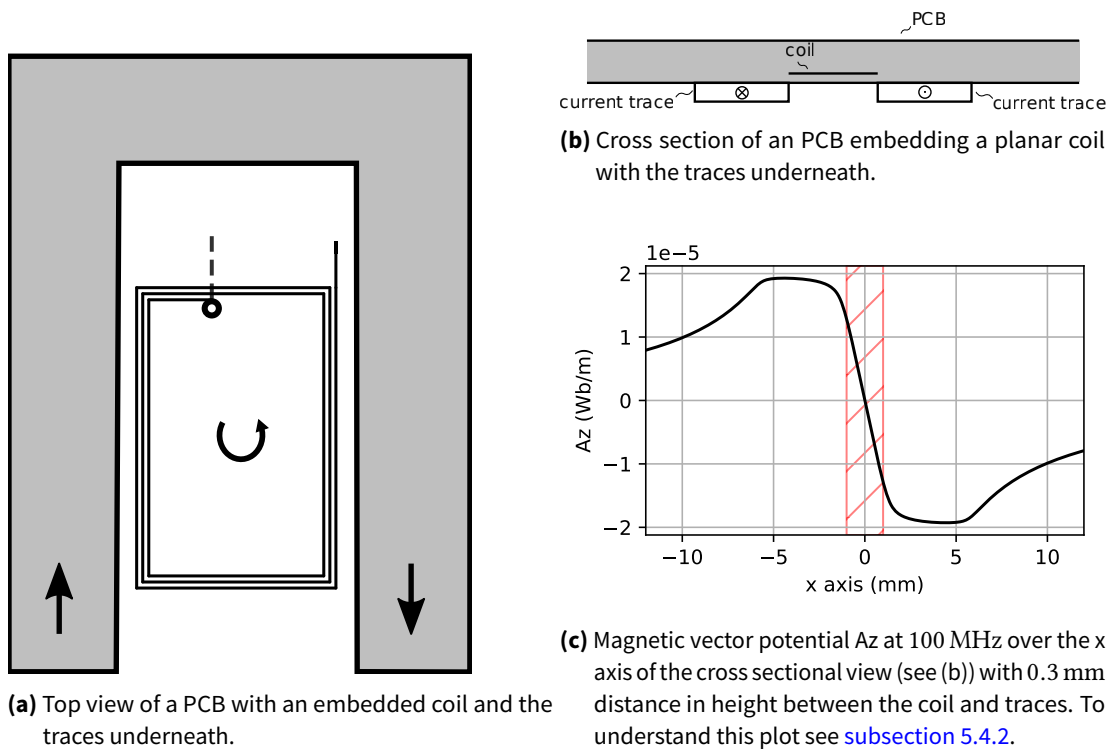


Figure 4.6: The third possibility to place a coil on top of an U shaped conductor. The main advantage is the reduced inserted inductance and the high response from the traces.

4.3 Sensor fusion of the Magnetoresistor and Rogowski coil

To keep the system simple and understandable, combining the sensors should be done analog. Based on papers like [20] and [21] the sensor fusion is supposed to work as shown in Figure 4.7. The magnetoresistor has some sort of band limiting which results in a low-pass behavior (Equation 4.5) with a slope of -20 dB/decade after the limiting frequency of $f_{MR} = \frac{1}{\tau_{MR}}$. This is equivalent to first order low-pass filters with the equivalent time constant $\tau = RC$. The Rogowski coil connects the input current to an output voltage based on Equation 4.7 which can be converted into the frequency domain as demonstrated in Equation 4.8. The Rogowski coil only needs a current-proportional signal, when the magnetoresistor's cutoff frequency is reached, because the magnetoresistor covers the lower frequency range. To get a proportional signal from the Rogowski coil, the coil's output has to be integrated which is done in Equation 4.9. If the magnetoresistor's cutoff frequency is too high, a low-pass filter can be added (Equation 4.6). This additional low-pass filter would circumvent the magnetoresistor's variation in cutoff frequency. The Rogowski coil needs a cutoff filter (Equation 4.10) to limit the bandwidth to a value the operational amplifiers can handle. Therefore, a second order passive low-pass filter was chosen. All sensors and filters are graphically combined in Figure 4.7.

$$H_{MR}(s) = \frac{K_{MR}}{1 + s\tau_{MR}} \quad (4.5)$$

$$H_{lpMR}(s) = \frac{1}{1 + sR_{lp}C_{lp}} \quad (4.6)$$

$$u_{rog}(t) = M_{rog} \frac{d}{dt} i_{current}(t) \quad (4.7)$$

$$H_{rog}(s) = sM_{rog} \quad (4.8)$$

$$H_{int}(s) = \frac{1}{1 + s\tau_{int}} \quad (4.9)$$

$$H_{cutoff}(s) = \frac{1}{1 + sRC + s^2LC} \quad (4.10)$$

For simplicity, the explanation of the sensor fusion will not cover the Rogowski coil cutoff filter. It will also only take the lower limiting frequency of the magnetoresistor signal conditioning. The omission of one low-pass filter for the magnetoresistor will need some precautions. The closer the both filter cut-off frequencies are together, the less correct the resulting transfer function will be. To start the proof for the fusion, some gains for both sensors need to be stated (Equations (4.11) and (4.12)). To calculate the conditions, where a fusion is valid, only a frequency independent gain should be the result of the simple addition in Equation 4.13. After inserting Equations (4.5), (4.8), (4.9), (4.11) and (4.12) into Equation 4.13, equating the coefficients was done in Equation 4.16. For s^0 (Equation 4.17) and s^1 (Equation 4.18) the coefficient equating gave easy results, for s^2 some assumptions need to be made (Equation 4.19). The result from Equation 4.19 states, that the integrator time constant and magnetoresistor time constant needs to be exact the same². Otherwise the s^2 terms will effect the resulting transfer

²During all operational condition ranges like temperature, currents, humidity, age, etc.

function in Equation 4.20. The resulting gain values for the sensor fusion were calculated using Equation 4.21 and Equation 4.22. The gain K_s can be chosen freely for the overall system gain.

$$K_{MR(OPV)} = \frac{K_s K_1}{K_{MR}} \quad (4.11)$$

$$K_{rog(OPV)} = \frac{K_s K_2}{M_{rog}} \quad (4.12)$$

$$H_{fusion}(s) = K_{MR(OPV)} H_{MR}(s) + K_{rog(OPV)} H_{rog}(s) H_{int}(s) \quad (4.13)$$

$$H_{fusion}(s) = \frac{K_s K_1}{K_{MR}} \frac{K_{MR}}{1 + s\tau_{MR}} + \frac{K_s K_2}{M_{rog}} s M_{rog} \frac{1}{1 + s\tau_{int}} \quad (4.14)$$

$$= K_s \left(\frac{K_1}{1 + s\tau_{MR}} + \frac{K_2}{1 + s\tau_{int}} \right) \quad (4.15)$$

$$= K_s \left(\frac{K_1 + s(K_1\tau_{int} + K_2) + s^2 K_2 \tau_{MR}}{1 + s(\tau_{MR} + \tau_{int}) + s^2 \tau_{MR} \tau_{int}} \right) \quad (4.16)$$

$$K_1 = 1 \quad (4.17)$$

$$K_2 = \tau_{MR} \quad (4.18)$$

$$\tau_{MR} = \tau_{int} \quad (4.19)$$

$$H_{fusion}(s) = K_s \quad (4.20)$$

$$K_{MR(OPV)} = \frac{K_s}{K_{MR}} \quad (4.21)$$

$$K_{rog(OPV)} = \frac{K_s \tau_{MR}}{M_{rog}} \quad (4.22)$$

$$(4.23)$$

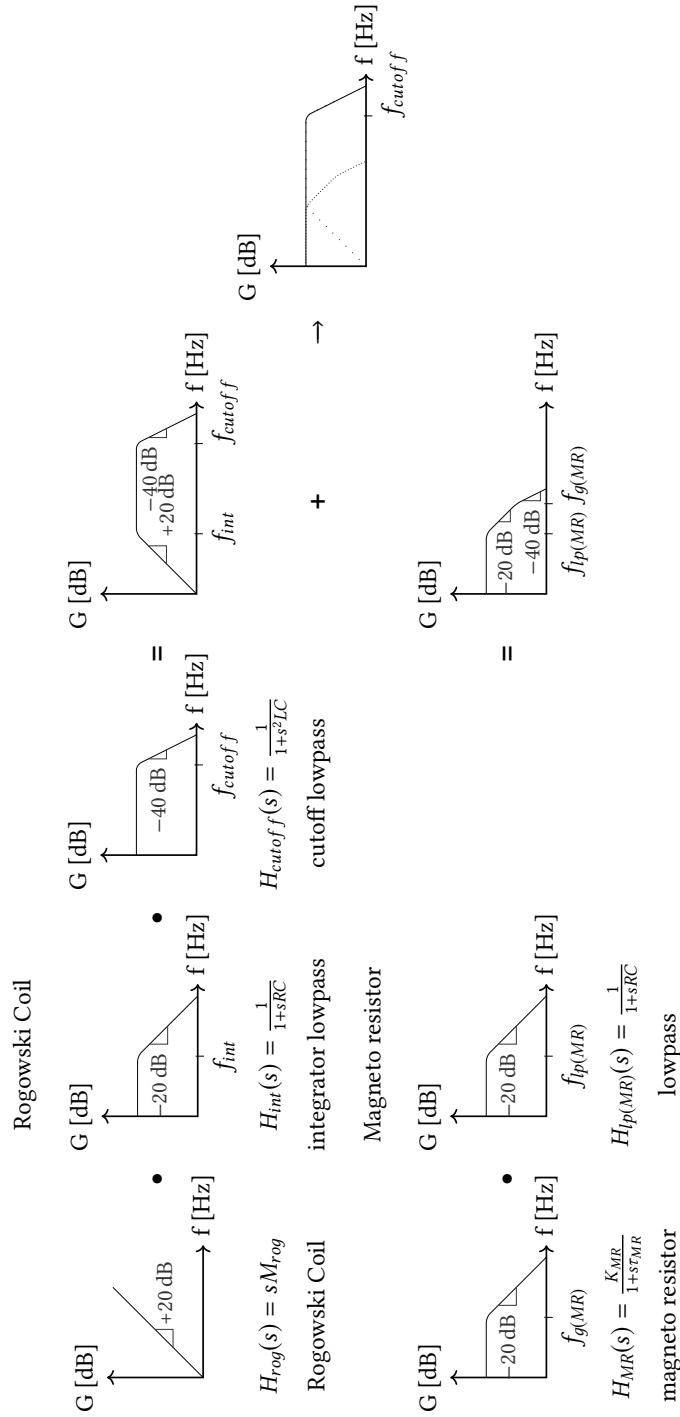


Figure 4.7: Sensor fusion concept: Magnitude plot in frequency domain. The frequency axis is logarithmic, the magnitude axis linear in [dB]. The figure describes graphically how the sensor fusion will work in the frequency domain. Basically the Rogowski coil measures the high-frequency parts and the magnetoresistor the low-frequency parts which can be added together with ideally a constant transfer-function. The triangles shown in the transfer functions describes their slope per decade.

4.4 Sensor Interface

One important part of a sensor is its interface to the external signal processing electronics and power supply. This is the point where the signal conditioning and voltage supply is not under the control of the sensor board any more. Therefore the datasheet of such a sensor has to specify the maximum output load, power supply range, etc.

To maximize the noise rejection between the sensor and the signal processing electronics (e.g. an ADC), one design concept is a fully differential output. This feature gives the following advantages:

- Common-mode noise reduction
- Common-mode field suppression³
- Doubled Signal⁴
- Less offset issues
- High-frequency ADCs support differential signaling but require a common-mode voltage (V_{OCM})⁵
- No need for a $\frac{V_{CC}}{2}$ or negative supply for a subtraction amplifier

Another weak point is the power supply:

One way to reduce the impact is to embed a dedicated voltage regulator onto the sensors PCB. The other way is an appropriate filtering. Both possibilities do have their own benefits and drawbacks. For this thesis, no internal power supply should be used. Since the Rogowski coil's signal is independent from the power supply, varying the power supply voltage will change the gain for the magnetoresistor and not for the Rogowski coil and therefore change the resulting transfer function.

³Due to the sensors are partly already differential.

⁴Due to two signals with opposite sensing directions.

⁵Fully differential analog to digital converter with V_{OCM}/V_{CM} output e.g. Analog AD9634.

5 Magnetic Field Simulation

5.1 Introduction

In the last chapters, the general idea of which sensors should be used and how they should be placed were explained. In this chapter, a magnetic field simulation was designed. It was later used for a placement optimization.

5.2 Tools

For magnetic field simulations, a few tools were considered and evaluated. Besides the functionality to simulate magnetic fields, the main properties, which were important for the final selection were:

- Availability
- Remote controllability
- Operating System Support for Linux

The remote controllability was necessary for generating repeatable results and varying different parameters. The evaluation started with *Keysight Advanced Design System*, which is a RF design system. This software did not fit the needs, because it only simulate the coil as an inductive component and would not take care of the geometry in relation to some traces. The next software was *COMSOL Multiphysics* which solves different physics related problem formulation using finite element analysis. It requires *MathWorks MATLAB* for remote controlling. *Ansys Maxwell* was also considered, but failed while installing on a Linux operating system. This short and non-exhaustive evaluation led to the final use of *COMSOL Multiphysics*. It was the first software that was able to simulate the relevant models during the test period.

5.3 Simulation details

The first idea for optimizing the placement was to load a geometry based on [section 3.2](#) into *COMSOL Multiphysics* and varying the parameter of the coil geometry and current trace geometry. The aim was to optimize the output amplitude and linearity of the coil's output. Therefore a model was implemented in *COMSOL Multiphysics*. The model is shown in [Figure 5.1](#). Due to the very high simulation effort in the order of hours for the three dimensional (3D) simulation, optimizing was not possible without very enhanced optimization algorithms. There were as well too much parameters to optimize. A second problem which occurred during all simulation runs was the abandonment because the simulation did not converge. With a high

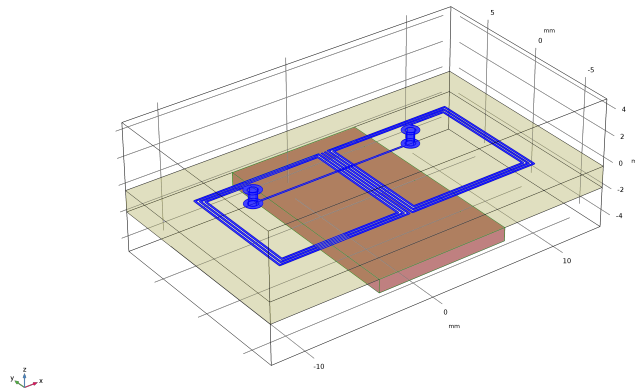


Figure 5.1: 3D simulation volume in *COMSOL Multiphysics* with a current trace (brown) below a pcb (yellow) where a differential Rogowski coil (blue) is embedded. This 3D simulation model was the first design made for this thesis with only a single trace at this time.

probability the problem occurred because of the thickness difference between the different material layers were too high. The wire of the coil has a thickness of $35\ \mu\text{m}$, the circuit board has one of $1.6\ \text{mm}$ and the air volume around was a sphere with a diameter of $20\ \text{mm}$. The thickness variation were close to 10^3 . This is the limit which *COMSOL Multiphysics* proposes as the maximum difference of layer thickness in one dimension. Another problem were these many pieces of $0.127\ \text{mm}$ wide coil trace segments which led to a fine mesh. This mesh was way too big for solving in a useful amount of time.

Since this three dimensional approach was a deadlock, a possible approach was to remove the coil and replacing the inner area of the coils with an integration zone. The resulting \vec{B} -field in this zone would then be integrated according to the *Ampère's circuital law* explained in [Equation 3.2](#).

To simplify this approach even more, the dimension could be reduced by one. To get the same result as with the three dimensional model, some calculations were done. Of course reducing the dimensions will involve an information loss. The trace does not have the correct length anymore and will be considered as infinitesimal long. The necessary calculations are outlined in the following section. One benefit of this two dimensional approach is a more simple optimization of the magnetoresistors placement which only needs the exported \vec{B} -field from the same simulation as for the Rogowski coil.

5.4 Effort reduction

5.4.1 Assumptions for calculations

For the first calculations, the trace will be assumed to be an infinite long wire along the z-axis with an infinitesimal thin circular diameter. For simplicity, the trace is centered at the origin of the coordinate system.

5.4.2 Proof

Based on the *Faraday law of induction* (Equation 5.1) with the surface S and the *Gauß law for magnetism* (Equation 5.2), the induction voltage (U_{ind}) of a coil is proportional to the magnetic flux (Φ_B) (Equation 5.3). ∂S can be understood as a line integral N times around \vec{E} like an N turn coil. The B in Φ_B stands for the magnetic flux density \vec{B} . Using this knowledge it is possible to limit the calculation focus from $I_{trace} \rightarrow U_{ind}$ to $I_{trace} \rightarrow \Phi_B$. $\Phi_B \rightarrow U_{ind}$ is the coils transfer function which will be discussed in a following chapter.

$$\oint_{\partial S} \vec{E} \, d\vec{l} = - \iint_S \frac{\partial \vec{B}}{\partial t} \, d\vec{S} \quad (5.1)$$

$$\Phi_B = \iint_S \vec{B} \, d\vec{S} \quad (5.2)$$

$$U_{ind} = \oint_{\partial S} \vec{E} \, d\vec{l}$$

$$U_{ind} = -N \frac{\partial \Phi_B}{\partial t} \quad (5.3)$$

The magnetic flux Φ_B can be calculated as a line integral using the *Kelvin-Stokes theorem* (Equation 5.4) and the formula for the magnetic vector potential (Equation 5.5). *Kelvin-Stokes theorem* converts the surface integral of the magnetic flux density \vec{B} to a boundary integral of the magnetic vector potential \vec{A} in normal direction.

$$\oint_{\partial S} \mathbf{F} \, d\vec{l} = \iint_S \nabla \times \mathbf{F} \, d\vec{S} \quad (5.4)$$

$$\vec{B} = \nabla \times \vec{A} \quad (5.5)$$

$$\Phi_B = \iint_S (\nabla \times \vec{A}) \, d\vec{S} \quad (5.6)$$

$$= \oint_{\partial S} \vec{A} \, d\vec{l} \quad (5.7)$$

Now coming back to the trace, Equation 5.7 states that only the magnetic vector potential \vec{A} is needed in order to calculate the magnetic flux Φ_B .

The magnetic vector potential can be derived based on the *law of Biot-Savart*. Therefore Equation 5.8 [22, eq. 5.14] can be rewritten to Equation 5.9 [22, eq. 5.16]. When comparing Equation 5.9 with the formula for the magnetic vector potential in Equation 5.10, their same structure can be seen. Hence these formulas lead to the magnetic vector potential in Equation 5.11 [22, eq 5.28]. The $\Psi(x)$ in Equation 5.11 describes the gauge freedom based on the gauge theory. This will allow to shift $\vec{A}(\mathbf{x}) = 0$ to any point in the valid space. Calculating this equation for an infinite long and infinitesimal thin circular wire in z-direction leads in case of the magnetic vector potential \vec{A} in z-direction to Equation 5.12¹. For rotational symmetry, cylindrical coordinates are easier and therefore $x^2 + y^2$ can be replaced with r^2 . The wire is carrying the current only in z-direction, which leads Equation 5.10 to be one dimensional with respect to dz. The magnetic vector potential will be $\vec{A} = (0 \ 0 \ A_z)$. As an explanation: The \vec{B} -field is circulating around the wire and Equation 5.5 states, that \vec{A} must be normal to the \vec{B} -field.

$$\vec{B}(\mathbf{x}) = \frac{\mu}{4\pi} \int J(\mathbf{x}') \times \frac{\mathbf{x} - \mathbf{x}'}{|\mathbf{x} - \mathbf{x}'|^3} d^3\mathbf{x}' \quad (5.8)$$

$$\vec{B}(\mathbf{x}) = \frac{\mu}{4\pi} \nabla \times \int \frac{J(\mathbf{x}')}{|\mathbf{x} - \mathbf{x}'|^3} d^3\mathbf{x}' \quad (5.9)$$

$$\vec{B}(\mathbf{x}) = \nabla \times \vec{A}(\mathbf{x}) \quad (5.10)$$

$$\vec{A}(\mathbf{x}) = \frac{\mu}{4\pi} \int \frac{J(\mathbf{x}')}{|\mathbf{x} - \mathbf{x}'|} d^3\mathbf{x}' + \nabla\Psi(\mathbf{x}) \quad (5.11)$$

$$A_z(x, y) = -\frac{\mu I}{4\pi} \ln\left(\frac{x^2 + y^2}{x_0^2 + y_0^2}\right) \quad (5.12)$$

$$A_z(r) = -\frac{\mu I}{2\pi} \ln\left(\frac{r}{r_0}\right) \quad (5.13)$$

Because of the rotational symmetry of \vec{A} , it only changes with the radius. The variable r_0 is an arbitrary radius, which represents the before explained gauge freedom. It represents the radius where $A_z(r) = 0$.

With the recent calculation, it is possible, to calculate the magnetic flux Φ_B from Equation 5.2 with \vec{B}_x or using Equation 5.7 with A_z . In Figure 5.2 the surface area of the magnetic flux is depicted as blue hatching. The boundary of this area is marked red and represents the line integral with arrows for the integration direction based on the *Kelvin-Stokes theorem*. The literals $\{a, b, c, d\}$ will be used to show which part of the integral is calculated in the following formulas.

The line integral in Equation 5.14 can be separated into straight line integrals. In the next step they can all be calculated separately. After a few steps, it can be seen, that the integral parts perpendicular to the current trace cancel themselves out. The parallel parts show a linear dependency with the length of the integration. When solving Equation 5.15, the result can be seen in Equation 5.21. In this equation, the magnetic vector potential can be replaced with Equation 5.13 for an infinitesimal thin and infinite long circular current-carrying wire which results in Equation 5.22.

¹The derivation was calculated in [23, chap 5.2.1, eq 5.27].

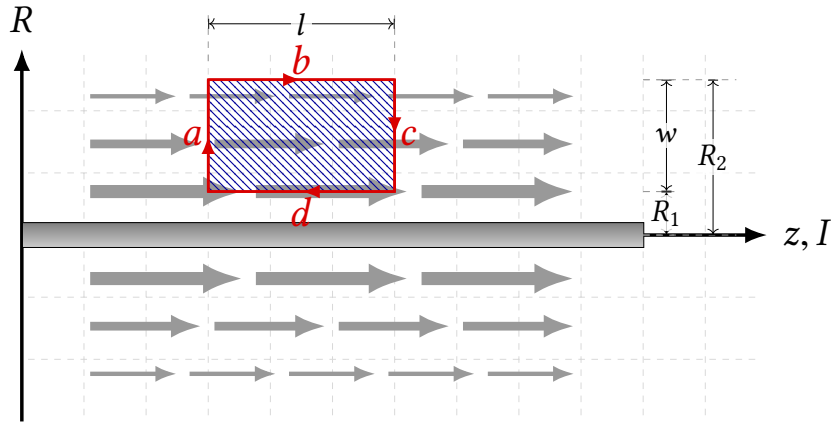


Figure 5.2: The plot describes the connection between the coil area (blue hatched) with a current-carrying infinitesimal thin, infinite long wire. The hatched area represents the Rogowski coils inner diameter. The thickness of the arrows indicates the magnitude of \mathbf{A}_z . There are two corresponding calculation methods: The magnetic flux Φ_B can be calculated using Equation 5.2 and applying a surface integration to the magnetic flux density \mathbf{B}_x . As an alternative the magnetic flux can be calculated using Equation 5.7 and applying a closed curve integration to the magnetic vector potential \mathbf{A}_z .

$$\Phi_B = \oint_{\partial S} \mathbf{A}_z \, d\vec{s} \quad (5.14)$$

$$= \sum_{i=\{a,b,c,d\}} \Phi(i) \quad (5.15)$$

$$\Phi(a) = \int_{r_1}^{r_2} \mathbf{A}_z(s) \, d\vec{s} \quad (5.16)$$

$$\begin{aligned} \Phi(b) &= \int_l^0 \mathbf{A}_z(r_2) \, d\vec{s} \\ &= - \int_0^l \mathbf{A}_z(r_2) \, d\vec{s} \\ &= -\mathbf{A}_z(r_2) \cdot l \end{aligned} \quad (5.17)$$

$$\Phi(c) = \int_{r_2}^{r_1} \mathbf{A}_z(s) \, d\vec{s}$$

$$\begin{aligned}
&= - \oint_{r_1}^{r_2} \mathbf{A}_z(s) \, d\vec{s} \\
&= -\Phi(a)
\end{aligned} \tag{5.18}$$

$$\begin{aligned}
\Phi(d) &= \oint_0^l \mathbf{A}_z(r_1) \, d\vec{s} \\
&= \mathbf{A}_z(r_1) \cdot l
\end{aligned} \tag{5.19}$$

$$\Phi_B = \Phi(a) + (-\mathbf{A}_z(r_2) \cdot l) + (-\Phi(a)) + \mathbf{A}_z(r_1) \cdot l \tag{5.20}$$

$$\Phi_B = [\mathbf{A}_z(r_1) - \mathbf{A}_z(r_2)] \cdot l \tag{5.21}$$

$$\Phi_B = -\frac{\mu I}{2\pi} l \ln\left(\frac{r_1}{r_2}\right) \tag{5.22}$$

5.4.3 Conclusion

Equation 5.21 implies that for the calculation of the magnetic flux Φ_B only the vector potential \mathbf{A}_z at point r_1 and r_2 and the length l of the area are necessary. This insight allows simulating the magnetic vector potential from a two dimensional cross-section of the trace – coil structure and being able to calculate the magnetic flux with some postprocessing. An additional benefit of this proof is to receive one degree of freedom with the length l of the flux surface.

When simulating the magnetic vector potential \mathbf{A}_z of the real trace, the constraint with an infinitesimal thin wire can be dropped. The two dimensional simulation still assumes an infinite long wire in z -direction.

5.5 Introduction to Magnetoresistor placement

The magnetoresistors have one or more sensitive axes according to their respective data sheet. For current measurement only one sensing axis is necessary. The trace has to maintain a distance to the sensor to withstand the voltage difference between sensor electronics and the current trace's voltage for galvanic isolation. Therefore the trace will be on the one side of the PCB and the sensor on the other side or inside the PCB. This reduces the degrees of freedom for placing the sensor to one. A plot of the magnetic flux density in x -direction (\mathbf{B}_x) from a circular trace as shown in Figure 4.1b will give a first assumption of how the magnetoresistor placement can be done. Figure 4.3d shows, that the left side has negative \mathbf{B}_x values and the right side has positive values. This allows a differential magnetoresistor measurement with two sensors. From the datasheet, the precise location of the magnetoresistor sensor can be determined and then the position at this height, be optimized.

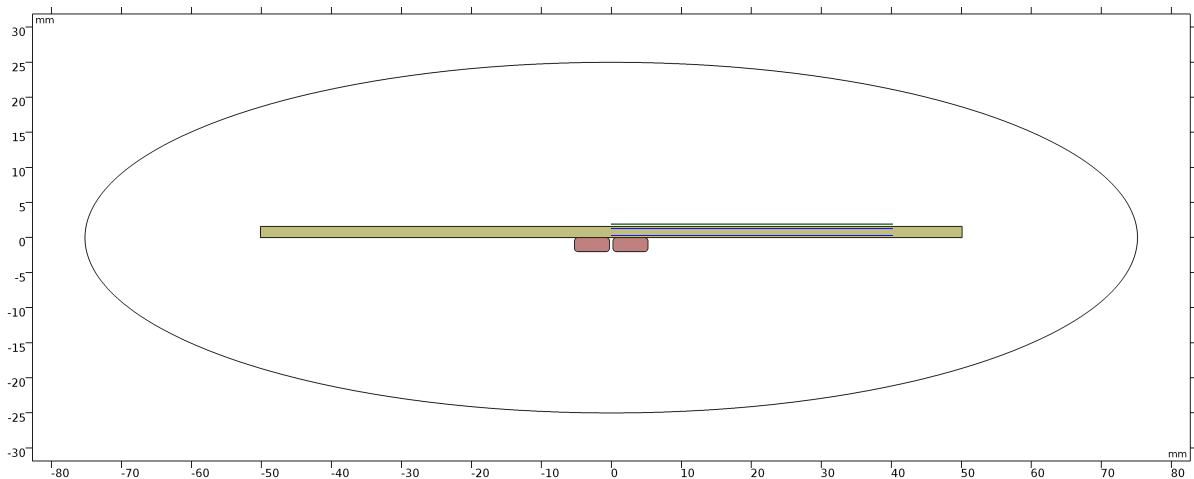


Figure 5.3: The simulation model for magnetic field simulation. The figure shows a current trace (brown) underneath a circuit board (yellow-green) with embedded coils (blue). The traces are 5 mm wide and 2 mm high and keep a distance of 0.5 mm.

5.6 Postprocessing

5.6.1 Principle

Based on the theoretical analysis in [subsection 4.2.3](#) and [section 5.4](#) a two dimensional simulation model was created. An exemplary model is shown in [Figure 5.3](#). The current-carrying traces are displayed as brown bars underneath the yellow-green colored circuit board. Inside the circuit board are two lines on the right side which represent the inner area of the coils. The line above the circuit board represents the line for the magnetoresistor placement. These lines are divided into several pieces to force the simulation to solve all equation at these points. The ellipse around the model is the air volume which functions also as the boundary for all magnetic fields. The shape has to be matched with the expected contour lines of the magnetic fields. Otherwise the simulation error will increase. The magnetic vector potential \vec{B} should be an ellipse in the far field for a single current-carrying trace. For simplicity, the ellipse was kept also for the dual trace simulation. The difference of the magnetic field between the right and the left side is only the algebraic sign. This allows to simulate only one side which was not realized. The simulation shows the expected results in [Figure 5.4](#) for the magnetic vector potential A_z and the magnetic flux density B_x . All simulations are auto generated based on a configuration read by a script that remote controls the simulation tool. The optimal placement can be reached by optimizing [Equation 5.21](#). Because the Length l of the coil does not change the optimal result, it can be set to 1 m.

5.6.2 Workflow

One important characteristic of scientific work should be the repeatability of any task. In this thesis, repeatability has been ensured by running the simulations and postprocessing with almost no manual steps, but only by vary the configuration file. Therefore, two main scripts

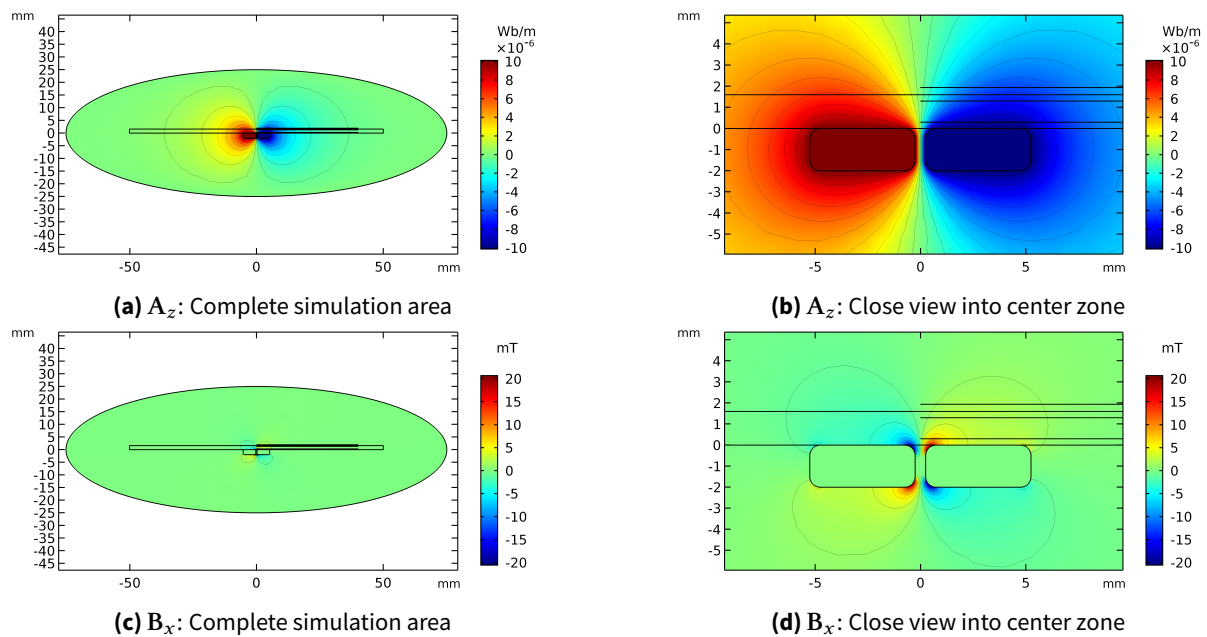


Figure 5.4: Screenshots from a *COMSOL Multiphysics* simulation. (a) and (b) are showing the magnetic vector potential (A_z) and (c) and (d) are showing the magnetic flux density (B_x). For all plots at 100 A and 100 MHz with a inter trace distance of 0.5 mm.

were written in *Python3*² which are extensively using *NumPy*³. The first one generates the geometric model and the simulation model and runs the simulation. The second script does all the postprocessing for the coil and magnetoresistor placement and plots the result. The working principle and interaction between these scripts is depicted in [Figure 5.5](#).

The first script exports the vector potential A_z and the magnetic flux density B_x at the previously described lines in the geometry from the simulation tool into *csv*⁴-files which will then be imported by the second script for further processing. The postprocessing script evaluates the data using an objective function. Afterwards the optimal parameter trajectory can be exported and compared to other trajectories obtained from other simulations.

5.6.3 Objective function

An objective function⁵ is a constrained or unconstrained cost function for optimizing a set of parameters. The goal of an optimization is to get an optimal parameter set p_{opt} which leads to minimal (or maximal) cost.

The data from the simulation tool is a discrete, complex transfer function for the magnetic vector

²<https://www.python.org>

³<https://www.numpy.org>

⁴comma separated value

⁵An objective function or design function contains out of two parts: “[The] objectives and constraints. Objectives represent goals we wish to maximize or minimize. Constraints represent limits we must stay within, if inequality constraints, or, in the case of equality constraints, target values we must satisfy.” [24, chap. 1.1]

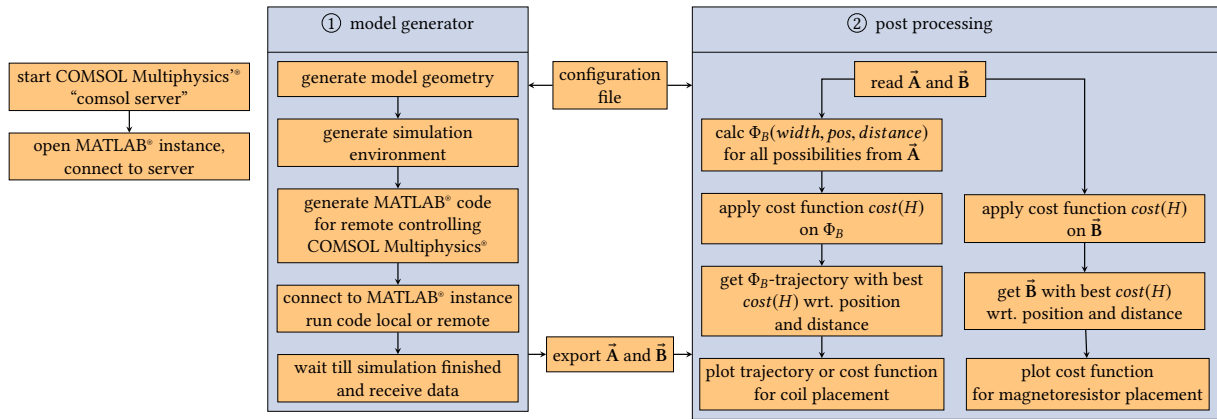


Figure 5.5: Software flowchart for running magnetic field simulations and the subsequently done post-processing for the placement simulation of magnetoresistors and planar Rogowski coils. The scripts are written in *Python3/NumPy*. For running simulations, a *COMSOL Multiphysics* server and a *MathWorks MATLAB* instance is necessary.

potential A_z and magnetic flux density B_x at distinct points for a frequency range between 1 Hz and 1 GHz. For the optimal placement of the coil, the results from Equation 5.21 are used as objective function $H(\omega)$. The coil's parameter set p consists of an integration width and a starting position of the integration. For the magnetoresistor, The magnetic flux density B_x can directly used as objective function $H(\omega)$. The magnetoresistor's parameter set p consists only on a one dimensional position, because the height of the placement is fixed by the circuit board.

Usually the cost function of a transfer function increases/decreases the larger the difference between the actual transfer function and the desired transfer function gets. In this case, the system should be a minimal phase system with all-pass characteristics and a maximum gain. This leads to an optimal phase $\psi(\omega_{opt}) \rightarrow 0$ and an optimal magnitude $\frac{A(\omega)}{A} = 1 \quad \forall \omega$.

For simplicity and because the cost function needs to be evaluated for every possible parameter set p , the phase and magnitude differences are gathered rather simply. Using the transfer function (Equation 5.23), the phase is calculated in Equation 5.24 based on [25, def 4.19]. As the corresponding cost function, the L_1 -norm of the phase $\psi(\omega)$ is used (Equation 5.25). This gives a range for the phase cost function from 0 (very good) to ∞ (very bad).

The magnitude is calculated in Equation 5.26 based on [25, def 4.17]. The corresponding cost function could be Equation 5.28. \bar{A} represents the arithmetic mean of $A(\omega)$. Equation 5.28 should reach zero for its optimum.

The cost function should be maximized with respect to the phase, all-pass characteristics and gain. The used realization is shown in Equation 5.29. The coefficients $0 > \alpha \geq 1$ and $0 > \beta \geq 1$ are used to weight the phase and magnitude quality. The optimal parameter set p_{opt} leads to a maximal cost-function.

$$H(\omega) = Re\{H(\omega)\} + j Im\{H(\omega)\} \quad (5.23)$$

$$\psi(\omega) = \arg(H(j\omega)) = \arctan2\left(\frac{\text{Im}\{H(\omega)\}}{\text{Re}\{H(\omega)\}}\right) \quad (5.24)$$

$$\text{cost}(\psi) = \|\psi(\omega) - \psi(0)\|_1 = \sum_i |\psi(i) - \psi(0)| \quad (5.25)$$

$$A(\omega) = \|H(\omega)\|_2 = \sqrt{(\text{Re}\{H(\omega)\})^2 + (\text{Im}\{H(\omega)\})^2} \quad (5.26)$$

$$\bar{A} = \frac{1}{n} \sum_{i=1}^n A(i) \quad (5.27)$$

$$\text{cost}(A) = \left\| \frac{A(\omega)}{\bar{A}} - 1 \right\|_1 \quad (5.28)$$

$$\text{cost}(H) = \left(\frac{\alpha}{\text{cost}(\psi)} + \frac{\beta}{\text{cost}(A)} \right) \bar{A} \quad (5.29)$$

5.6.4 Explanation

Using the insights from the last subsection and combining it with the exported data from the simulation leads to [Figure 5.7](#) for the coil placement and [Figure 5.8](#) for the magnetoresistor placement. Each point in these plots represents the objective function for a placement simulation with a specific parameter set $p(\text{pos}, \text{width})$. The simulation results are based on the model depicted in [Figure 5.3](#).

The origin of the x-axis in the plot describes the start of the underlying current trace to the right. This shift from the coils origin to the start of the trace ($\frac{\text{trace gap}}{2}$) has to be done in order to be able to compare different trace gap sizes. The left limit describes the origin of the coil or the middle of the trace gap. The x-axis describes the left starting position of the coil's inner white space (left anchor). This is necessary because the calculations' aim is to integrate the field collected between the coil parts running in parallel to the trace. Therefore the calculation does not respect the number of turns or other properties of the coils trace properties for example the trace width. The width of the coil plotted on the y-axis is only the length of the integration line. The overall width of the coil can be calculated by adding the trace space and the trace width multiplied by twice the number of turns plus the width shown at the y-axis. The terminology is described using a sketch in [Figure 5.6](#).

In [Figure 5.7](#), higher values or darker colors represent a better parameter set p consisting of positioning and width. The triangular shape results because a small line can be shifted through one of these coil-representing lines in [Figure 5.3](#) several times. A long coil can only be shifted a few times. A coil with the width of the complete line cannot be shifted at all. The plot is only valid for a fixed distance on the y-axis to the trace and only for one trace geometry.

The plots (a), (b), (c) in [Figures 5.7](#) and [5.8](#) each show one part of the objective function to understand the composition of the objective function. Plot (d) represent the final plot of the objective function ([Equation 5.29](#)). The plots in [Figure 5.9](#) show the real transfer function for both the Rogowski coil and magnetoresistor positioning. The overshoot is could be due to bad gain coefficients α and β at the cost function in [Equation 5.29](#). Another possibility could be some simulation problem, because almost all transfer functions show this behavior. But it

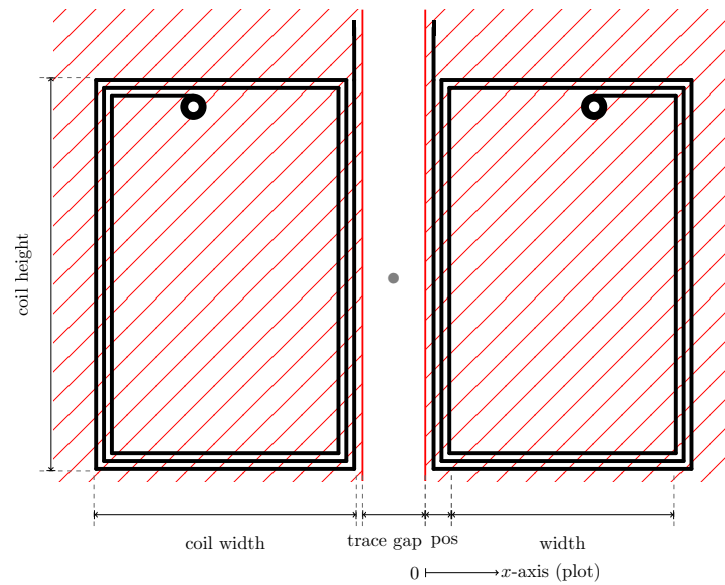


Figure 5.6: The real coil layout with 0.15 mm thick traces and the current trace as red hatches below the left and right side. The coils overall dimensions are described with “coil width” and “coil height”. The “pos” (short for positioning) represents the x-axis of the optimization plots and the “width” of the corresponding y-axis. The origin of the trace plot is $\frac{\text{“trace gap”}}{2}$. The gray dot marks the origin of the Rogowski coils in this figure.

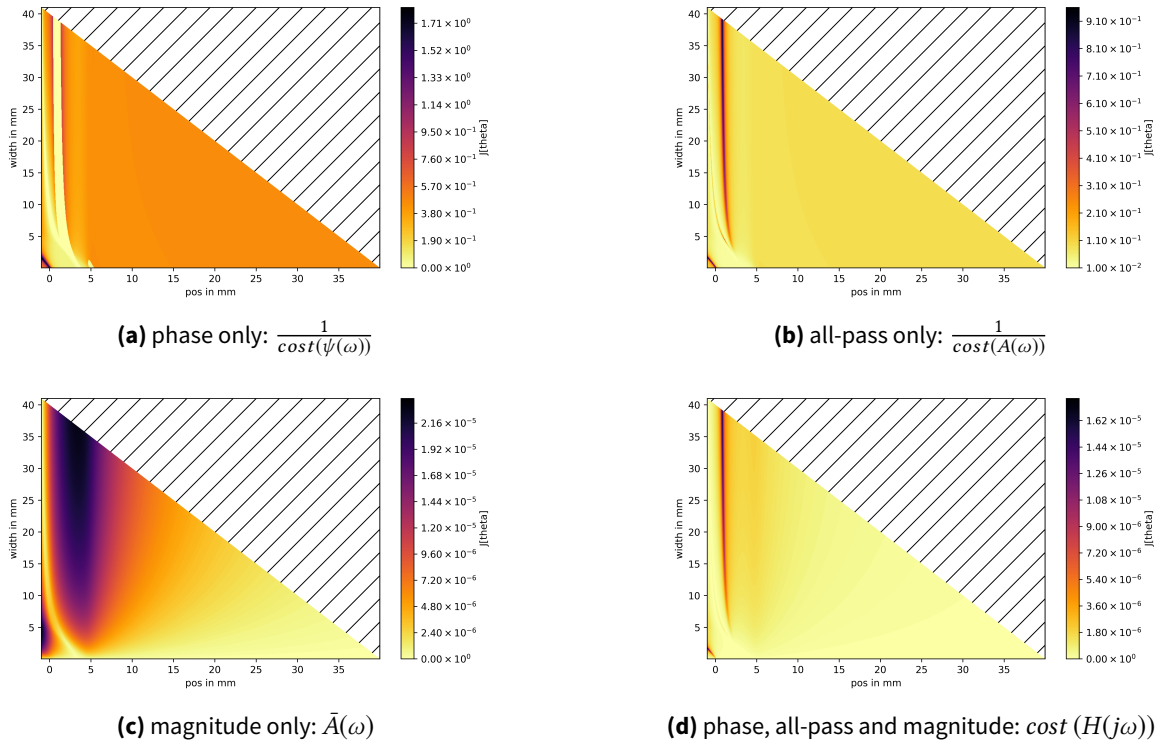


Figure 5.7: Different parts of the objective functions for coil placement using the U-shaped trace with 5 mm trace width, 2 mm trace thickness, 2 mm trace distance and 0.3 mm distance to the trace. The plots (a)-(c) describe parts of the objective function which are combined in the plot (d). IN plot (d) a clear trajectory can be recognized. With this result, the width and length of the coil can be freely chosen and only the optimal positioning will vary slightly, when a minimum width of 5 mm is chosen.

should be remembered, that this approach only tries to achieves the best for a non-ideal planar Rogowski coils. Using a traditional Rogowski coil would circumvent this problem but would however not meet the requirement stated in [section 1.2](#).

5.6.5 Trajectory extraction

The trajectory extraction has only been done for the single trace coil assembly (compare [Figure 4.4](#)), because when starting to use the U-shaped trace, the trace parameters were already fixed and the only choice left posed the y-axis distance between the two inner layers of the trace. Furthermore, the lower inner layer were chosen because of the higher gain.

The results from the first step in [Figure 5.7d](#) of the coil placement show a clear trajectory, of the optimum. This trajectory can be extracted by searching in every width the maximum. Plotting multiple trajectories leads to a plot like [Figure 5.10](#). Each line shape represents a different distance and each color another trace shape. The current and trace cross-section is still fixed. With increasing distance from the trace, the cross-section moves towards the corner of the trace. The wider a trace, the less is the influence of the cross-section on the distance.

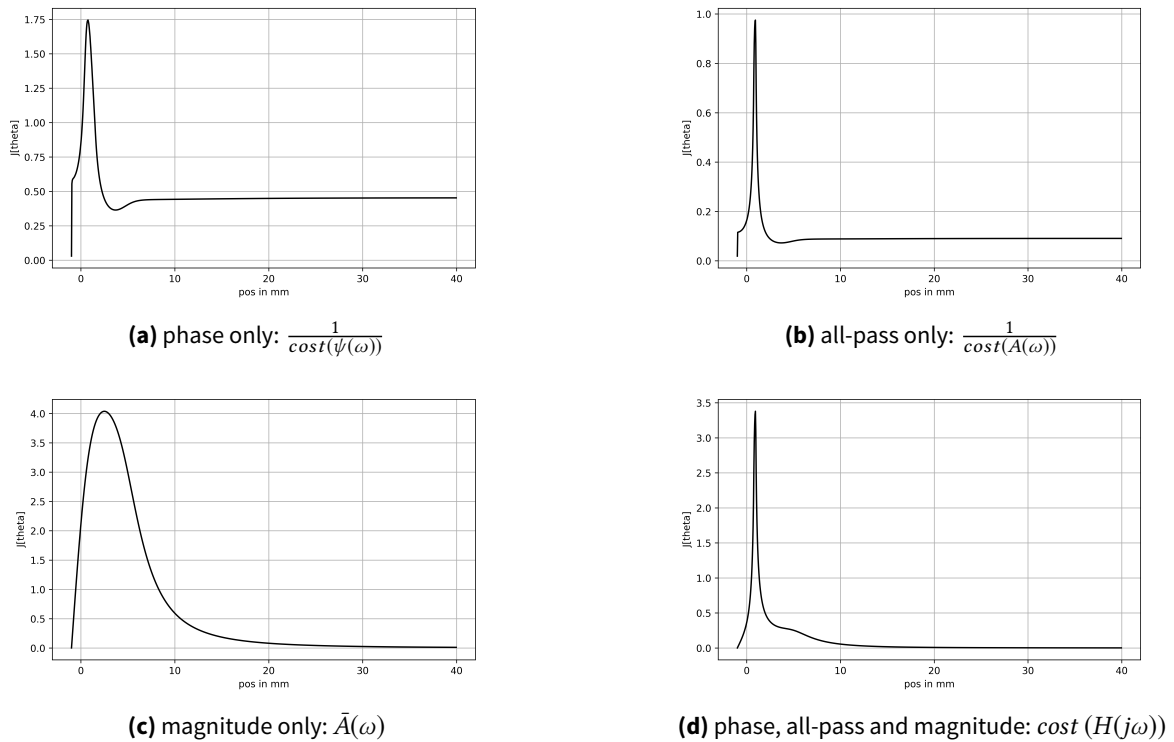


Figure 5.8: Different parts of the objective functions for magnetoresistor placement using the U-shaped trace with 5 mm trace width, 2 mm trace thickness, 2 mm trace distance and 1.94 mm distance to the trace. The plots (a)-(c) describe parts of the objective function which are combined in the plot (d). For the chosen trace shape and distance of the sensor, an optimal positioning can be viewed directly from plot (d).

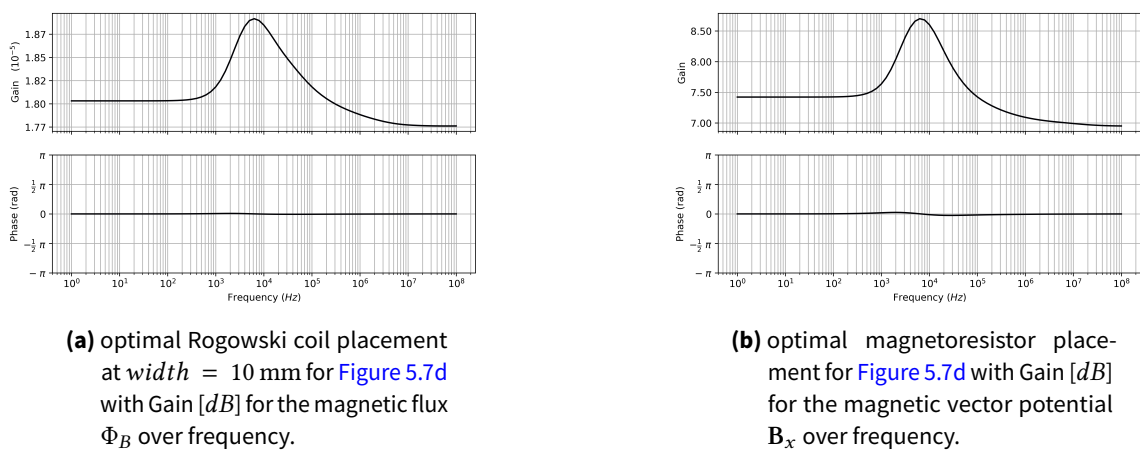


Figure 5.9: Normalized Bode plots for the sensors respective optimal point. The Gain [dB] shows some overshoot at 5 kHz. For this overshoot there are different possible explanations as simulation errors, model errors, etc. This behavior was later not recognized from the coils output.

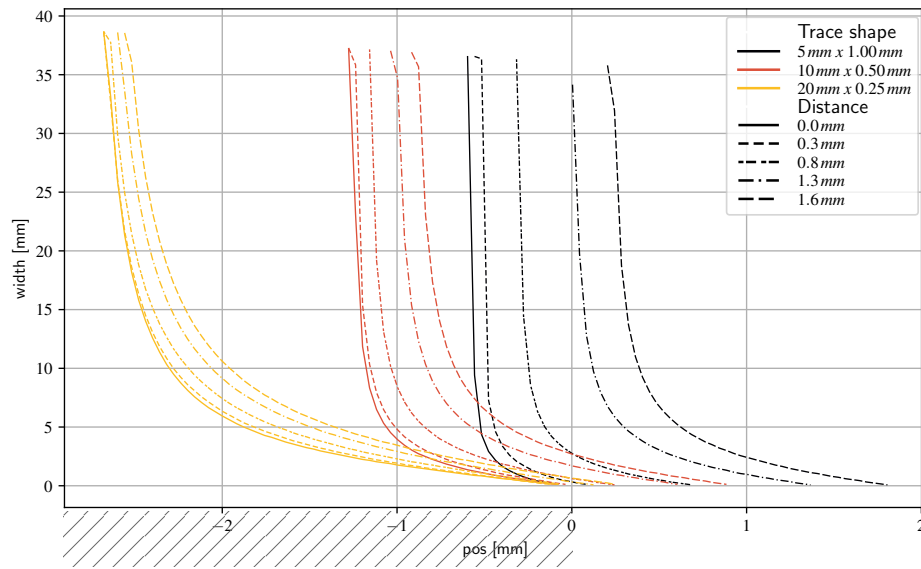


Figure 5.10: Optimal trajectories for different coil distances and trace shapes for single current trace assembly. The right part of the trace cross-section is depicted as an hatched block below the x-axis. The plot is based on a setup shown in [Figure 4.4](#).

5.6.6 Conclusion

To determine how a coil should be placed, it is a good start to study, which restrictions apply. At first glance it is necessary to determine the cross-section of the trace for the targeted current. The distance between coil and trace is limited by what layer stack a circuit board manufacturer provides and the maximum output voltage the sensor is targeting. The length of the coil area is freely choosable but should not reach the length of the current trace because of the magnetic flux Φ_B will not increase linear with the length because the current trace is not a infinite long wire. The cross-sectional width is also restricted by the available space on the circuit board and the minimal sum of trace width and trace spacing.

If all conditions are set, the optimal starting point for the cross-section can be calculated by the self written pre- and postprocessing script. With the resulting parameter set a footprint for the coils can be generated. The magnetoresistors are way easier to model. Only the magnetic flux density in x-direction at all points has to be evaluated. The magnetoresistor's optimal placement can be clearly viewed in [Figure 5.8d](#). The narrow optimum leads to the necessity of a precise placement which was ensured by marking the center position of the magnetoresistors in the coil's footprint.

5.7 Result

In the last section, the optimal placement for the Rogowski coil and the magnetoresistor has been simulated and calculated. The width of the coil was determined to 10 mm as a good

type	distance to trace	position
Rogowski coil	0.3 mm(Layer 3)	1.34 mm
Rogowski coil	1.6 mm(Layer 1)	1.45 mm
magnetoresistor	1.94 mm	0.929 mm

Table 5.1: Final simulation results for the sensors with a given integration width of 10 mm for the coil. The distance to trace describes the geometric distance between sensor and trace. “width” and “height” are sketched in [Figure 5.6](#).

starting point for a useful circuit board size. The optimal positioning can be read off [Figures 5.7](#) and [5.8](#). [Table 5.1](#) lists all relevant values for the chosen optimal parameter set $p_{opt}(chosen)$ for both sensors.

6 Sensor Structure

6.1 Introduction

In the last few chapters, there were no considerations on how both sensing elements from [chapter 4](#) could be merged to one wideband sensor. In this chapter a structure how the sensors could be merged will be described.

6.2 Rogowski coil equivalent circuit

Basically, the Rogowski coil acts as a transformer which converts a current into a voltage. This theory was already described in [section 3.2](#) in [Equation 3.5](#). The coupling M between both coils cannot be calculated but has to be determined because the planar coil does not cover the whole perimeter of the current trace. Therefore a numerical calculation was used. The theory is described in the following paragraphs.

The current trace and the coil can be described using a generic passive linear two-port network model ([Figure 6.1](#)) which can be expressed using an impedance matrix shown in [Equation 6.1](#). The impedance Z is defined in [Equation 6.2](#) to [6.5](#) [[26](#), chap. 4.2].

$$\begin{bmatrix} U_1 \\ U_2 \end{bmatrix} = \begin{bmatrix} Z_{11} & Z_{12} \\ Z_{21} & Z_{22} \end{bmatrix} \cdot \begin{bmatrix} I_1 \\ I_2 \end{bmatrix} \quad (6.1)$$

$$Z_{11} \stackrel{\text{def}}{=} \left. \frac{U_1}{I_1} \right|_{I_2=0} \quad (6.2)$$

$$Z_{12} \stackrel{\text{def}}{=} \left. \frac{U_1}{I_2} \right|_{I_1=0} \quad (6.3)$$

$$Z_{21} \stackrel{\text{def}}{=} \left. \frac{U_2}{I_1} \right|_{I_2=0} \quad (6.4)$$

$$Z_{22} \stackrel{\text{def}}{=} \left. \frac{U_2}{I_2} \right|_{I_1=0} \quad (6.5)$$

The “current trace - Rogowski coil”-system can be described as an equivalent circuit model shown in [Figure 6.2](#). This model can be transformed based on [Equation 6.1](#) and results in [Equation 6.6](#). The components of the equation are the coil resistances $R_i \in 1, 2$, the self inductance $L_i \in 1, 2$, the mutual inductance M and a distributed capacitance C_c on the Rogowski side of the model. As it becomes evident from [Figure 6.2](#), all components are linear and passive. The resulting passive linear two-port is reversible or reciprocal by definition, i.e. $Z_{12} \equiv Z_{21}$. To explain this behavior in [Figure 6.2](#), only the mutual inductance M connects both sides of this

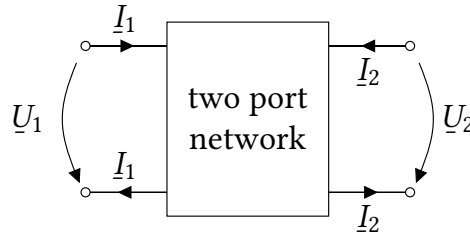


Figure 6.1: Generic two port model

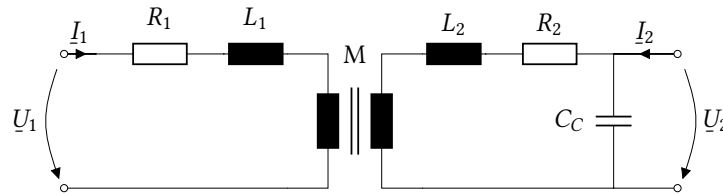


Figure 6.2: Equivalent Circuit model of a transformer or Rogowski coil with a current trace.

model. Since M is linear and has the same value in both directions, the resulting impedance matrix has to be symmetric. The coupling should be almost lossless which forces Z_{12} and Z_{21} to be purely imaginary. In the here chosen definition, \underline{U}_1 and \underline{I}_1 represent the current trace and \underline{U}_2 and \underline{I}_2 represent the Rogowski coil.

$$\begin{bmatrix} \underline{U}_1 \\ \underline{U}_2 \end{bmatrix} = \begin{bmatrix} R_1 + j\omega L_1 & j\omega M \\ j\omega M & R_2 + j\omega L_2 \end{bmatrix} \cdot \begin{bmatrix} \underline{I}_1 \\ \underline{I}_2 \end{bmatrix} \quad (6.6)$$

To fill these definitions with real values, a numerical calculation was performed. Based on the exact geometry used for the real PCB layout, a three-dimensional inductance extraction using *fasthenry*¹[27, 28] has been performed. To validate the results, the required symmetry of the matrix has to be checked ($A = A^T$). Minor unsymmetrical values happen due to the numerical computation and finite accuracy and can be compensated by using the average of Z_{12} and Z_{21} which can be calculated in matrix notation as $A = 0.5(A + A^T)$. Based on Equation 6.6, the self and mutual inductance and the corresponding series resistances can be calculated. From the mutual inductance M and the self inductance's $L_i \in 1, 2$, the coupling can be calculated using Equation 6.7. The distributed capacitance C_c can't be computed with *fasthenry* because it does only calculate inductive and resistive parts of the geometry. A computation using the corresponding program *fastcap* for calculating the parasitic capacitance was not successful.

$$k^2 = \frac{M^2}{L_1 L_2} \quad (6.7)$$

As examples, two results of the numerical computation are displayed in Table 6.1.

¹<https://www.fastfieldsolvers.com/>

	Layer 1	Layer 3
distance [mm]	1.6	0.38
L_1 [nH]	11.16	11.16
L_2 [nH]	521.5	491.3
R_1 [m Ω]	5.233	5.030
R_2 [Ω]	2.110	2.122
M [$\frac{H}{H}$]	4.572e-9	8.732e-9
k [%]	6.05	11.73

Table 6.1: Rogowski coil equivalent circuit parameters for placement on different PCB layers with 0.38 mm (Layer 3) and 1.6 mm (Layer 1) distance to current trace based on [Figure 6.2](#). The most significant changes are within the coupling of trace and coil.

6.3 Design Considerations

6.3.1 Attaching the trace to the sensor board

To attach the current trace to the board, there are several options:

- bonding via epoxy
- soldering to copper islands
- bolting to the circuit board
- holding in place via some plastic snapping parts (distance will be maintained after the sensor with its PCB and trace is soldered into its final board)

The easiest solution for a prototype is to glue the copper trace to the circuit board. This can be done with e.g. epoxy. For mass production, some plastic clip could speed up the production. If using epoxy, a few things have to be noted. In this example *Henkel Loctite M-121HP*[29] will be used. The manufacturer requires an average bond thickness of 0.1 to 0.2 mm. The shear strength of this bond will increase, the thinner the bond is, but raises the risk of incomplete fills. For a galvanic insulation calculation, the bond thickness has also to be considered. The bond thickness also needs to be considered for the coupling between the coil and the current trace. It adds about 25 % to 50 % of distance to the trace.

6.3.2 Galvanic Insulation

One important property of the sensor is the galvanic isolation between the current trace and the sensing electronics. To achieve this, a minimum euclidean distance between the trace and the parts of the coil² have to be ensured. As one of the intended applications in a GaN

²The coil consists out of two Rogowski coils, the connection between the coils and the supply lines. Specially vias needs to be considered in terms of minimum distance.

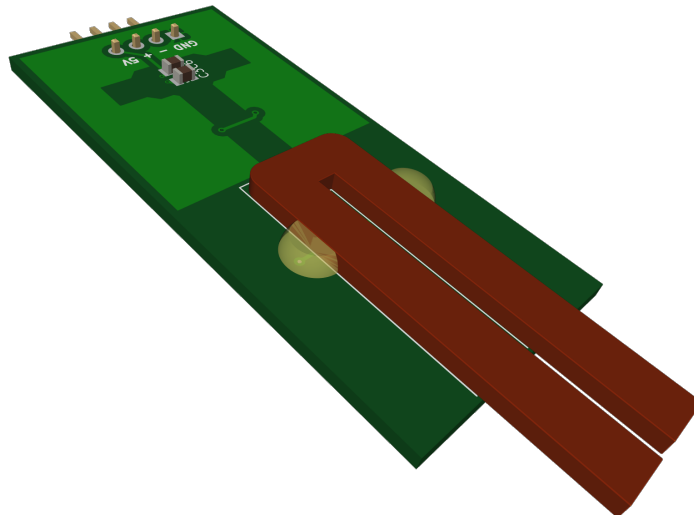


Figure 6.3: Current Trace(red) on top of PCB(green) with epoxy over the vias(opaque)

Converter, voltages of 650 V³ and higher have to be considered. In general a starting point for the required insulation test voltage are other isolating products, such as opto-couplers, or isolating current sensors. Opto-couplers can be divided into two groups⁴: *Optical Isolators* and *Digital Isolators*. The latter refer to magnetic or capacitive coupling. The current sensor's physical functionality is based on magnetic coupling. As established standards *IEC 61010-1*⁵ and *IEC 60950-1*⁶ have to be mentioned in this case. These standards define a test voltage of 4.8 kV for an operational voltage between 354 V and 1414 V for one minute of reinforced insulation tests. The standard circuit board material FR4⁷ has a dielectric strength of $13 \frac{\text{kV}}{\text{mm}}$. Using the formula for the dielectric strength $E = \frac{U}{d}$ results in a minimal distance of 0.385 mm. For the vias, there is another possibility to avoid using expensive burried vias. They can easily be covered with epoxy. For example with the previously mentioned *Henkel Loctite M-121HP*. The dielectric strength according to their datasheet[29] is $25.5 \frac{\text{kV}}{\text{mm}}$. This leads to a minimum euclidean distance in this epoxy of 0.1875 mm. Now the vias can be covered with a 0.2 mm thick layer of epoxy and only need to maintain a distance of 0.2 mm between the via and any point of the copper trace. This is shown in Figure 6.3. If the copper trace is glued down using epoxy the epoxy-via solution can be done in the same working step.

³GaN Transistors from GaN SYSTEMS.

⁴www.analog.com/media/en/technical-documentation/tech-articles/MS-2234.pdf

⁵*IEC 61010-1*: safety standards for products in information technology

⁶*IEC 60950-1*: safety standards for products in measurement equipment

⁷This the today's standard for circuit boards and abbreviates "flame retardant 4"(NEMA, 1968)

6.3.3 Targeted dimensioning

6.3.3.1 Distance

For this thesis, the sensor should be able to handle an nominal current of 100 A. The current trace should be out of tin-plated copper and glued down using *Henkel Loctite M-121HP* epoxy. Based on the geometrical aspects in subsection 4.2.2 and the optimal placement of the coil from chapter 5, a short distance to the current-carrying trace is preferable. The voltage requirements and dielectric strength of epoxy and FR4 from subsection 6.3.2 with the bond thickness described in subsection 6.3.1 lead to a mixed calculation of the minimum required distance between trace and coil (Equation 6.8). In Equation 6.9 the minimum distance within the PCB d_{PCB} can be calculated. The result for a bond thickness of 0.1 mm is shown in Equation 6.10.

$$E_{IEC60950-1} \leq d_{PCB}E_{FR4} + d_{bond_{min}}E_{epoxy} \quad (6.8)$$

$$d_{PCB} \geq \frac{4.8 \text{ kV} - d_{bond_{min}} 25.5 \frac{\text{kV}}{\text{mm}}}{13 \frac{\text{kV}}{\text{mm}}} \quad (6.9)$$

$$d_{PCB}(d_{bond_{min}} = 0.1 \text{ mm}) \geq 0.173 \text{ mm} \quad (6.10)$$

$$d_{PCB}(d_{bond_{min}} = 0.0 \text{ mm}) \geq 0.369 \text{ mm} \quad (6.11)$$

The resulting distance from Equation 6.10 has to be used with care. If there are impurities or voids inside the epoxy or a conductive whisker at the current trace, the dielectric strength of the epoxy could locally be below the desired value. So if the quality of the epoxy, the distance of the bond, the complete underfill or the flatness of the current trace can not be ensured, the dielectric strength could not or only partially be considered for the final distance calculation. The worst case “current trace to coil”-distance inside the FR4 is calculated in Equation 6.11. The PCBs were manufactured using the pool service from *Beta LAYOUT GmbH*. Figure 6.4 shows their provided layer build. From the calculations above, the closest distance would be Layer 3 with a final distance of 0.38 mm to the lower end of the PCB. This would be the final distance for the complete dimensioning. This will leave a generous amount of extra distance as security. For the layout, the type of via (e.g. regular vias, burried vias) and its distance to the trace has to be considered. For a first test, the restriction with the via placing can be dropped and therefore tests at the maximum voltage are not possible. The via with epoxy method described in subsection 6.3.2 can be used in any further prototypes. In Figure 6.5 the dimensioning of the PCB with glue and the current trace is depicted for a better comprehension.

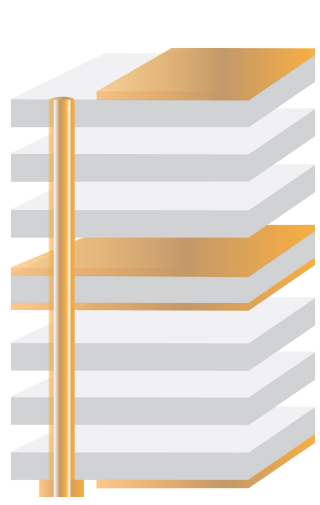
6.3.3.2 Trace Crosssection

The minimum crosssection of copper traces can be calculated by using the maximum current density. But also a maximum temperature rise has to be considered. The maximum thermal current density⁸ for regular copper is $154 \frac{\text{A}}{\text{mm}^2}$ [30, Table 18.3, p. 556]. The maximum melting current density⁹ of copper is $3060 \frac{\text{A}}{\text{mm}^2}$ [30, Table 18.3, p. 556].

Usually the maximum current density in electrical connections is between $2-6 \frac{\text{A}}{\text{mm}^2}$. For bond wires of power electronic devices it could reach more than $500 \frac{\text{A}}{\text{mm}^2}$ for very short distances.

⁸the current density, at which the conductors temperature rises by 200 K.

⁹the current density at which after $\frac{1}{1000}$ s the conductor reaches its meting temperature.



Qty	TypeNo	Type	Thickness/Prepreg
1	7628	Layer 1 Prepreg	0,18 mm
1	2125	Prepreg	0,10 mm
1	2125	Prepreg	0,10 mm
4	7628	Layer 2 Prepreg Layer 3	0,71 mm
1	2125	Prepreg	0,10 mm
1	2125	Prepreg	0,10 mm
1	7628	Prepreg Layer 4	0,18 mm

Figure 6.4: PCB ML4 Layer build of *Beta LAYOUT GmbH* [uk.beta-layout.com/pcb/technology/specifications/]

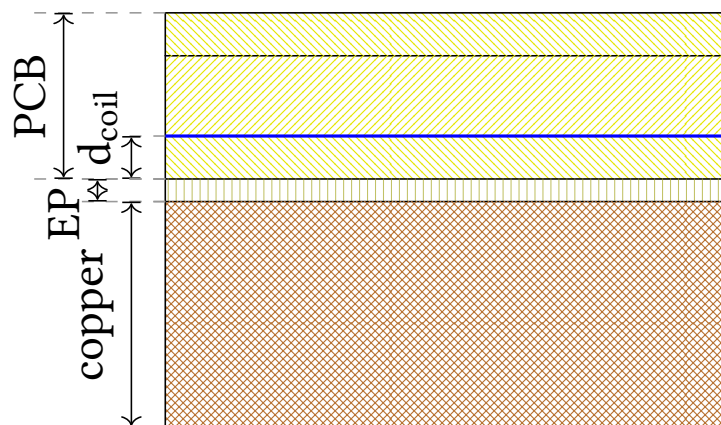


Figure 6.5: Final layer build with PCB (yellow, hatched, divided into three layers according to [Figure 6.4](#)), coil (blue line), epoxy (yellow, thin layer), copper (cross hatching)

For the sensor, the temperature rise has to be limited, because the shear strength of the epoxy decreases with higher temperature. The next limit is the usually available thickness of copper sheets to mill or punch out the current trace. Due to overload ability, the trace has to be designed for a much higher peak current than the nominal current. For the first test, a 2 mm thick and 5 mm wide trace were chosen. This results in 10 mm^2 which equals to a nominal current density of $10 \frac{\text{A}}{\text{mm}^2}$ at 100 A (DC). The trace cooling could be performed by large copper areas where it is soldered down.

7 Experimental Setup

Some experiments are carried out to verify the single sensors and the merged sensor in relation to the expected output or simulation results. For the magnetoresistor the bandwidth is not explicitly stated in the datasheets and therefore needs to be measured. The sensor fusion can be done in the first run in software using recorded measurements of the single sensors. Later the real merged sensor will be measured.

7.1 Evaluation of Current Pulse Generators

For generating a current pulse, there are a lot of possibilities. But the most do have insufficient bandwidth limitations. The following subsections will describe a few solutions, which would be able to meet the bandwidth requirements of at least 500 MHz.

7.1.1 Avalanche Pulse Generator

The avalanche pulse generator was first used to test the bandwidth of scopes with minimum part count and cost. It was first described by Jim Williams in [18, Appendix D] as “Measuring Probe-Oscilloscope Response”. The circuit is shown in Figure 7.1. For implementing current sensors into ASICs, this approach could be a good way to test even very fast sensors with respect to their bandwidth. Unfortunately, the maximum current is way too low for the planned usage. The circuit consists basically out of an RC element that slowly increases the voltage across the collector-emitter U_{CE} of the bipolar transistor till the avalanche breakdown voltage $U_{avalanche}$ is reached. Then the transistor switches to avalanche mode and discharges the energy from the RC elements’ capacitor over a $50\ \Omega$ resistor for a limited time. $U_{avalanche}$ depends heavily on the single transistor and is always higher than the $U_{CEbreakdown}$ that can be found in the datasheets. The author of this application note achieved a pulse width down to 350 ps.

7.1.2 Short-Circuit Switch

The *Institute for Power Electronics and Electrical Drives at the university of Stuttgart* presented in 2017[31] a 300 A pulse current source for high $\frac{dU}{dt}$ rates. The schematic is shown in Figure 7.2. It basically turns on switch S1 during the off-time, which results in a steady current from the current source. For the pulse, S2 will be switched on and shortly afterwards, S1 will be turned off. After this transition, the current will flow through the device under test (DUT) and the reference shunt. To turn off the pulse, S1 needs to be activated again and then S2 needs to be released. The benefit of this circuit is that all inductivities except the inductivities in the branch between S1 and S2 are already in steady state and only the appended inductivity will limit the rise time. That allows to only focus on reducing the inductivity between S1 and S2. The in

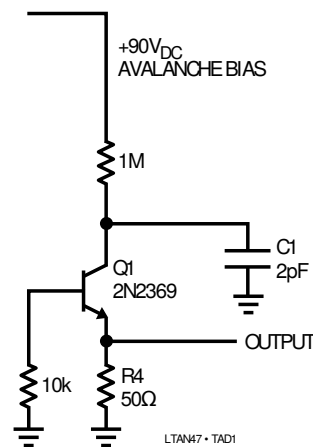


Figure 7.1: avalanche pulse generator [18, Appendix D]

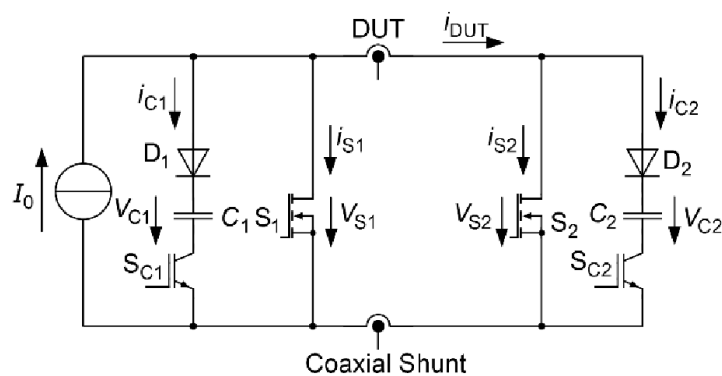


Figure 7.2: 300 A Short Circuit Switch [31]

the paper used coaxial enclosure for the DUT reduces the inductivity while leaving enough space for the DUT. It reduces external electromagnetic interference (EMI), e.g. from the gate drivers, as well. Because the construction and control of such a circuit needs a lot of effort, it was excluded in the course of this thesis

7.1.3 Full-bridge bidirectional pulse generator

The last approach is basically a half bridge which can be actively switch the current through the DUT on and off. When using a fast half bridge and ensuring a very low inductance between the DC-link capacitor, the half bridge and the DUT, it is possible to generate fast rising current pulses. When using two half bridges, it is possible to generate positive and negative current pulses. This would enable the pulse generator to test the linearity of the sensor for positive and negative currents without mechanically reversing the sensor. It also allows to measure the hysteresis of the magnetoresistors and test the degaussing procedure to overcome the hysteresis effect. The setup is described in Figure 7.3. The voltage supply for the half bridges is completely feeded by the DC-link capacitor. The voltage supply does only recharge the capacitor.

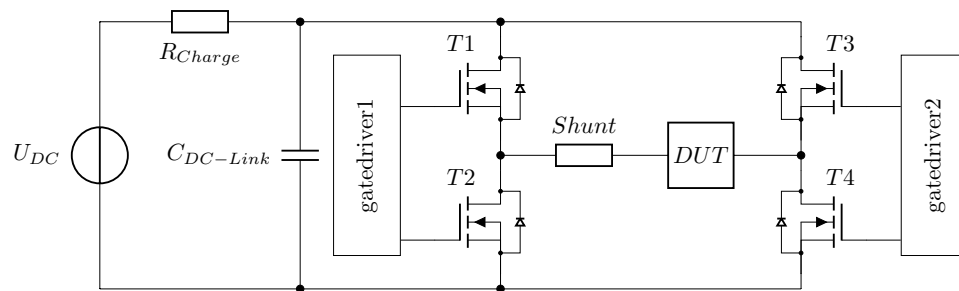


Figure 7.3: 100 A / 10 μ s Full bridge bidirectional Circuit Switch

The charging resistor will limit the maximal current. The main benefit of this circuit is its low energy in the system and no need for a high current power supply. Because the low stored energy in the DC-link capacitor the half bridges will not burn when accidentally turning them on for a long time. The capacitor's charge resistor will effectively limit the maximum continuous current supplied to the whole circuit.

7.2 Prototype (V1)

The experimental construction including the full-bridge bidirectional pulse generator from [subsection 7.1.3](#) has been divided into several parts to simplify the design of each component:

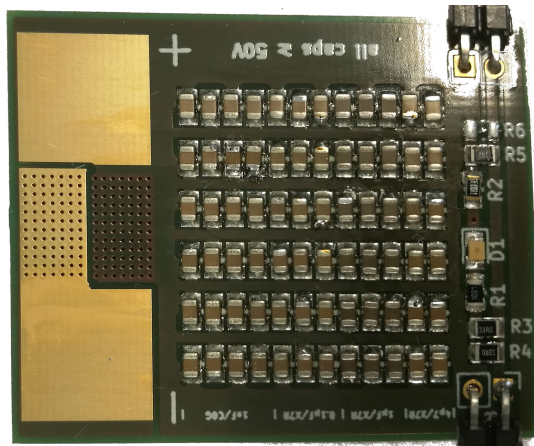
- DC-Link Capacitor
- Shunt
- Two half-bridges
- Sensor adapter for power supply and differential to single-ended signaling
- DUT:
 - Rogowski Coil
 - TMR: Crocus Technology CT219
 - TMR: Sensitec TF952

7.2.1 DC-Link Capacitor

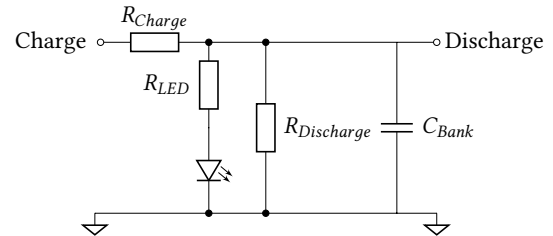
Two capacitors banks were used for constructing the pulse generator. For reducing the parasitic inductance and the parasitic resistance of the DC-link capacitor, a lot of capacitors were soldered in parallel to the PCB. About the first third of capacitors on the board were special “C0G”¹ capacitors for the fast rising edge with low capacity values. The later ones were “X7R”²

¹EIA code for Class 1 ceramic capacitors based on IEC/EN 60384-8/21. C0G features no temperature dependency and no voltage dependency for the capacity.

²Class 2 capacitors with a significant dependency from temperature and voltage.



(a) PCB before mounting onto the pulse generator.

(b) Principle schematic diagram with $R_{Charge} = 10 \Omega$, $R_{Discharge} = 100 \text{ k}\Omega$, $C_{Bank} = 76.224 \mu\text{F}$ **Figure 7.4:** DC-Link Capacitor with 76.224 μF

capacitor for the necessary overall needed capacity. The capacitor bank features charge and discharge resistors and the capacitors with a entire capacity of 76.224 μF . In Figure 7.4 a simplified principle schematic diagram and a image of the PCB are shown. The stored energy can be calculated using the capacity and the voltage of the capacitor using Equation 7.1. The stored energy of one DC-Link Capacitor for 10 V is 3.81 mJ and 15.24 mJ for 20 V.

$$W = \frac{1}{2}CU^2 \quad (7.1)$$

7.2.2 Shunt

The shunt should be used as a current reference. Therefore, a special low inductance power resistor from Vishay³ was chosen. A high resistor value of 100 m Ω was chosen to allow rectangular pulses and to be able to control the maximum current without knowing every parasitic capacitance and inductance. A resistance close to 0 Ω would only generate a high peak current and is completely dependent on the inductivity of the whole setup. A higher resistance will effectively limit the current and allows the capacitor bank to discharge slowly with an approximated flat top for short pulses. In Figure 7.5 a picture of the shunt before mounting is shown. When using the shunt for current measurement, the parasitic inductance has to be considered. According to the shunt's datasheet [32], the resistor should have a parasitic inductance of <5 nH. Equation 7.3 shows the resulting transfer function with the complex frequency $s = 0 + j\omega$. The current can be back-calculated in frequency domain as shown in Equation 7.4 with as the measured voltage $U_{Shunt}(t)$ transformed into frequency domain to $U_{Shunt}(s)$. The shunt is rated for 10 W continuous power dissipation. The setup will be able to feed the shunt with much higher pulse energies. Therefore, the manufacturer has an online tool⁴ with which the pulse energy of the resistor can be displayed according to the

³Vishay WSHP2818: 10 W 100 m Ω shunt resistor[32]

⁴<https://www.vishay.com/resistors/power-metal-strip-calculator/>

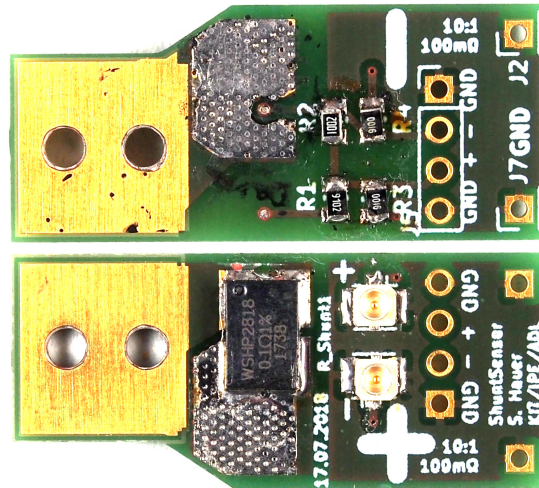


Figure 7.5: Front and back side of the shunt measurement board with 100 mΩ Shunt from Vishay

ambient temperature and pulse duration. A screenshot from the exported PDF can be found in [Appendix B](#). For the maximum pulse time (from [subsection 7.4.1](#)) of 68.8 μs, the shunt can absorb ≈1 kJ of energy. Since the maximum energy of two capacitor banks in parallel is around 30 mJ (see [subsection 7.2.1](#)), the maximum limit of the shunt is pretty far away and the shunt is operated in a safe area.

$$G_{Shunt}(s) = R_{Shunt} + sL_{Shunt} \quad (7.2)$$

$$G_{Shunt}(s) = 0.1 \Omega + s 5 \text{ nH} \quad (7.3)$$

$$I(s) = \frac{U_{Shunt}(s)}{G_{Shunt}(s)} \quad (7.4)$$

7.2.3 Half-Bridge

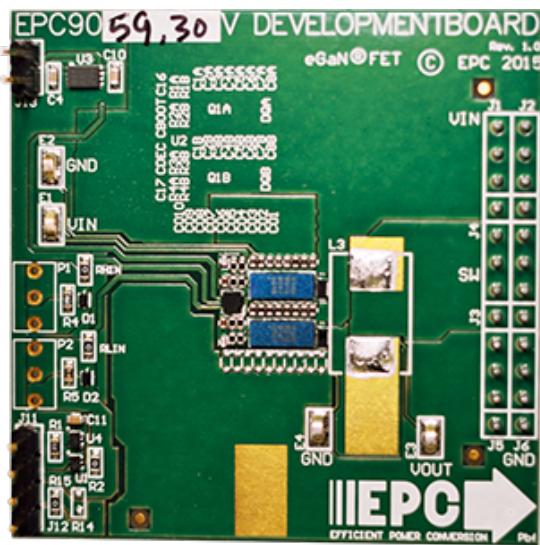
For the half-bridge, the main focus was a high-as-possible switching frequency and rise time in current. eGaN⁵/E-HEMT⁶ proved to be the best choice as technology for the half bridge design. There are two main manufacturer for eGaN-Transistors: *GaN Systems*⁷ and *EPC Cooperation*⁸. For the setup, only half-bridges without an inductor are needed. The *GaN Systems* evaluation boards were not suited, because they were ready to use converter boards with an inductor and are designed for high continuous power output. *EPC-cooperation* sells evaluation boards with half-bridges only. The chosen board (EPC9059[33]) has a high voltage slew rate of about 1 ns according to the datasheet. The board consist out of two EPC2100 eGaN die's which are wired in parallel. Each can only handle 10 A on the top side switch and 40 A on the bottom side switch. But for pulse load they can handle ten times the current for 300 μs at 25 °C. For

⁵Enhancement Mode gallium nitride

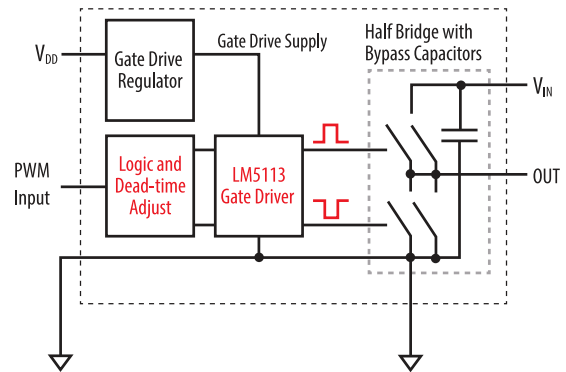
⁶Enhancement high electron mobility

⁷<https://gansystems.com/>

⁸<http://epc-co.com>



(a) Photo of the PCB from <https://epc-co.com/epc/portals/0/epc/boards/EPC9059.png>



(b) Principle schematic diagram [34]

Figure 7.6: The half-bridge from EPC-Cooperation

one half-bridge board, a maximum current of 200 A can be handled safely. The board and its simplified schematic are displayed in Figure 7.6.

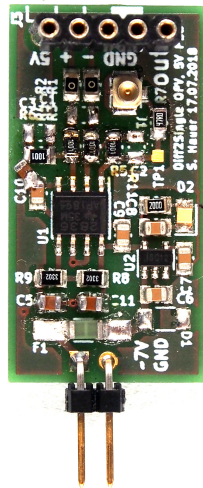
7.2.4 Sensor Adapter

All sensor circuits require a filtered 5 V supply and output their signals using differential signaling. A sensor adapter was built for supplying and signal conditioning. It consists out of a voltage regulator and an op amp circuit. To measure the sensors' signal via differential signaling at the scope, either a differential probe is available or it has to be converted to a single ended signal. The later was done using a differential amplifier. A virtual ground at the half-supply voltage is required for this circuit. The schematic and a picture of the PCB is shown in Figure 7.7. The resistor $R10$ is needed because the output of the op amp has to be decoupled from the capacitive load ($C11$ and $C5$).

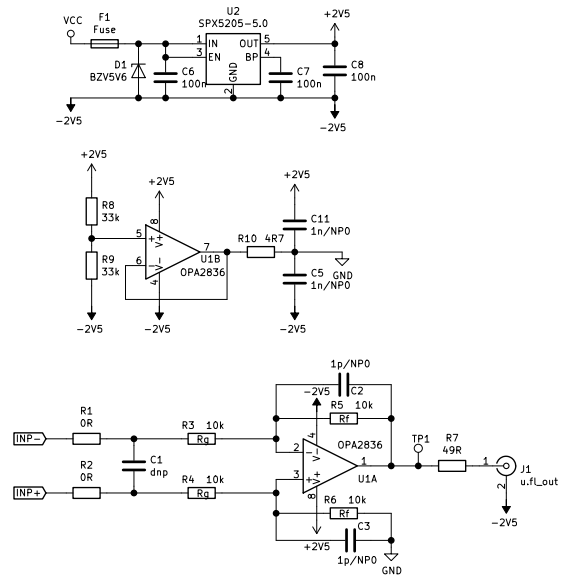
7.2.5 Device Under Test

The test setup can be used with different sensors as device under test (DUT). Three different DUT's were developed. The sensor principles were described in detail in chapter 3. All sensors use the same fully differential OPV Texas Instruments THS4521 for signal conditioning. All sensor outputs were fully differential and so, there were no reference ground connection in the measurement path.

The *Planar Rogowski coils* in Figure 7.8 represents the high-frequency sensor and has a passive differential lowpass ($f_g = \frac{1}{2\pi \cdot 2RC}$) directly after the coil. It also has the possibility to tap the response of the coil after the lowpass without an amplifier.

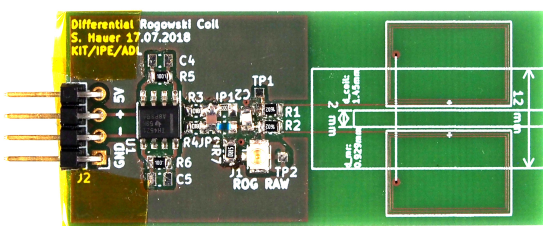


(a) Photo of the PCB

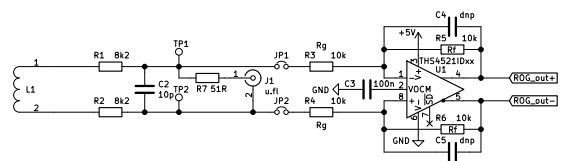


(b) Schematic diagram

Figure 7.7: Sensor Adapter with power supply and differential to single-ended signaling

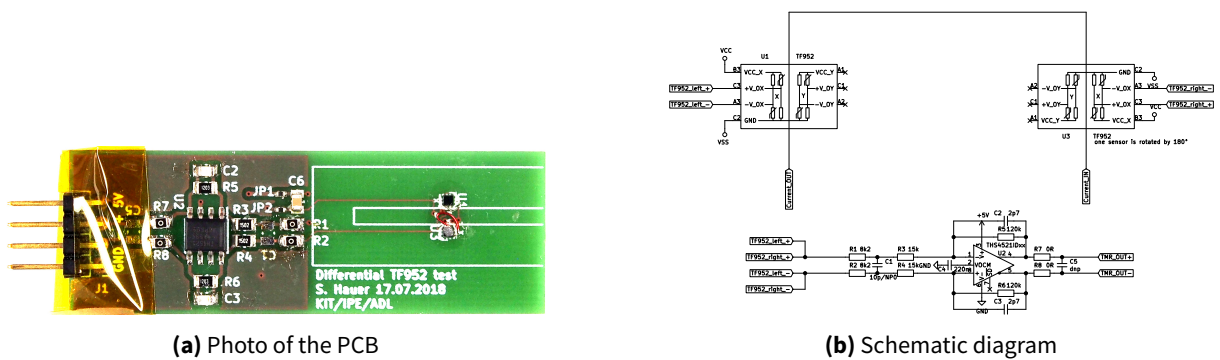


(a) Photo of the PCB



(b) Schematic diagram

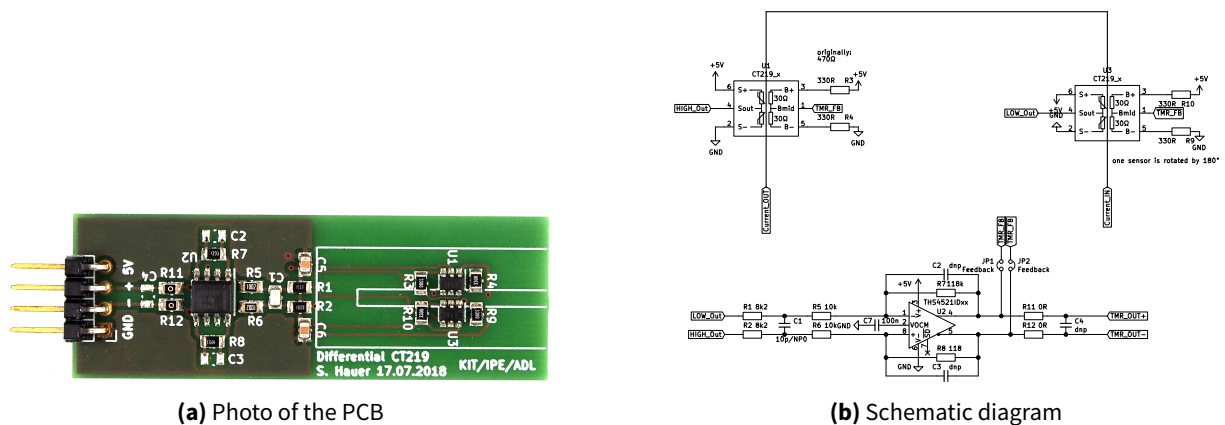
Figure 7.8: The planar differential Rogowski coil. It is sensing the high frequency parts of the current applied to the trace. The PCB consists out of the Rogowski coil (L1), an differential passive integrator, an following fully differential amplifier as an impedance converter. The auxiliary tap (J1) is used for measuring the coil signal directly after the integrator.



(a) Photo of the PCB

(b) Schematic diagram

Figure 7.9: The *Sensitec TF952* magnetoresistor. The sensing elements are mechanically rotated by 180° and then simply connected in parallel. The sensing elements measure the current always into the same direction of their x-axis because the sensors are rotated with the current flow which turns 180° as well.



(a) Photo of the PCB

(b) Schematic diagram

Figure 7.10: The *Crocous CT219* magnetoresistor. It features the in [subsection 3.1.3](#) described closed loop control to keep the sensor for the complete measurement range within its linear range.

The *Sensitec TF952* magnetoresistor sensor board basically consists out of two magnetoresistor wheatstone bridges which are mechanically rotated by 180° against each other. Due to the current trace shape (U-shaped current bar), both sensors measure the current into the same direction and external fields will be measured with a phase difference of 180° which cancels them out. A schematic and the PCB is shown in [Figure 7.9](#).

The *Crocous CT219* magnetoresistor sensor board – like the TF952 board – out of two magnetoresistors which are rotated by 180° against each other. The bias current described in the datasheet[8] is controlled via the differential outputs in a P-control⁹ mode. With two sensors, a differential sensor was constructed. The explained sensing structure is shown in [Figure 7.10](#) including a picture of the PCB.

⁹proportional-control describes in control theory a control where the error will be compensated by an error-proportional value.

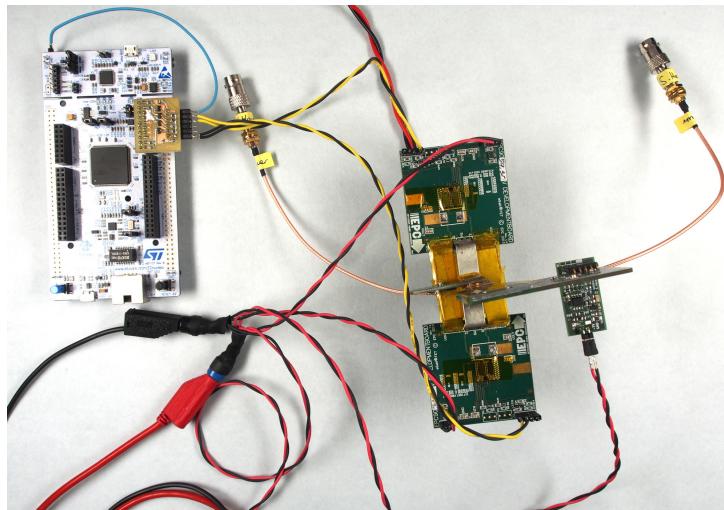


Figure 7.11: The Measurement setup with all main components connected via tinned copper bars. It includes the pulse generator board, the half-bridges and the shunt.

7.3 Measurement setup

All the parts from the last chapter were combined using copper bars shown in [Figure 7.11](#). To use this construction, a few parts are missing:

- Power supply
- Oscilloscope
- Pulse Generator
- Readout equipment

These parts will be described in the following subsections.

7.3.1 Power Supply

Supplying the different parts with power requires a few different voltages. They can be merged into two different supply voltages. The first voltage source is a variable voltage source from 0 V to 25 V for charging the DC-link capacitor bank. The second voltage source supplies 7 V for the sensor adapter and the gate drivers. The pulse generator was supplied via USB by the connected computer. The specific power supply unit (PSU) can be controlled using a serial connection based on the virtual instrument software architecture (VISA).

7.3.2 Oscilloscope

The oscilloscope used for all measurements is a 500 MHz four-channel *Keysight InfiniiVision MSO-X 3054T*. It captures all signals with a sample rate of up to $2.5 \frac{\text{GSa}}{\text{s}}$. The oscilloscope can be completely remote controlled via its VISA interface¹⁰.

7.3.3 Pulse Generator

As a pulse generator, a STM¹¹ Nucleo Microcontroller board¹² with a four channel level shifter was used. The microcontroller was programmed to provide an VISA interface for changing settings and initiating pulses. It supports setting the pulse width, the number of cycles, the pulse period time and a switch for positive and negative current pulses (Using either the left or the right half-bridge).

7.3.4 Readout equipment

A computer was used for controlling and triggering the pulse generator and controlling and receiving measurements of the oscilloscope. All measurements were evaluated during the post-processing. The algorithms used for the measurements will be described in the next section.

7.4 Experiments

The main purpose of this experimental setup is to verify the theoretical optimizations and the frequency response of all these sensors.

The measurement after the initial testing and calibration of the equipment should include:

- Frequency response of all sensors
- Hysteresis measurement for magnetoresistors
- Degaussing for magnetoresistors
- Combined sensor with complete sensor fusion

7.4.1 Frequency response

For the frequency response, a rectangular pulse can be used. Due to generating a clean rectangular pulse is complicated, an exponential pulse was generated as a test signal for the sensing elements. Therefore, the gate pulse generator was turned on till the capacitor bank was discharged. The necessary times were calculated using the corresponding time constants $\tau = RC$. For charging one capacitor bank, there are three parallel 33Ω resistor in series to the capacitor bank with $76 \mu\text{F}$. This results in a time constant $\tau_{charge} = 838 \mu\text{s}$. For discharging over an overall

¹⁰the VISA interface was used over USB

¹¹ST Microelectronics [<https://www.st.com>]

¹²Nucleo-144 STM32F767ZI board

resistance of approx. $120 \text{ m}\Omega$ the time constant results in $\tau_{\text{discharge}} = 18 \text{ }\mu\text{s}$ for the two capacitor banks in parallel. After $t = 5 \tau$ a capacitor has reached 99 % charge¹³ and can be considered as fully charged. The same time $t = 5 \tau$ can be used for estimating the discharging time of the capacitor. For the measurement, the charge current while discharging the capacitors has to be considered. Using $4200 \text{ }\mu\text{s}$ for charging and $100 \text{ }\mu\text{s}$ for discharging leads to a pulse period of $4300 \text{ }\mu\text{s}$. The 16 Pulses need around 68.8 ms . Acquiring about 1000 samples will take approx. 2 min not considering the data download time at the scope. The multiple pulses were done, to increase the accuracy in time and frequency domain and to reduce the noise in the frequency domain.

In [algorithm 1](#) the basic measurement acquisition method is written down. It has to be mentioned, that the scope's manual was misunderstood and this scope is not able to do averaging over multiple data samples. Therefore the time domain averaging will always be 1.

The post-processing ([algorithm 2](#)) is basically a discrete Fourier transformation (DFT) and

Initialize Gate pulser

```

| set pulse width to 100  $\mu\text{s}$ 
| set pulse period to 4300  $\mu\text{s}$ 
| set pulse cycles to 16 pulses

```

Initialize Scope

```

| set for 16 time series averaging

```

for number of samples do

```

| start scope trigger mode SINGLE
| start pulse generator
| wait till pulse generator finished
| wait for scope trigger
| receive and save measurement data from scope

```

end

Algorithm 1: Measurement data acquisition: The scope will trigger on the signal generated by the pulse generator. The interaction between all devices is controlled by this algorithm.

plotting it as a bode plot afterwards. But especially the current reference has to be considered. The shunt has a known transfer function found in the datasheet which consists out of a resistive and an inductive part (explained in [subsection 7.2.2](#)).

7.4.2 Hysteresis measurement

Every magnetic sensing element does have some sort of hysteresis. It can be characterized by measuring the three characteristic points *saturation magnetization* B_S , *remanent magnetization* B_R and *magnetic coercivity* H_c . These parameters and the corresponding plot were briefly

¹³The Charging can be calculated with:

$$Q(t) = Q_0 \left(1 - e^{-\frac{t}{\tau}}\right)$$

$$\frac{Q(3\tau)}{Q_0} = 95 \% \quad \frac{Q(4\tau)}{Q_0} = 98 \% \quad \frac{Q(5\tau)}{Q_0} = 99 \%$$

```

Function doFFT( $x(t)$ , sampling rate, time step)
    Strip DC-offset
    calculate amplitude correction factor14
    calculate DFT15
end
Function time2frequency(data, time)
    calculate time step16
    calculate sampling rate17
    doFFT(data, sampling rate, time step)
    back-calculating the current from shunt measurement18
    calculate transfer function19
    combine sensors20
end

```

Algorithm 2: Measurement data post-processing with DFT. For valid current measurement, the shunt measurement has to be processed with its transfer function to get the real current value. The current will then be used to calculate the transfer function of the sensor based on the measurements.

introduced in [subsection 3.1.2](#). Using the existing setup, [algorithm 3](#) describes one possible way to measure the hysteresis. All measured parameters (B_S , B_R and H_C) do not really reflect the magnetic field or the magnetic flux density, they rather describe these values transformed to an output voltage and input current with respect to the complete sensor. The algorithm basically drives the current till a specified maximum current I_{max} is reached and declares the resulting voltage as B_S . After that the pulse generator is turned off and the voltage is measured as B_R . In the next step the current will be slowly shifted towards the negative maximum current $-I_{max}$. After the measured current reaches 0 V, the set current represents H_C . The same has to be done in the reverse direction. After measuring the parameters in both directions, half of the distance between the corresponding parameters can be calculated which then describes the final parameter values. This is necessary due to the initially existent offset of the sensor and since it will not start exactly in the center of the hysteresis curve. Due to lack of time this measurement procedure has not yet been implemented, tested and evaluated.

7.4.3 Degaussing

To minimize hysteresis effects described in the last section, a “degaussing”-procedure can be performed. The theory was explained in [subsection 3.1.2](#). As in the last section, the “degaussing” was not implemented and tested due to lack of time.

Function measureCurrentSteadyState(I_{set})

```

| set voltage for  $I_{set}$ 
| generate pulse
| measure top value of pulse as  $I_{measured}$ 
| return  $I_{measured}$ 

```

end

$I_{max} = [100 \text{ A}, -100 \text{ A}]$

$\mathbf{B}_S = \mathbf{B}_R = \mathbf{H}_C = [0,0]$

for $i \in [0, 1]$ **do**

```

|  $\mathbf{B}_S(i) = \text{measureCurrentSteadyState}(I_{max}(i))$ 

```

```

|  $\mathbf{B}_R(i) = \text{measureCurrentSteadyState}(0 \text{ A})$ 

```

```

|  $I_{measured}(old) = 2I_{max}(i)$ 

```

```

| for  $I_{set} \leftarrow I_{max}(i)$  to  $-I_{max}(i)$  do

```

```

| |  $I_{measured}(new) = \text{measureCurrentSteadyState}(I_{set})$ 

```

```

| | if  $\text{abs}(I_{measured}(old)) < \text{abs}(I_{measured}(new))$  then

```

```

| | |  $\mathbf{H}_C(i) = I_{set}$ 

```

```

| | | break

```

```

| | end

```

```

| |  $I_{measured}(old) = I_{measured}(new)$ 

```

```

| end

```

end

$\mathbf{B}_S = \frac{\|\mathbf{B}_S\|_2}{2}$

$\mathbf{B}_R = \frac{\|\mathbf{B}_R\|_2}{2}$

$\mathbf{H}_C = \frac{\|\mathbf{H}_C\|_2}{2}$

Algorithm 3: Hysteresis measurement: The current will be ramped up till I_{max} for \mathbf{B}_S then with $I = 0 \text{ A}$ for \mathbf{B}_R and while reversing the current to $-I_{max}$ and $\mathbf{B} = 0$ for \mathbf{H}_C . For symmetry issues, this procedure has to be done in both directions and averaged later on.

7.5 Conclusion (V1)

With the first version, the principle operation of the magnetoresistors and Rogowski coil was confirmed. As key values, a Bandwidth of 500 kHz has been achieved for the *Sensitec TF952* magnetoresistor. The *Crocus CT219* achieved 4 MHz. The Rogowski coil showed the desired behavior using the passive integrator, but not with the selected operational amplifier. The amplifiers real properties posed the main problem. They require a low input impedance which is not possible for high impedance sensors. Therefore amplifiers are needed that feature input impedance of several M Ω . The following section will list more errors and their solution for the next prototype.

7.6 Prototype (V2)

With the first set of sensor boards, a few limitations were uncovered. The main problems were:

- The fully differential operational amplifier was fast enough, but the maximum possible input impedance is way too low (the input common-mode resistance was about 100 k Ω ²¹)
- The coil had no voltage biasing which let the coil voltage float
- a second low-pass filter is needed to cutoff the Rogowski coil at about 100 MHz
- The fully differential amplifiers need low valued feedback resistors to allow a high bandwidth
- Due to an error in the Datasheet[9] of the TMR sensor TF952, the pinout has changed
- After initial testing, both sensors can no be combined on one PCB

The second (LC) low-pass filter was needed in order to suppress ringing at the end of the measurement bandwidth and to limit the sensor bandwidth for following ADC's.

7.6.1 Circuit Simulation

To ensure that the sensors work as required, a circuit level simulation using *LTspice*²² was implemented. [Figure 7.12](#) was developed for solving all problems listed above. The equivalent circuit model from [section 6.2](#) was used to test the response of the whole system including the operational amplifiers. After a lot of fine tuning, the result of the simulation can be displayed in time and frequency domain ([Figure 7.13](#) and [Figure 7.14](#)).

The steps taken to improve the design will be explained in the following paragraph: The current pulse was generated using a voltage source which performs a voltage step series. The shunt model was implemented to study how the measured signal at the shunt acts over the frequency range. This improved the estimation of the parasitic inductance of the shunt and

²¹fully-differential amplifier: Texas Instruments THS4521

²²<http://www.analog.com/en/design-center/design-tools-and-calculators/ltspice-simulator.html>

allows to back-calculate the current signal from the shunt's signal. The complete Rogowski coil model without the secondary parasitic capacitance was numerically calculated in [section 6.2](#). Then the passive differential integrator with a cutoff frequency of 500 kHz was simulated. A big issue when using an instrumental amplifier was the common-mode rejection²³. The complete circuit from the Rogowski coil to the amplifier does not have ground connection. To ensure that the idle signal will always be around half of the supply voltage, a biasing circuit with a voltage divider was established. The following (LC) low-pass filter was then used to damp and cut-off the frequency parts that would lead to oscillations at the far end of the bandwidth. The following instrumental amplifier circuit does a fully differential impedance conversion to allow standard differential amplifiers to process the sensor's signal. The added feedback capacitor increases the amplifier's bandwidth.

7.6.2 Hardware

For the second prototype, both sensors were implemented on one circuit board. Both sensors feature a passive signal conditioning and a following instrumental amplifier to apply gain and reduce the impedance the fully differential summing amplifier can work with. The schematic can be found in [Figure A.1](#). A figure of the fully populated circuit board is shown in [Figure 7.15](#).

²³Even for the Rogowski coil signal which does not contain dc parts, a bias network is crucial. If the differential voltage idle state is close to the maximum/minimum supply voltage, an incoming signal will touch the rails of the amplifiers very fast. Even if it does not touch the rails of the instrumental amplifier, it will touch the rail of the fully differential amplifier due to the missing common-mode rejection for the instrumental amplifier. To ensure the maximum performance, the common-mode voltage has to be set to the half supply voltage.

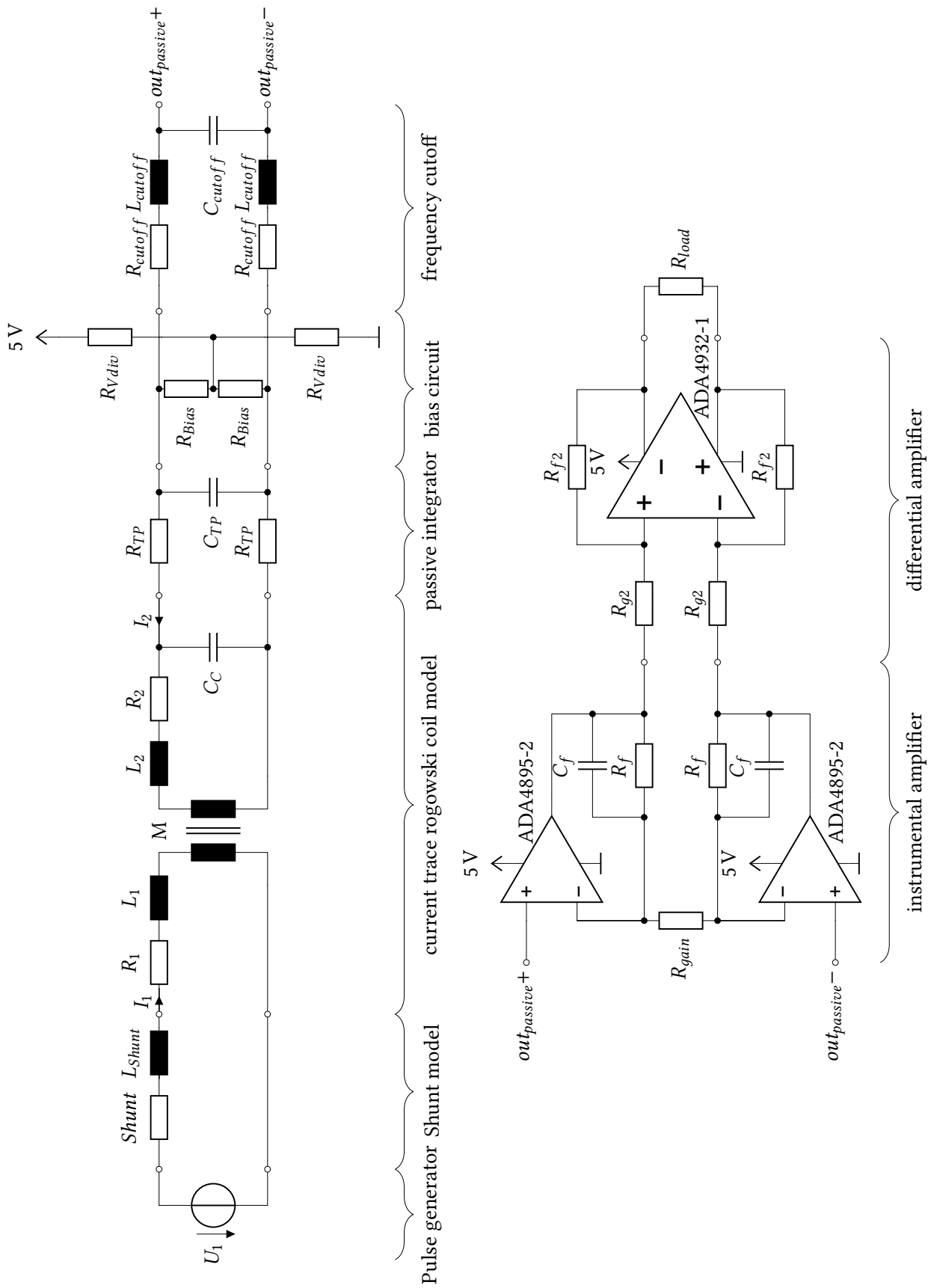


Figure 7.12: Schematic for simulation using LTSpice

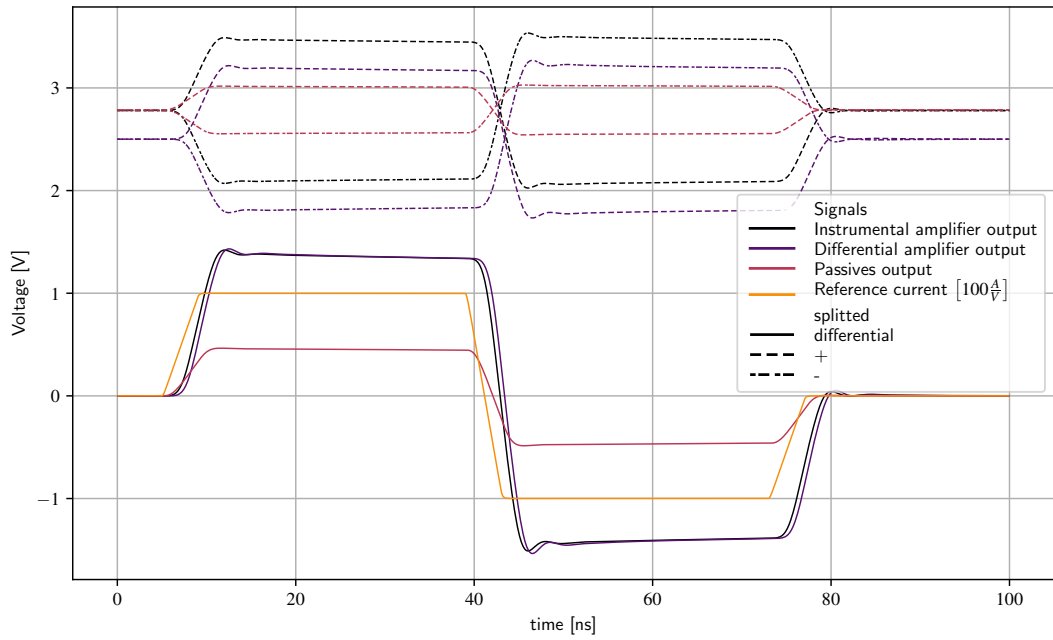


Figure 7.13: Time domain simulation results from Figure 7.12 using LTspice

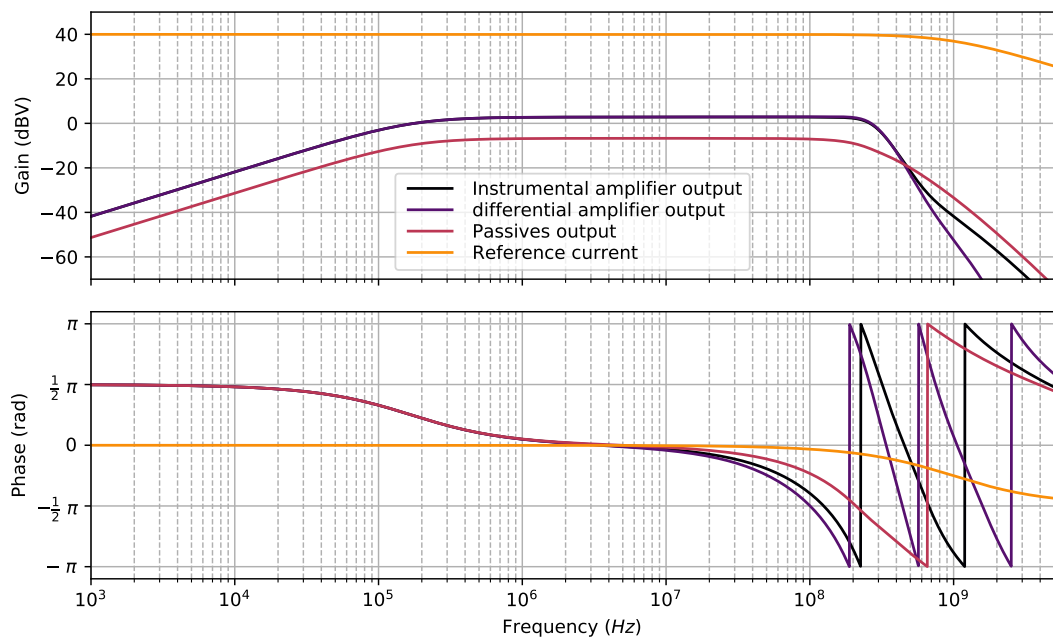
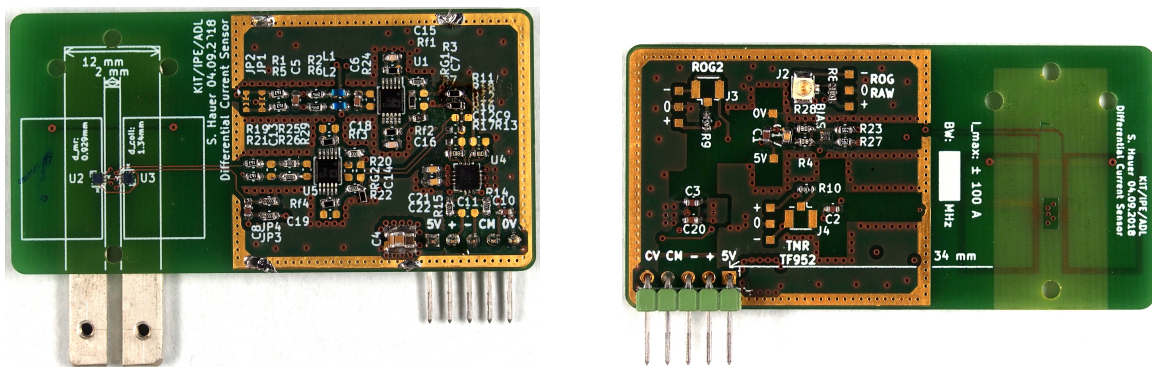


Figure 7.14: Frequency domain simulation results from Figure 7.12 using LTspice



(a) Front side of the sensor.

(b) Back side of the sensor.

Figure 7.15: Fully populated circuit board with TMR sensor TF952 and planar Rogowski coils. The board features the sensors, passive signal conditioning followed by a fully differential instrumental amplifier for impedance conversion. The Sensor fusion is then done using a fully differential amplifier as an adder and output buffer.

7.7 Measurement Results (V2)

Four different measurements were done for the characterization of the sensor as an current sensor.

Two magnetoresistor measurements with and without a low-pass filter, the Rogowski coil and the merged sensor was measured. For all measurements, a time domain double pulse test and a frequency domain bandwidth characterization was done.

All measurements were done using the $50\ \Omega$ termination in the scope to archive the maximum possible bandwidth.

7.7.1 Double Pulse

The double pulse test describes the time domain reaction of the sensor to a current signal represented with the shunts signal. The test can be seen as a slight variation of the bandwidth measurement from the experiment control standpoint. The double pulse test was carried out by applying two current pulses to the current-carrying trace. The lower current on the second pulse comes from the discharge behavior of the capacitor bank which results in an exponential slope of the capacitor banks voltage. The charge and discharge time constants are that different, that there is almost no recharging during the off-time. The ripples during the turn-on time results most likely from the turn-on behavior of the used transistor half-bridges.

The magnetoresistor shows in Figures 7.17a and 7.17b the expected bandwidth but does feature an unwanted rising edge distortion.

The filtered magnetoresistor shows in Figures 7.18a and 7.18b the same behavior than the unfiltered. but the rising edge distortion is now beyond the low-pass filter cut-off frequency.

The Rogowski coil shows in Figures 7.19a and 7.19b the expected pulses on both edges.

The merged sensor shown in Figures 7.20a and 7.20b combines the fast rising time from the Rogowski coil and the steady state value from the magnetoresistor. It clearly follows the shunt

value. The first overshoot pulse of the sensor results most likely from the spike on the rising edge.

All graphs show clearly that there are no offset issues after a current pulse and the rise time is about 100 ns for the combined sensor.

7.7.2 Bandwidth Characterization

For the bandwidth characterization explained in [subsection 7.4.1](#), an 100 A exponential current pulse was used. It was generated using the *full-bridge bidirectional pulse generator* setup in [subsection 7.1.3](#). For the single sensing effect measurement, the other sensor's adder resistor were removed from the fully differential amplifier. The current was back-calculated from the shunt measurements according to [subsection 7.2.2](#). As the first step, the single sensing elements were tested including their complete signal conditioning and amplifier stages. Later the sensor was combined used a simple adder on-board. The relevant transfer function "G_sensor" was calculated as $\frac{\text{sensor}}{\text{current}}$.

The magnetoresistor measurements in [Figure 7.17c](#) show a good flatness in the magnitude till 500 kHz and then there is a dip from where the sensor recovers. Due to this not on the first view explainable behavior, a low-pass filter with the edge frequency of 500 kHz was used to cut off the sensor at this point.

With the added filter in [Figure 7.18c](#), the magnetoresistor shows a clear decrease with -20 dB per decade. The increasing magnitude after 1 MHz seems to be almost only artificially due to the measurement because the combination of the Rogowski coil and the filtered magnetoresistor does not show this behavior. The phase swing at 1 MHz has also be mentioned. The origin of this swing is unclear.

The Rogowski coil in [Figure 7.19c](#) shows a clear and wanted increase of magnitude till 500 kHz and reaches a steady state over frequency till about 20 MHz. After 20 MHz the sensors output voltages reaches the noise floor of the scope. All results from within the noise floor are unusable and do not have any relevance. The gain for this Rogowski coil measurement is the twice the gain later used for the combined sensor.

The combined sensor shown in [Figure 7.20c](#) shows a merged sensor with a bandwidth of 20 MHz. The plot shows a magnitude dip at 200 kHz and a gain between the plateaus left and right of this dip. This measurement is as well affected from the noise floor, the signal steps into around 20 MHz.

7.7.3 Explanations

For the combined sensor, the magnitude has to be slightly adjusted to match the Rogowski coil and magnetoresistor gain. The small dip in the transfer function of the merged sensor can

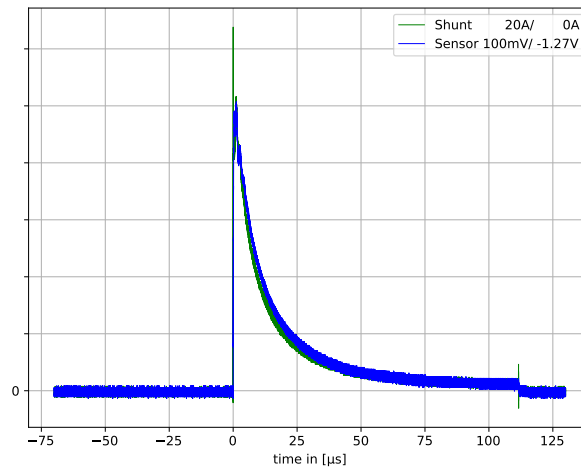
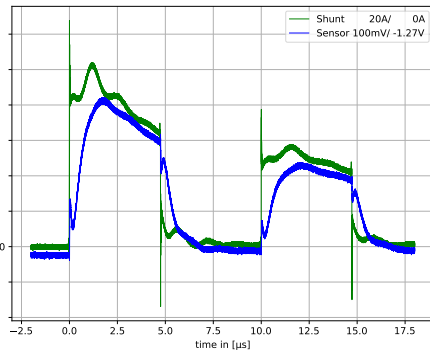


Figure 7.16: Exponential pulse test result in time domain. The pulse form was used for the bandwidth characterization.

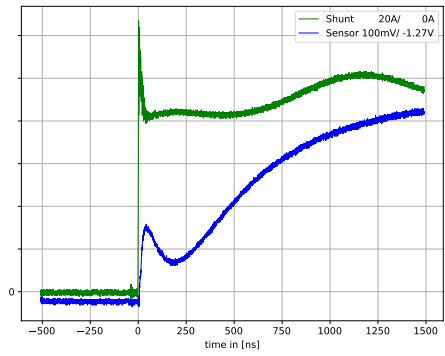
possibly be corrected by slightly increasing the cut-off frequency of the low-pass filter from the magnetoresistor or decreasing the cut-off frequency of the Rogowski coil's integrator. The maximum bandwidth had been chosen with respect to the phase: When the sensor signals touches the noise floor, the phase does not keep steady any more. at this point, the frequency is considered to be the maximum bandwidth of the sensor.

To bring the measurement in one line with the simulation, the corresponding bode plots were used. [Figure 7.14](#) shows the simulation bode plot. [Figure 7.19c](#) the measurement bode plot. The big absolute gain differences are because the simulation did not need a reference. The simulation simply calculated the signals output in dB. The measurement results was the division between the sensor output and the current measurement. The sensor shows almost the same slope till the first knee with +20 dB per decade. The sensor shows then a plateau till it reaches the noise floor. The second knee with a about 200 MHz can not be seen due to the noise floor. With the test setup it is not possible to measure the high frequency currents higher than 20 MHz.

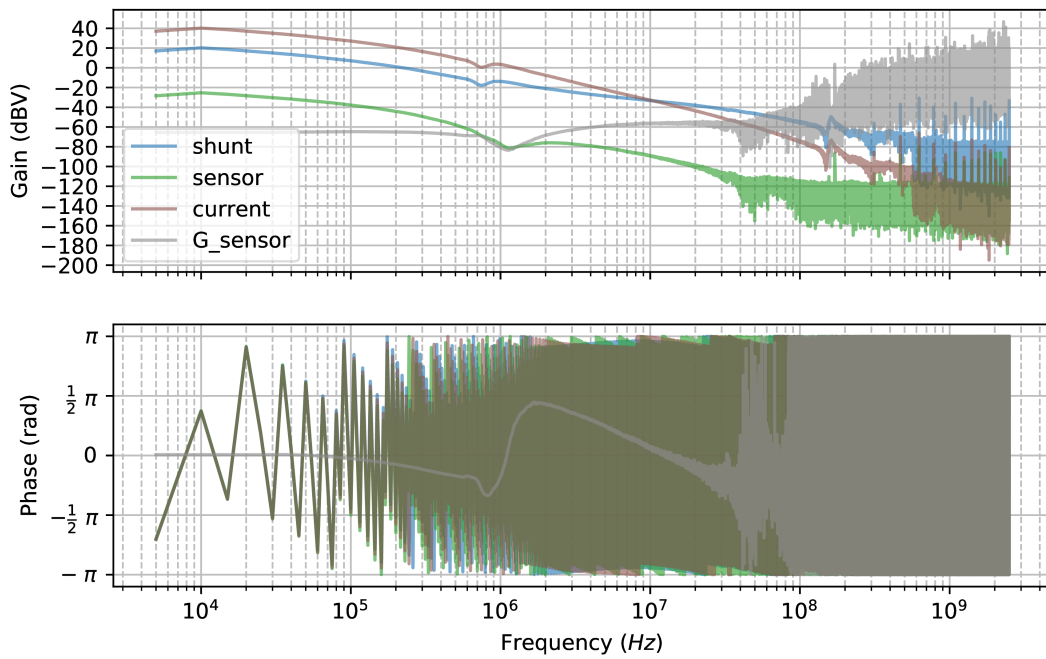
Due to the step current magnitude of frequency was not constant over the complete frequency range of interest, the sensor signal was weak starting at about 10 MHz and immerse into the noise floor. It would be an easy fix to increase the current from 100 A to 200 A, but this would lead to saturation of the amplifiers which would result in magnitude and phase ringing which would make the signal almost unusable. Also increasing the gain to a maximum is not always possible. The first instrumental amplifier has to keep the output voltage swing below the value, the fully differential amplifier can handle including all common-mode voltage issues. The fully differential amplifier is not an output rail-to-rail amplifier which results in a maximum output voltage swing with 1.5 V distance to both rails. For the simulation, a voltage of about 20 kV and a source resistance of 50 Ω were chosen to archive 200 A. This high voltage was chosen allow the the simulated current to be constant over the frequency till 500 MHz. But the simulation is



(a) The time domain results from an exponential pulse.

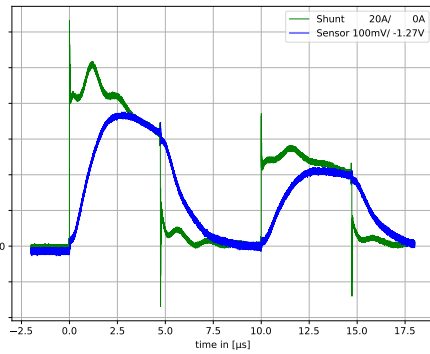


(b) Closeup view of the rising edge

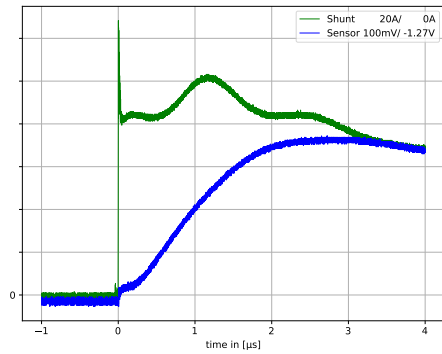


(c) The transfer function of the magnetoresistor part of the sensor without an additional lowpass filter. The reference current was back-calculated from the shunt measurement.

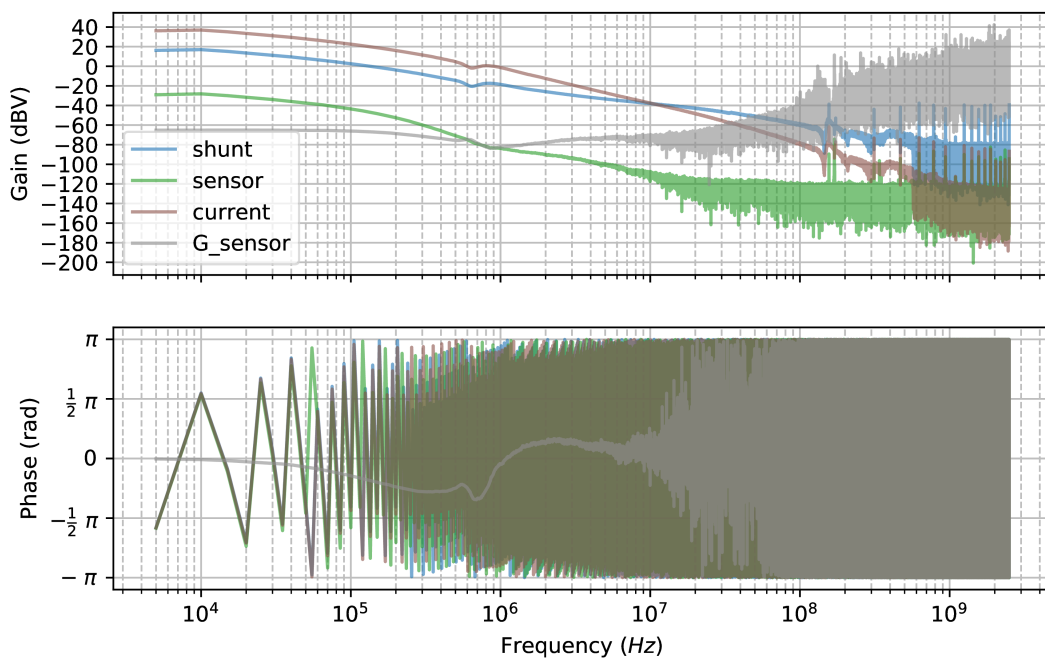
Figure 7.17: Bandwidth characterization for the magnetoresistor part of the sensor without an additional lowpass filter.



(a) The time domain results from an exponential pulse.

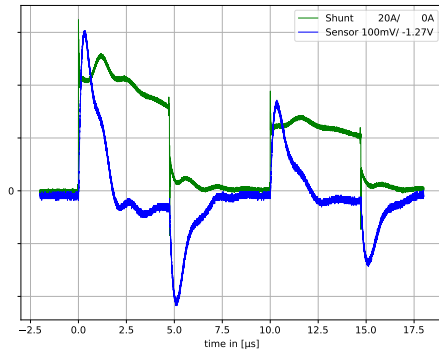


(b) Closeup view of the rising edge

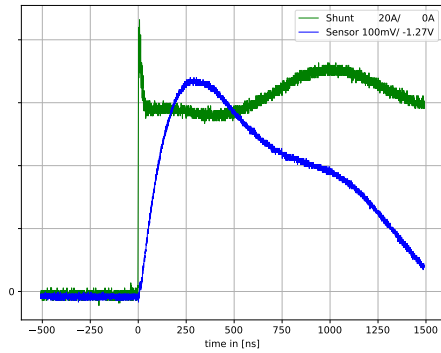


(c) The transfer function of the magnetoresistor part of the sensor including the low-pass filter at 500 kHz. The reference current was back-calculated from the shunt measurement.

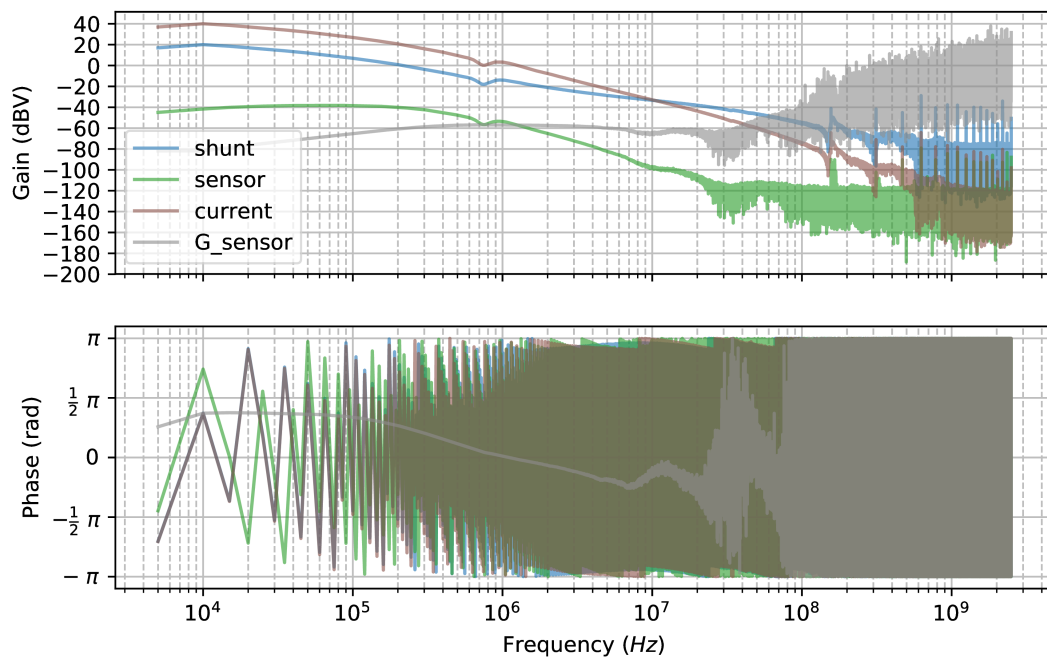
Figure 7.18: Bandwidth characterization for the magnetoresistor part of the sensor including a low-pass filter. Therefore an exponential pulse was used as described in [subsection 7.4.1](#).



(a) The time domain results from an exponential pulse.

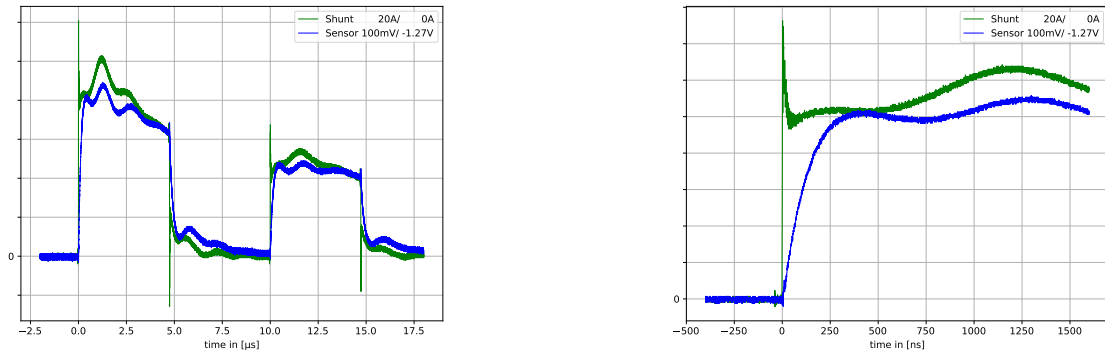


(b) Closeup view of the rising edge



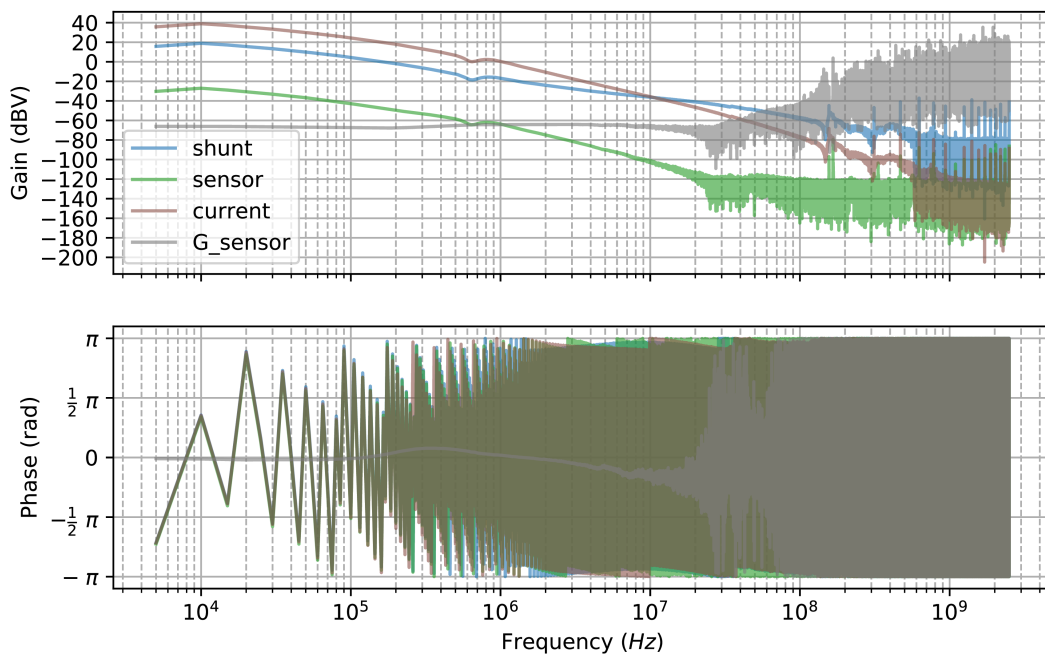
(c) The transfer function of the Rogowski coil part of the sensor. The reference current was back-calculated from the shunt measurement. The integration of the magnetoresistor starts as intended at about 500 kHz. At about 20 MHz the sensor signal is too weak for the scope and enters the noise floor of the scope measurement. The measurement does have a maximum frequency of about 20 MHz.

Figure 7.19: Bandwidth characterization for the Rogowski coil part of the sensor. Therefore an exponential pulse was used as described in [subsection 7.4.1](#).



(a) The time domain results from an exponential pulse.

(b) Closeup view of the rising edge



(c) The transfer function of the complete current sensor. The reference current was back-calculated from the shunt measurement. At about 20 MHz the sensor signal is too weak for the scope and enters the noise floor of the scope measurement. The measurement does have a bandwidth of about 20 MHz.

Figure 7.20: Bandwidth characterization for the merged sensor. Therefore an exponential pulse was used as described in [subsection 7.4.1](#).

at this point simply wrong. That high voltage would introduce a much higher inductance due to the insulation needed. The current trace itself would of course generate arcs because 2 mm trace gap would not be able to withstand more than 6 kV²⁴. Furthermore, transistors which would be able to reach the rising time needed for the sensor are not available for that high voltages.

The basic ideas to overcome the issues are:

- Rising the current magnitude at high frequencies with e.g. a higher voltage for the capacitor bank.
- Increasing the resolution of the scope (above 8 bit).
- Using an amplifier with ± 15 V supply voltage and ± 10 V output voltage swing.

For the first idea would likely not work due to the inductance of the system would increase with the voltage because the capacitors get bigger for the higher their withstand voltage is which leads to a higher inductance. Furthermore the current setup can not be used beyond 30 V as the maximum voltage rating. A higher voltage than approx 48 V would make the setup more complex due to the needed additional safety requirements. A scope with a higher vertical resolution could be used but would be more expensive and will most likely have a lower system bandwidth. The last idea to increase the output voltage to ± 10 V would use the complete range of the scope's 50 Ω input. The output of the amplifier would be connected with a 50 Ω output in series. The signal will then be feed using a coaxial cable into the scope's 50 Ω input.

As a conclusion, the sensor has to be tested with an entirely different setup which can deliver the currents at high frequencies. This possibly more complex setup would be well beyond the scope of this thesis.

²⁴The dielectric strength of air is about 3 $\frac{\text{kV}}{\text{mm}}$ at room temperature and normal pressure.

8 Outlook

As future work, the ideas from the experimental results in [subsection 7.7.3](#) could be used to improve the bandwidth measurement. For a measurement beyond 50 MHz, a complete new test setup has to be developed because the weak current signals at frequencies beyond this point are not usable for characterizing a current sensor any more. The shunt should be characterized by measuring the corresponding S-parameters for higher quality results, because the shunts transfer function has only been estimated with measurements and the datasheet. This would allow a more accurate current measurement which then would affect the precision of the bandwidth measurement.

For a commercial use of a fully working sensor, many tests would be required especially for compliance with all standards. These standards include for example the electromagnetic compatibility and RoHS¹. The reliability, linearity, over current behavior, maximum operating conditions and the lifetime has to be measured and estimated.

For noise reduction, the Rogowski coil could be shielded based on the findings in the paper “Micro PCB Rogowski coil for current monitoring and protection of high voltage power modules”[35].

Another approach would be to try the third possibility from [subsection 4.2.3](#) which states the use of a single coil between the U shaped current trace. Due to the small size of the coil this approach would more or less require a circuit board with very small traces or an (rather large) ASIC². For currents up to 100 A such a chip could include coils and the complete signal conditioning. An ASIC would also lead to the opportunity to reduce the current consumption of the sensor and further increase the bandwidth. On an ASIC chip, the filters can be integrated more easily with their precise values. Parasitic capacities and inductivities (depending on the technology process) can be suppressed or at least included into the design.

¹Restriction of Hazardous Substances Directive

²Application-specific integrated circuit

9 Summary and Conclusion

The sensing elements were selected based on the stated requirements in [section 1.2](#). The selected sensors and their operation modes were introduced. Furthermore the known pitfalls of these sensors e.g. their hysteresis were explained. In [chapter 4](#) the preliminary system design was explained and serves as the basis for the magnetic field simulation. Furthermore the sensor fusion concept was explained.

In [chapter 5](#) an introduction how to simulate the coupling between planar Rogowski coils and a current trace were given. For reducing the effort of simulation, the problem was reduced to a two dimensional level. Therefore a proof was stated to explain why and under which circumstances the three dimensional problem can be solved using a two dimensional simulation. With the results from the two dimensional magnetic field simulation a postprocessing was used to optimize the optimal placement of the Rogowski coil and magnetoresistor. The simulation results are verified by subsequent experiments. The results can as well be used as a general idea, how planar Rogowski coils can be placed, even if the geometry is slightly different. After the magnetic field simulation a final dimensioning of the sensor was carried out. The main focus was the galvanic insulation with the corresponding standards and the attachment of the primary current-carrying trace to the sensor PCB.

For the experimental setup, almost the complete test setup was constructed and build during the thesis. The first results were not as good as expected but promising, that there was no general mistake in the Rogowski coil/magnetoresistor design and placement. A circuit level simulation based on the numerically calculated Rogowski coil equivalent circuit were than used to fix almost all the little mistakes in the first revision.

The second revision of the hardware was constructed and build to allow the sensors to be merged directly using a fully differential adder directly on board. The results shown in [section 7.7](#) show that both sensors and the merged sensor work as expected. The targeted bandwidth of 100 MHz was not achieved due to problems with the test setup. The magnitude of the current was beyond 20 MHz too weak. The sensor output immersed into the noise floor of the scope measurement. There was no sign that the sensor's transfer function was going to decrease before or at 20 MHz. It is in general possible that the sensor reaches a higher bandwidth, but the test setup was not able to generate the necessary magnitude for current pulses at higher frequencies.

All in all, the most requirements from [section 1.2](#) were fulfilled. The bandwidth requirement could not be measured but for now the requirement is not fulfilled.

List of Figures

3.1	Simplified transfer functions for AMR, GMR and TMR	7
3.2	An exemplary hysteresis curve	8
3.3	Different measurement methods for magnetoresistor sensors	10
3.4	Experiment for measuring the magnetic induction voltage by Walter Rogowski in 1912	12
3.5	Schematic of a Rogowski coil	12
3.6	Schematic for a low-pass filter after an simplified Rogowski coil	14
4.1	The magnetic field generated by a circular current-carrying wire	16
4.2	A U-shaped current trace	17
4.3	The magnetic field generated by one or two current-carrying traces	18
4.4	The first possibility to place coils on top of an single conductor. The main advantage is the common mode rejection.	20
4.5	The second possibility to place coils on top of an U shaped conductor. The main advantage is the reduced inserted inductance and the possibility to place the magnetoresistor in a differential manner.	21
4.6	The third possibility to place a coil on top of an U shaped conductor. The main advantage is the reduced inserted inductance and the high response from the traces.	22
4.7	Sensor fusion concept in the frequency domain	25
5.1	3D simulation volume in <i>COMSOL Multiphysics</i>	28
5.2	Description of the connection between the magnetic flux Φ_B and the magnetic vector potential A_z and magnetic flux density B_x using a thin circular wire.	31
5.3	A current trace underneath a circuit board with embedded coils as the simulation volume	33
5.4	Screenshots from a <i>COMSOL Multiphysics</i> simulation	34
5.5	Software flowchart for magnetic field simulation	35
5.6	The real coil layout with 0.15 mm thick traces and relevant dimensions	37
5.7	Different parts of the objective functions for coil placement using the U-shaped trace	38
5.8	Different parts of the objective functions for magnetoresistor placement using the U-shaped trace	39
5.9	Normalized Bode plots for the sensors respective optimal point	39
5.10	Optimal trajectories for different coil distances and trace shapes for single current trace assembly	40
6.1	Generic two port model	43
6.2	Equivalent Circuit model of a transformer or Rogowski coil with a current trace.	43

6.3	Current Trace on top of PCB with epoxy over the vias	45
6.4	PCB ML4 Layer build of <i>Beta LAYOUT GmbH</i>	47
6.5	Final layer build with PCB, coil, epoxy and copper	47
7.1	avalanche pulse generator [18, Appendix D]	50
7.2	300 A Short Circuit Switch [31]	50
7.3	100 A / 10 μ s Full bridge bidirectional Circuit Switch	51
7.4	DC-Link Capacitor with 76.224 μ F	52
7.5	Front and back side of the shunt measurement board with 100 m Ω Shunt from Vishay	53
7.6	The half-bridge from <i>EPC-Cooperation</i>	54
7.7	Sensor Adapter with power supply and differential to single-ended signaling	55
7.8	The planar Rogowski coils	55
7.9	The <i>Sensitec TF952</i> magnetoresistor	56
7.10	The <i>Crocous CT219</i> magnetoresistor	56
7.11	The Measurement setup with all main components connected via copper bars	57
7.12	Schematic for simulation using <i>LTspice</i>	64
7.13	Time domain simulation results from Figure 7.12 using <i>LTspice</i>	65
7.14	Frequency domain simulation results from Figure 7.12 using <i>LTspice</i>	65
7.15	Fully populated circuit board with TMR sensor TF952 and planar Rogowski coils. The board features the sensors, passive signal conditioning followed by a fully differential instrumental amplifier for impedance conversion. The Sensor fusion is then done using a fully differential amplifier as an adder and output buffer.	66
7.16	Exponential pulse test result in time domain. The pulse form was used for the bandwidth characterization.	68
7.17	Bandwidth characterization for the magnetoresistor part of the sensor without an additional lowpass filter.	69
7.18	Bandwidth characterization for the magnetoresistor part of the sensor including a low-pass filter. Therefore a exponential pulse was used as described in subsection 7.4.1	70
7.19	Bandwidth characterization for the Rogowski coil part of the sensor. Therefore a exponential pulse was used as described in subsection 7.4.1	71
7.20	Bandwidth characterization for the merged sensor. Therefore a exponential pulse was used as described in subsection 7.4.1	72
A.1	Circuit diagram for the second hardware revision	84
B.1	Vishay WSHP2818 100 m Ω shunt resistor - Pulse energy calculator: part 1	86
B.2	Vishay WSHP2818 100 m Ω shunt resistor - Pulse energy calculator: part 2	87

List of Tables

- 3.1 A comparison of general properties for different magnetoresistive effects . . . 6
- 3.2 A comparison of properties from selected TMR sensors 6

- 5.1 Optimization Results for both sensors 41

- 6.1 Rogowski coil equivalent circuit parameters 44

List of Algorithms

1	Measurement data acquisition	59
2	Measurement data post-processing with DFT	60
3	Hysteresis measurement	61

Bibliography

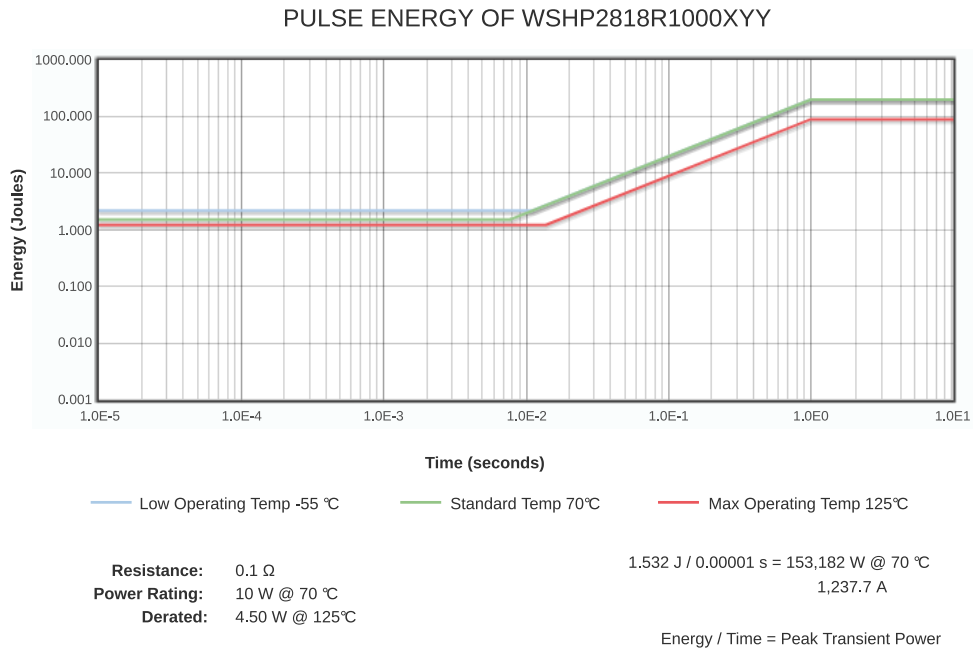
- [1] S. Ziegler et al. “Current Sensing Techniques: A Review”. In: *IEEE Sensors Journal* 9.4 (Apr. 2009), pp. 354–376. DOI: [10.1109/JSEN.2009.2013914](https://doi.org/10.1109/JSEN.2009.2013914).
- [2] F. R. S. Professor W. Thomson. “On the electro-dynamic qualities of metals:—Effects of magnetization on the electric conductivity of nickel and of iron”. In: *Proc. R. Soc. Lond.* 8 (Jan. 1856), pp. 546–550. DOI: [10.1098/rspl.1856.0144](https://doi.org/10.1098/rspl.1856.0144).
- [3] G. Binasch et al. “Enhanced magnetoresistance in layered magnetic structures with antiferromagnetic interlayer exchange”. In: *Phys. Rev. B* 39 (7 Mar. 1989), pp. 4828–4830. DOI: [10.1103/PhysRevB.39.4828](https://doi.org/10.1103/PhysRevB.39.4828).
- [4] M. Julliere. “Tunneling between ferromagnetic films”. In: *Physics Letters A* 54 (Sept. 1975), pp. 225–226. DOI: [10.1016/0375-9601\(75\)90174-7](https://doi.org/10.1016/0375-9601(75)90174-7).
- [5] *1- and 2-Axis Magnetic Sensors HMC1001/1002/1021/1022*. HMC1021s. Rev C. Honeywell. Aug. 2008. URL: https://aerocontent.honeywell.com/aero/common/documents/myaerospacecatalog-documents/Missiles-Munitions/HMC_1001-1002-1021-1022_Data_Sheet.pdf.
- [6] M. N. Baibich et al. “Giant Magnetoresistance of (001)Fe/(001)Cr Magnetic Superlattices”. In: *Phys. Rev. Lett.* 61 (21 Nov. 1988), pp. 2472–2475. DOI: [10.1103/PhysRevLett.61.2472](https://doi.org/10.1103/PhysRevLett.61.2472).
- [7] David D. Djayaprawira et al. “230% room-temperature magnetoresistance in CoFeB/MgO/CoFeB magnetic tunnel junctions”. In: *Applied Physics Letters* 86.9 (2005), p. 092502. DOI: [10.1063/1.1871344](https://doi.org/10.1063/1.1871344).
- [8] *Differential Sensor*. CT219. Rev 1.1. Crocus Technology Inc. 2017. URL: <https://crocus-technology.com>.
- [9] *MagnetoResistive Magnetic Field Sensor*. TF952. DSE_01 Preliminary data sheet. Sensitec GmbH. Apr. 2018. URL: <https://www.sensitec.com>.
- [10] *TMR2103 TMR Linear Sensor*. TMR2103. Ver. 1.0a. MultiDimension Technology Co., Ltd. May 2015. URL: <http://www.dowaytech.com/en/index.php?c=download&id=1515>.
- [11] *AA/AB-Series Analog Magnetic Sensors*. NVE Corporation. Sept. 2018. URL: https://www.nve.com/Downloads/analog_catalog.pdf.
- [12] *AAV003-10E Current Sensor*. AAV003-10E. Rev 1.1. NVE Corporation. Feb. 2012. URL: https://www.nve.com/Downloads/AAV003-10E_Data_Sheet.pdf.
- [13] W. Rogowski and W. Steinhaus. “Die Messung der magnetischen Spannung”. In: *Archiv für Elektrotechnik* 1.4 (Apr. 1912), pp. 141–150. DOI: [10.1007/BF01656479](https://doi.org/10.1007/BF01656479).
- [14] Adolf J. Schwab. *Hochspannungsmesstechnik : Messgeräte und Messverfahren*. Berlin, Heidelberg, 2011. DOI: [10.1007/9783642198823](https://doi.org/10.1007/9783642198823).

- [15] R. J. Thomas. “High-Impulse Current and Voltage Measurement”. In: *IEEE Transactions on Instrumentation and Measurement* 19.2 (May 1970), pp. 102–117. DOI: [10.1109/TIM.1970.4313872](https://doi.org/10.1109/TIM.1970.4313872).
- [16] N. Tröster et al. “Wide Bandwidth Current Sensor Combining a Coreless Current Transformer and TMR Sensors”. In: *PCIM Europe 2018; International Exhibition and Conference for Power Electronics, Intelligent Motion, Renewable Energy and Energy Management*. June 2018, pp. 1–7. URL: <https://ieeexplore.ieee.org/document/8403012/>.
- [17] B. Parkhideh and S. J. Nibir. “Hybrid Magnetoresistor-Planar Rogowski Current Sensing Scheme With Folded Trace Magnetic Field Concentration Technique”. In: *IEEE Sensors Journal* 17.11 (June 2017), pp. 3446–3452. DOI: [10.1109/JSEN.2017.2691262](https://doi.org/10.1109/JSEN.2017.2691262).
- [18] Jim Williams. “Linear Technology AN-47: High Speed Amplifier Techniques”. In: (Aug. 1991).
- [19] Junfeng Jiang and Kofi Makinwa. “A hybrid multipath CMOS magnetic sensor with 210 μ Trms resolution and 3MHz bandwidth for contactless current sensing”. In: Jan. 2016, pp. 204–205. DOI: [10.1109/ISSCC.2016.7417978](https://doi.org/10.1109/ISSCC.2016.7417978).
- [20] N. Tröster et al. “Wide bandwidth current probe for power electronics using tunneling magnetoresistance sensors”. In: *2017 IEEE 12th International Conference on Power Electronics and Drive Systems (PEDS)*. Dec. 2017, pp. 35–40. DOI: [10.1109/PEDS.2017.8289128](https://doi.org/10.1109/PEDS.2017.8289128).
- [21] B. Parkhideh and S. J. Nibir. “Hybrid Magnetoresistor-Planar Rogowski Current Sensing Scheme With Folded Trace Magnetic Field Concentration Technique”. In: *IEEE Sensors Journal* 17.11 (June 2017), pp. 3446–3452. DOI: [10.1109/JSEN.2017.2691262](https://doi.org/10.1109/JSEN.2017.2691262).
- [22] John David Jackson and Christopher Witte. *Klassische Elektrodynamik; 4th rev. version*. Berlin: De Gruyter, 2006. ISBN: 9783110189704. URL: <https://cds.cern.ch/record/989052>.
- [23] Günther Lehner. *Elektromagnetische Feldtheorie : für Ingenieure und Physiker*. Springer-Link : Bücher. Berlin, Heidelberg: Springer Berlin Heidelberg, 2010. ISBN: 978-3-642-13042-7. DOI: [10.1007/978-3-642-13042-7](https://doi.org/10.1007/978-3-642-13042-7).
- [24] A.R. Parkinson, R. Balling, and J.D. Hedengren. *Optimization Methods for Engineering Design*. Brigham, UT: Brigham Young University, 2013. URL: http://flowlab.groups.et.byu.net/me575/textbook/optimization_book.pdf.
- [25] Fernando Puente León and Holger Jäkel. *Signale und Systeme*. Berlin, 2015. DOI: [10.1515/9783110403862](https://doi.org/10.1515/9783110403862).
- [26] David M. Pozar. *Microwave engineering*. 4. ed. Hoboken, NJ: Wiley, 2012. ISBN: 978-0-470-63155-3.
- [27] Mattan Kamon, Michael J Tsuk, and Jacob K White. “FASTHENRY: A multipole-accelerated 3-D inductance extraction program”. In: *IEEE Transactions on Microwave theory and techniques* 42.9 (1994), pp. 1750–1758.
- [28] Matton Kamon et al. “Fasthenry user’s guide”. In: *Research Laboratory of Electronics, Department of Electrical Engineering and Computer Science, Massachusetts Institute of Technology* (1996).

-
- [29] *Technical Data Sheet LOCTITE EA M-121HP*. Henkel. Jan. 2015. URL: <http://tds.henkel.com/tds5/Studio/ShowPDF/EA%20M-121HP-EN?pid=EA%20M-121HP&format=MTR&subformat=REAC&language=EN>.
- [30] Eduard [Hrsg.] Vinaricky, ed. *Elektrische Kontakte, Werkstoffe und Anwendungen : Grundlagen, Technologien, Prüfverfahren*. Berlin, Heidelberg, 2016. DOI: [10.1007/978-3-642-45427-1](https://doi.org/10.1007/978-3-642-45427-1).
- [31] N. Tröster et al. “Design of a 300 Amps Pulsed Current Source with Slopes up to 27 Amps per Nanosecond for Current Probe Analysis”. In: *PCIM Europe 2017; International Exhibition and Conference for Power Electronics, Intelligent Motion, Renewable Energy and Energy Management*. May 2017, pp. 1–6. ISBN: 978-3-8007-4424-4. URL: <https://ieeexplore.ieee.org/document/7990694/>.
- [32] *Power Metal Strip® Resistors, High Power (10 W), Low Value (down to 0.001 Ω), Surface Mount*. Vishay Intertechnology, Inc. June 2018. URL: <https://www.vishay.com/docs/30347/wshp2818.pdf>.
- [33] *EPC2100 – Enhancement-Mode GaN Power Transistor Half-Bridge*. EPC – EFFICIENT POWER CONVERSION CORPORATION. Nov. 2017. URL: https://epc-co.com/epc/Portals/0/epc/documents/datasheets/EPC2100_datasheet.pdf.
- [34] *Demonstration System EPC9059 Quick Start Guide*. EPC – EFFICIENT POWER CONVERSION CORPORATION. 2015. URL: https://epc-co.com/epc/Portals/0/epc/documents/guides/EPC9059_qsg.pdf.
- [35] M. Tsukuda et al. “Micro PCB Rogowski coil for current monitoring and protection of high voltage power modules”. In: *Microelectronics Reliability* 64 (2016). Proceedings of the 27th European Symposium on Reliability of Electron Devices, Failure Physics and Analysis, pp. 479–483. DOI: [10.1016/j.microrel.2016.07.011](https://doi.org/10.1016/j.microrel.2016.07.011).

A Appendix: Circuit Diagram for hardware version 2

B Appendix: Vishay pulse energy calculator



	Ambient Temperature (°C)	% Rated Power	Derated Power (W)	Wire Energy (J)	Cross-Over (sec)	STOL 1s (J)	STOL 5s (J)
Low	-55	100%	10.00	2.216	0.0111	200.0	200.0
Medium	70	100%	10.00000	1.532	0.0077	200.0	200.0
High	125	45%	4.50000	1.231	0.0137	90.0	90.0

Low Operating Temp -55 °C		Standard Temp 70 °C		Max Operating Temp 125 °C		
	Time	Energy	Time	Energy	Time	Energy
Cross Over	0.000010	2.216	0.000010	1.532	0.000010	1.231
	0.000010	2.216	0.000010	1.532	0.000010	1.231
STOL 1 seconds	0.0111	2.216	0.0077	1.532	0.0137	1.231
STOL 5 seconds	1	200.00	1	200.00	1	90.00
	5	200.00	5	200.00	5	90.00
	Power (W)	Current (A)	Power (W)	Current (A)	Power (W)	Current (A)
Cross Over	221,566	1,489	153,182	1,238	123,092	1,109
	221,566	1,489	153,182	1,238	123,092	1,109
STOL 1 seconds	200.0	44.7	200.0	44.7	90.0	30.0
STOL 5 seconds	200.0	44.7	200.0	44.7	90.0	30.0
	40.0	20.0	40.0	20.0	18.0	13.4

Figure B.1: Vishay WSHP2818 100 mΩ shunt resistor - Screenshot of the Pulse energy calculator from <https://www.vishay.com/resistors/power-metal-strip-calculator/>

Pulse Chart Description:

Section 1: (typically < 20 milliseconds)

The first portion of the curve is based on the amount of energy required to raise the temperature of the mass of resistance wire to a maximum of 350 °C. This temperature is below the curie point of the alloy so that it does not cause annealing, stress relief, and/or grain structure changes that would cause resistance shift. This limit assures that resistance shift does not occur over the lifetime of the part that exceeds the limits of the datasheet. Resistors with more resistor wire mass are able to withstand a larger pulse energy than a resistor of lower mass; for example, a 2512 10 m(ohm) part will have a higher surge capacity than a 1206 10 m(ohm) resistor. This temperature is based on decades of testing and experience in manufacturing wirewound resistors.

Section 2: (20 milliseconds to 1 second, positive slope)

This positive sloping section of the curve is when a sufficient amount of time has passed to allow for the heat energy to transfer from the wire into the surroundings, such as ambient air, terminations, PCB,... As time progresses, more energy is transferred to the larger mass of the PCB so that the pulse capability becomes dependent upon the thermal performance characteristics of the system.

Section 3: (1 second to 5 seconds)

This is the portion of the curve that is based on the Short Time Overload rating of the part, which can be up to 5 x rated power for 5 seconds. If a part is rated for 1 W (1 Joule / second), then it would have an energy dissipation capability of 25 Joules.

Additional Information:

The pulse capability varies according to the resistance value of the part based on how much material is removed for trimming to resistance value and tolerance or on the thickness of the resistive element. The pulse capability of the part is not limited to the continuous power rating of the part because the short duration of the transient is dependent upon resistive element mass and temperature rise. A short duration pulse will have much higher power than the continuous rating of the part; refer to explanation detailed in Section 1.

Figure B.2: Appendix from Pulse energy calculator from <https://www.vishay.com/resistors/power-metal-strip-calculator/> when using the export Button